國立交通大學

電機資訊學院
顯示科技研究所

碩士論文

液晶排列配向結構之動態取影與逆問題

Dynamic Optical Probing and Inverses Problem of Liquid Crystal Alignment Structures

研究生：李建輝

指導教授：黃中垚 教授

中華民國九十七年九月

液晶排列配向結構之動態取影與逆問題

Dynamic Optical Probing and Inverses Problem of Liquid Crystal Alignment Structures

研究生：李建輝　　Student：Jien-Hui Li

指導教授：黃中垚　　Advisors：Professor Jung Y. Huang

國立交通大學電機資訊學院

顯示科技研究所

碩士論文

A Thesis
Submitted to Institute of Display
College of Electrical Engineer and Computer Science
National Chiao Tung University
in Partitial Fulfillment of the Requirements
for the Degree of
Master
in
Display Institute

September 2008
Hsinchu, Taiwan, Republic of China

中華民國九十七年九月

液晶排列配向結構之動態取影與逆問題

研究生：李建輝　　指導教授：黃中垚 教授

國立交通大學

顯示科技研究所

摘要

液晶的排列指向在液晶應用是很重要的性質。在本篇論文中，我們利用加入混合垂直配向的延展態液晶盒做為例，以模擬計算與量測的光學結果相比較，得到靜態與動態液晶指向分佈資訊。我們模擬計算液晶的排列與光學反應使用液晶自由能張量表現型式。實驗量測使用高靈敏度攝影機搭配延遲時間產生器來擷取液晶盒的動態影像。我們針對取得液晶的排列指向逆問題做了理論分析與實驗示範。結果發現在加入混合垂直配向可消除延展態液晶的暖機時間，但也增加了液晶盒的反應時間。在利用逆問題的方法取得液晶的排列指向，我們提出了符合液晶特性的正則化矩陣，並驗證使用大範圍入射角的光學測量數據和系統量測誤差在百分之十下，在此逆問題求解是穩定而可靠的。從實際實驗示範成功展示在不同施加電壓下的液晶盒內之液晶排列指向可穩定而可靠取得。

Dynamic Optical Probing and Inverses Problem of Liquid Crystal Alignment Structures

Student：Jien-Hui Li Advisors：Professor Jung Y. Huang

Department of Photonics and Display Institute,
National Chiao Tung University

Abstract

The liquid crystal (LC) director profile is an important property for a variety of LC applications. In this study, we combine simulation and experimental measurement of the optical responses of hybrid alignment liquid crystal cells to demonstrate the functionality of LC director profile retrieval. Our simulation invokes the *Q*-tensor formalism of liquid crystal director calculation and Berreman matrix method for the optical response of LC. An electron-multiplying charge coupled device and a delay time generator were combined to capture the dynamic optical image of the liquid crystal cells. We discovered that by including a hybrid alignment region into an OCB cell, the warm up time of the LC cell can be effectively eliminated. The relaxation time was unfortunately also increased. We also study the inverse problem of LC to retrieve the director profile of liquid crystal cell directly from the measured optical transmittance data. To retrieve the director profile from the inverse problem technique, we proposed a regularization matrix based on a priori knowledge of LC. We found our method can yield LC director profile reliably from the measured optical data covering a wide range of incident angle and 10% noise level. We further demonstrated the functionality by retrieving the liquid crystal director profiles of LC cells with applied voltage from the experimentally measured data.

誌謝

在碩士班的時間裡，感謝指導教授 黃中垚教授所給予我偌大的收穫，讓我真正體會到做一份研究所需要的嚴謹態度以及用邏輯的思考來解決問題。雖然過程辛苦，但是我想唯有紮實的訓練，才是真正做學問的基礎。

再來感謝實驗室裡的柳萱學姐，總是能給我適當的協助與解答，還有雲漢學長、秉寬學長、燦丞、綿綿、建佑，給了在嚴肅的研究生活裡最好的調劑。

最後要感謝的是我的父母與家人，提供我精神上最大的支持，讓我能夠用最積極的狀態來完成這份研究。

Content

Abstract (in Chinese) **i**

Abstract (in English) **ii**

Acknowledgement (in Chinese) **iii**

Contents **iv**

List of Tables **vi**

List of Figures **vii**

1 Introduction to the Physical and Optical Properties of LC **1**

1.1 Motivation.....2

1.2 The Physics of Liquid Crystal.....3

1.3 The Optical Properties of Liquid Crystal.....7

2 Models of the LC Alignment Structure and the Optical Response **12**

2.1 The *Q*-Tensor Formalism.....13

2.2 The Berreman Matrix Method.....21

2.3 The Application Examples.....30

3 Dynamic Optical Probing for Hybrid Alignment Liquid Crystal Cells **38**

3.1 Introduction.....38

3.2 The Modification of The Existing OCB Cell……..39

3.3 Experimental Setup of the Dynamic Optical Probing Apparatus.....41

3.4 Results and Discussion…….....43

4 Inverse Problem of Liquid Crystal Director Profile 56

4.1 Introduction to the Inverse Problem.....56

4.2 The Inverse Problem of Liquid Crystal Director Profile.....62

4.3 Theoretical Details.....65

4.4 Simulation Results and Discussion.....71

5 Inverse Retrieval of Liquid Crystal Director Profile from Measured Optical Transmittance Data 81

5.1 Experimental Apparatus for Inverse Problem Retrieval.....81

5.2 Experiment Results and Discussion.....82

6 Conclusions and Future Prospect of This Thesis Study 92

References 97

List of Tables

2-1 The material parameters of LC used for the simulation.....33

3-1 The LC cell and material parameters used in this experiment.....42

3-2 The response times of each cells are given.....45

3-3 The optical images of the two line-patterned cells at different delay times.....48

4-1 Comparison of the calculation results with the two different methods based on Eq. (4.25) and Eq. (4.26). Eq. (4.26) is calculated to the fourth order of Taylor expansion.....73

List of Figures

1-1 (a) Different shapes of liquid crystal molecules. (b) The molecular alignments in the SmC, SmA, and the nematic phases.....1

1-2 An example to describe nematic LC with an averaged molecular direction picture.....3

1-3 Two cases of the distribution function of molecular orientation θ_m with (a) high orientational order, (b) low orientational order.....4

1-4 Three kinds of deformation commonly existing in a liquid crystal medium.....6

1-5 A diagram showing ordinary and extraordinary rays in a LC medium.....8

1-6 Schematic showing the way to generate on and off state with a positive $\Delta\varepsilon$ LC material.....9

1-7 Shcematic showing two kinds of LC alignment: (a) planar, (b) hybrid.....11

2-1 An optical beam incidents on a homogeneous anisotropic layer at an angle φ_0 ..23

2-2 Schematic showing the coordinates system and a stratified anisotropic medium between two isotropic media.....26

2-3 The flowchart of the simulation used to calculate the alignment configuration and optical response of nematic LC.....32

2-4 The simulation structure with a square of defect. (a) The mesh plot. (b) The plot of simulation result.....34

2-5 (a) The schematic showing the distribution of LC pretilt angle from the bottom to the top plate. (b) The pretilt angle distribution of a LC cell with different anchoring energies.....35

2-6 The simulation results revealing the influence of the separation of in-plane electrodes on LC alignment.....36

2-7 The calculated optical transmittance of a LC cell, which has both a homeotropic

and hybrid alignment zones inside, and the pretilt angle distribution are plotted.....37

3-1 The geometric transition of the OCB cell as applied voltage. (a) Splay configuration. (b) Bend 1 configuration. (c) Bend 2 configuration. (d) Twist configuration.....39

3-2 The schematic and the side view of our modified OCB cell.....41

3-3 (a) The setup of dynamic optical probing comprising of a delay generator to control the time delay. (b) The waveform and the trigger signal applied on the sample and the EMCCD.....43

3-4 Optical response curves of four different LC cells (homogeneous OCB, homogeneous hybrid, and $2\mu m$ - and $4\mu m$ -line patterned hybrid OCB cells....44

3-5 The optical transmittance is measured after the applied voltage is removed. The measurement results reveal the LC twist motion in each cells.....45

3-6 The optical micrographic images of the line-patterned hybrid cells. The resolution of the microscope is about $0.3\mu m$.....46

3-7 (a) The measured and calculated optical transmittance images of two line-patterned LC hybrid alignment cells in a region covering one period ($90\mu m$). (b) The measured and the simulated optical transmittance images of the $4\mu m$ -line patterned cell and the gray level profiles horizontally cut through the images at the center of the vertical position.....47

3-8 The summed gray-level value over a region covering one period in each image of Table 3-3 is plotted as a function of delay time.....49

3-9 The optical transmittance (in terms of gray-level) of the $2\mu m$ and $4\mu m$ -line patterned cells was measured under a crossed polarizer-analyzer. The summed gray-level values over the region with hybrid alignment configuration (Hybrid) and over the region with OCB splay configuration (Splay) are plotted as a

function of delay time.....50

3-10 The measured optical transmittance (in terms of gray-level) of the $2\mu m$ and $4\mu m$-line patterned cells is plotted as a function of delay time. The direction of the polarizer is aligned with the rubbing direction and the analyzer is set to cross with the polarizer.....52

3-11 The calculated optical transmittance variation (in terms of gray-level change) of a TN cell with a twist angle varying from 0° to 180°. Two TN cells with cell gaps 4 and 10 μm were used for the simulation.....52

3-12 The calculated director profile and optical transmittance of the $4\mu m$ line-patterned cell at delay time of $5ms$, $15ms$, $25ms$ and $75ms$.....53

3-13 The measured and simulated optical transmittance variation (in terms of gray-level change) is plotted as a function of delay time. The $4\mu m$ line-patterned cell was inserted between a cross polarizer-analyzer with (a) the direction of the polarizer aligning to the rubbing direction, (b) the direction of the polarizer deviating from the rubbing direction by 1.82°.....54

4-1 (a) The Stability distribution of $\mathbf{x}$. (b) The Stability distribution of $\mathbf{b}$.....60

4-2 The *L-curve* is a curve in a log-log scale with $\|\lambda \mathbf{Ix}\|^2$ on the y-axis and $\|\mathbf{Ax}-\mathbf{b}\|^2$ on the x-axis by varying λ from 10^{-5} to 1. The optimal value of λ is be chosen is at the corner of the curve labeled with the red circle.....62

4-3 The schematic showing the setup implemented to collect the data with various incident angles of light.....63

4-4 (a) Schematic showing the difference between our new approach and the HP group's method. (b) The flowchart of searching for the LC director profile with optical transmittance data.....65

4-5 The experimental setup used to measure the optical transmittance data for

inverse problem retrieval of LC director profile.....72

4-6 The schematic showing an idea that decomposes a LC cell into several layers to facilitate the calculation of optical transmittance.....73

4-7 Comparison of the retrieved LC director profiles by using different regularization methods. The transmittance data are prepared first with the finite element simulation based on Q-tensor approach and then added with one percentage of noise. (a) LC director profile retrieval by using one-constant regularization parameter λ. (b) LC director profile retrieval by using our new regularization scheme.....74

4-8 LC director profiles retrieved with the transmittance data. The data are prepared first with the finite element simulation based on Q-tensor approach and then added with 1%, 5%, 10%, 15%, 20%, 30% of noise. (a) The retrieved LC director profiles. (b) The statistics of the total deviation of the profiles to the true solution.....78

4-9 The retrieved LC director profiles with the three ranges of simulated optical transmittance data: I ($+10^\circ \sim -10^\circ$), II($+30^\circ \sim -30^\circ$), and III($+50^\circ \sim -50^\circ$)....79

5-1 The experimental setup used to measure the optical transmittance data for inverse problem retrieval of LC director profile.....81

5-2 The polarization-resolved optical transmittance measurement results T_x and T_y of the LC cell with hybrid alignment are presented by using four different input polarization states (22.5^o, 67.5^o, 112.5^o, and CP). The LC cell was applied with 0V. Two curves are included for comparison: red open squares: simulated curve with Berreman matrix technique, and blue cross symbols: the measured transmittance as a function of optical incident angle.....84

5-3 The polarization-resolved optical transmittance measurement results T_x and T_y

of the LC cell with hybrid alignment are presented by using four different input polarization states (22.5^o, 67.5^o, 112.5^o, and CP). The LC cell was applied with 2.5V. Two curves are included for comparison: red open squares: simulated curve with Berreman matrix technique, and blue cross symbols: the measured transmittance as a function of optical incident angle.....85

5-4 The polarization-resolved optical transmittance measurement results T_x and T_y of the LC cell with hybrid alignment are presented by using four different input polarization states (22.5^o, 67.5^o, 112.5^o, and CP). The LC cell was applied with 5V. Two curves are included for comparison: red open squares: simulated curve with Berreman matrix technique, and blue cross symbols: the measured transmittance as a function of optical incident angle.....86

5-5 The polarization-resolved optical transmittance measurement results T_x and T_y the OCB cell with bend-splay alignment are presented by using four different input polarization states (22.5^o, 67.5^o, 112.5^o, and CP). The LC cell was applied with 0V. Two curves are included for comparison: red open squares: simulated curve with Berreman matrix technique, and blue cross symbols: the measured transmittance as a function of optical incident angle.....87

5-6 The polarization-resolved optical transmittance measurement results T_x and T_y the OCB cell with bend-splay alignment are presented by using four different input polarization states (22.5^o, 67.5^o, 112.5^o, and CP). The LC cell was applied with 2.5V. Two curves are included for comparison: red open squares: simulated curve with Berreman matrix technique, and blue cross symbols: the measured transmittance as a function of optical incident angle.....88

5-7 The polarization-resolved optical transmittance measurement results T_x and T_y

the OCB cell with bend-splay alignment are presented by using four different input polarization states (22.5^o, 67.5^o, 112.5^o, and CP). The LC cell was applied with 5V. Two curves are included for comparison: red open squares: simulated curve with Berreman matrix technique, and blue cross symbols: the measured transmittance as a function of optical incident angle.....89

5-8 The retrieval director profiles of the hybrid cell by inverse problem method. (a) The coordinate system used to present the LC director profiles. (b) The retrieved director profiles of the hybrid cell biased at 0V, 2.5V, and 5V. Two profiles are included for comparison: red squares: retrieved profile, and blue symbols: the simulated profile calculated by the FEM with Q-tensor approach.....90

5-9 The retrieval director profiles of the OCB cell by inverse problem method. (a) The coordinate system used to present the LC director profiles. (b) The retrieved director profiles of the OCB cell biased at 0V, 2.5V, and 5V. Two profiles are included for comparison: red squares: retrieved profile, and blue symbols: the simulated profile calculated by the FEM with Q-tensor approach.....91

6-1 An example of the iterative regularization method with different iteration number…….94

6-2 Optical microscope with high NA objective can be used to simplify the data taking procedure for inverse problem retrieval. (a) The experiment setup. (b) The NA value of the objective lens for our incident angle range……96

Chapter 1

Thesis Motivation and the Introduction to the Physical and Optical Properties of LC

Liquid Crystal (LC) is an intermediate state of a matter between the isotropic liquid and the crystal. In the LC state, several phases with different molecular alignment orders can be found. LC molecules have typical shapes of rod-like, discotic-like, and bend-shape. Figure 1-1 illustrates the different phases and shapes of LC molecules. For simplicity of this thesis study, we will focus only on the rod-like LC molecules in the nematic phase. [1]

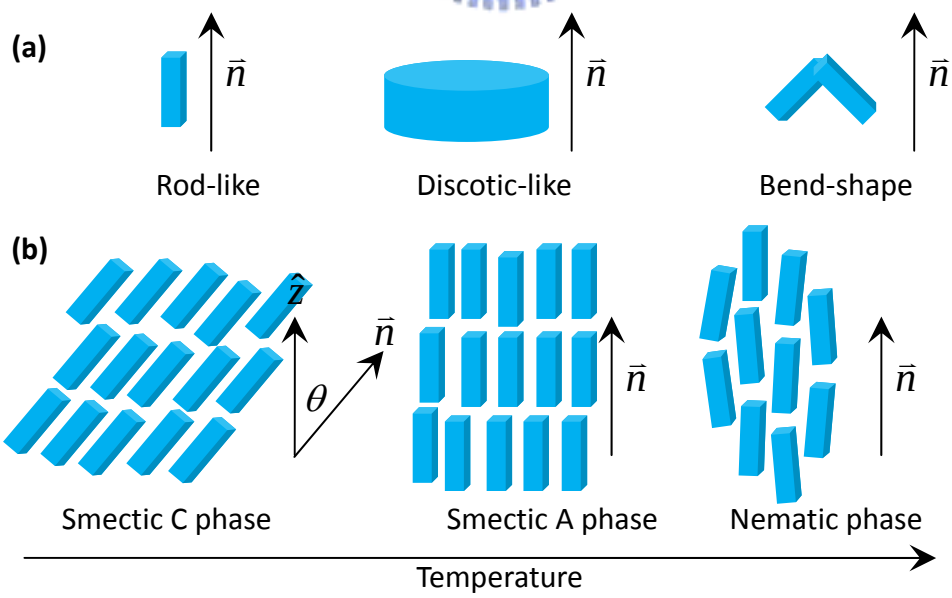

Figure 1-1 (a) Different shapes of liquid crystal molecules. (b) The molecular alignments in the SmC, SmA, and the nematic phases.

1.1 Motivation

Liquid crystal display (LCD) has been widely used in the flat panel display (FLD) industry. To satisfy the ever-increasing need for information flow and display, the next generation LC display will demand accurate control of LC configuration in each LC pixels. The static and dynamic alignment structures of liquid crystal molecules are important factors for the optical properties and response of a LC device. To probe the response of a LC device, a variety of optical techniques can be used to yield useful insight. However, the optical data are usually resulted from the entire liquid crystal layer along the propagation direction of the optical beam used. To offer the detailed information of LC director profiles and allow for the further progress of LC devices, we developed in this thesis two techniques to retrieve the LC director profiles of LC devices. We termed the first approach with a name of the model extraction. The method iteratively compares the simulation result with the measured data and retrieves the LC director profile. The second method invokes the inverse problem technique by way of optical transmittance measurement of a LC device and retrieving the LC director profile directly from the measured data. We demonstrate these two methods as in Chapters 3 and 4. However, to fulfill the objective, in the flowing we will first depict the physical and optical properties of LC materials in chapter 1 and

then in chapter 2 illustrate the models developed to simulate the LC alignment structure and the resulting optical response.

1.2 The Physics of Liquid Crystal

A rigid rod-shaped molecule is the simplest picture to be used for the description of the nematic LC. For an elongated molecule, the alignment status and the positions of the centers of mass of the molecules determine the state of matter. We can first define the averaged molecular orientation of a nematic LC, which is called director$(\vec{n})$, as shown in Figure 1-2.

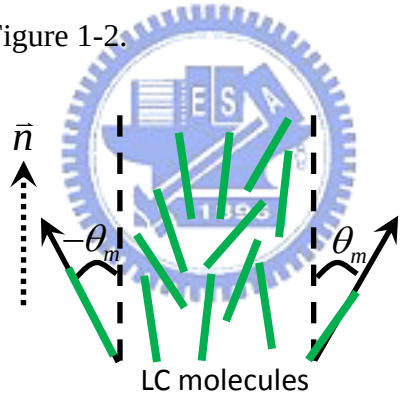

Figure 1-2. An example to describe nematic LC with an averaged molecular direction picture.

Because the director is an averaged vector over a small local volume, we need to further specify how the LC molecules angularly spread about the direction. A convenient measure of the amount of order is the *scalar order parameter*, denoted by S. This is a weighted average of the molecular alignment angles θ_m between the long

molecular axes and the director. Eq. (1.1) describes how to calculate the scalar order parameter:

$$S = \frac{1}{2}\left\langle 3\cos^2\theta_m - 1\right\rangle \quad , \tag{1.1}$$

where $\langle\ \rangle$ denotes the thermal or statistical average. Therefore, Eq. (1.1) can be rewritten as:

$$S = \frac{1}{2}\int_B \left(3\cos^2\theta_m - 1\right) f\left(\theta_m\right) dV \ , \tag{1.2}$$

where B denotes the volume of integration and $f\left(\theta_m\right)$ is the distribution function of the molecular angle θ_m. Figure 1-3 presents two cases of the distribution function $f\left(\theta_m\right)$ with a high and a low orientational order. As we can see in the Figure 1-3, because of the symmetry of molecule, $f\left(\theta_m\right)$ shall be even with $f\left(\theta_m\right) = f\left(-\theta_m\right)$ and periodic $f\left(\theta_m + \pi\right) = f\left(\theta_m\right)$. We can easily calculate a perfect crystal to have $S = 1$ and $S = 0$ for an isotropic fluid.

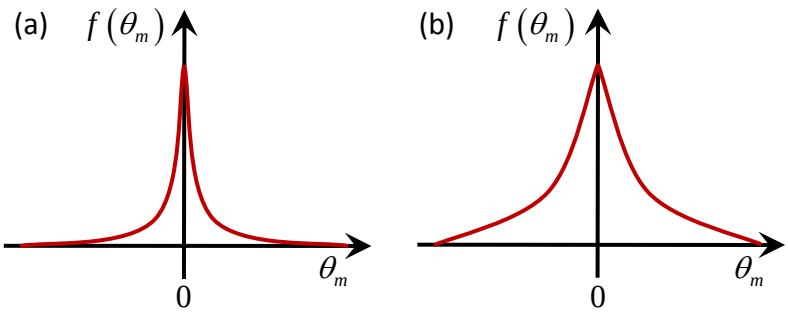

Figure 1-3 Two cases of the distribution function of molecular orientation θ_m with (a) high orientational order, (b) low orientational order.

According to the Frank-Oseen theory, the Gibbs free energy density of a nematic

LC medium can be expressed as

$$
\begin{aligned}
f_G &= f_{elastic} + f_{electric} + f_{surface} \\
&= \frac{1}{2}K_{11}\left(\nabla\cdot\vec{n}\right)^2 + \frac{1}{2}K_{22}\left(\vec{n}\cdot\nabla\times\vec{n}\right)^2 + \frac{1}{2}K_{33}\left(\vec{n}\times\nabla\times\vec{n}\right)^2 \\
&\quad -\frac{1}{2}\left(K_{22}+K_{24}\right)\nabla\cdot\left[\vec{n}\left(\nabla\cdot\vec{n}\right)+\vec{n}\times\left(\nabla\times\vec{n}\right)\right] \\
&\quad -q_0K_{22}\left(\vec{n}\cdot\nabla\times\vec{n}\right) \\
&\quad -\frac{1}{2}\left(\vec{D}\cdot\vec{E}\right) \\
&\quad +\frac{1}{2}W\left(\vec{n}-\vec{n}_0\right)^2,
\end{aligned}
\tag{1.3}
$$

by taking the elastic, the electric and the surface energy density into account. Each term can be explained as follows:

The expression at the first line, which describes the elastic deformation energy of the LC medium, is comprised of three terms representing the most important elastic distortion energies in LC: splay $\left(K_{11}\left(\nabla\cdot\vec{n}\right)^2\right)$, twist $\left(K_{22}\left(\vec{n}\cdot\nabla\times\vec{n}\right)^2\right)$, and bend $\left(K_{33}\left(\vec{n}\times\nabla\times\vec{n}\right)^2\right)$ with three corresponding elastic constants. K_{24} at the second line is related to the surface anchoring energy and q_0 at the third line is the chirality of the LC. Figure 1-4 shows the LC molecular alignment with the three different elastic deformations. In fact, the elastic constants in a typical LC material are very small in the order of *pN*, implying that LC material is quite easy to be influenced by an external force field.

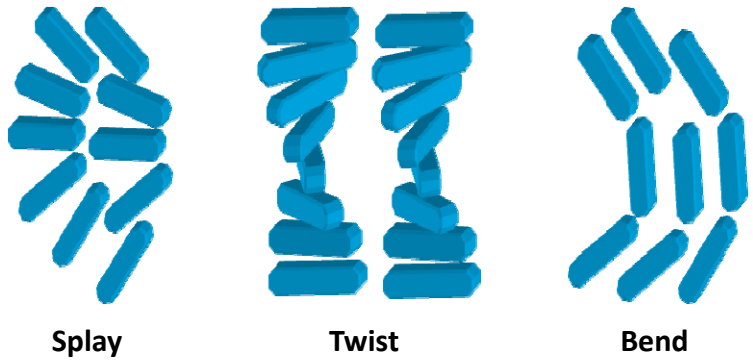

Figure 1-4. Three kinds of deformation commonly existing in a liquid crystal medium.

The expression at the fourth line describes how the LC molecules interact with an electric field. This is the foundation of LC applications. For LC with dielectric constants, $\varepsilon_{\parallel}$ (parallel to the molecular long axis) and $\varepsilon_{\perp}$ (perpendicular to the molecular long axis), we can relate the electric energy $f_{electric}$ to the LC director by using

$$\begin{aligned} f_{electric} &= -\frac{1}{2}\left(\vec{D}\cdot\vec{E}\right) \\ &= -\frac{1}{2}\left(\varepsilon_0\vec{\varepsilon}\,\nabla V\cdot\nabla V\right), \end{aligned} \tag{1.4}$$

where $\vec{\varepsilon}$ is the dielectric tensor of LC, and can be conveniently expressed as $\varepsilon_{ij} = \varepsilon_{\perp}\delta_{ij} + \Delta\varepsilon n_i n_j \quad (i, j = x, y, z)$, with $\Delta\varepsilon = \varepsilon_{\parallel} - \varepsilon_{\perp}$ and δ_{ij} the Kronecker delta, which is 1 if *i* equals *j*, and 0 otherwise.

The expression at the fifth line is the surface energy or called surface anchoring energy, where $\vec{n}_0$ denotes the prefer alignment direction of LC molecules on surface

and W is the surface anchoring strength. A useful model of surface anchoring energy is Rapini-Papoular form [2].

In a physical system, the equilibrium stable state tends to have a structure with minimum free energy. Thus, we can use this property to calculate the director configuration by minimizing the free energy density of LC. We can use the functional minimization technique to yield the result that the target functionals shall satisfy the Euler-Lagrange equations:

$$\begin{aligned} &\frac{\partial f_G}{dn_i} - \frac{d}{dx}\left(\frac{\partial f_G}{dn_{i,x}}\right) - \frac{d}{dy}\left(\frac{\partial f_G}{dn_{i,y}}\right) - \frac{d}{dz}\left(\frac{\partial f_G}{dn_{i,z}}\right) = 0, \text{ and} \\ &\frac{\partial f_G}{dV} - \frac{d}{dx}\left(\frac{\partial f_G}{dV_{,x}}\right) - \frac{d}{dy}\left(\frac{\partial f_G}{dV_{,y}}\right) - \frac{d}{dz}\left(\frac{\partial f_G}{dV_{,z}}\right) = 0, \end{aligned} \tag{1.5}$$

where f_G is the Gibbs free energy density describing by Eq. (1.3).

1.3 The Optical Properties of Liquid Crystal

LC has been widely used in fat panel display industry due to its attractive visco-elastic and electro-optical characteristics. To reveal its unique properties, we will study in this section the electro-optical behavior of LC under an electric field.

Nematic LC is an optical uniaxial medium with birefringence characterizing by two principal refractive indices. The refractive index, which is given by $n = \frac{c}{\upsilon}$, is inverse proportional to the velocity of light, υ, traveling in the medium, and c denoting for the velocity of light in vacuum. So, when an optical beam is incident at a

nematic LC film, it would experience two different velocities inside the LC, which we called ordinary-ray and extraordinary-ray. Therefore, a phase retardation will be experienced between the o-ray and e-ray in the LC film. Figure 1-5 illustrates how we can convert a unpolarized light into a polarized light by using a LC cell.

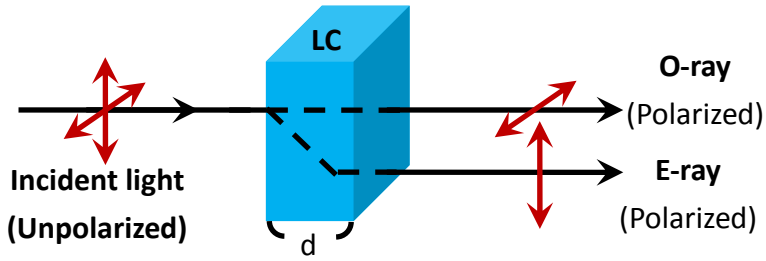

Figure 1-5 A diagram showing ordinary and extraordinary rays in a LC medium.

We can introduce ordinary and extraordinary refractive indices and birefringence as:

$$n_o = \sqrt{\varepsilon_\perp},\ n_e = \sqrt{\varepsilon_\parallel},\ \Delta n = n_e - n_o. \tag{1.6}$$

From Eq. (1.4) and Eq. (1.6), we found that the dielectric constants and refractive indexes can be affected by electric field. Figure 1-6 describes a general operational principle of LC applications.

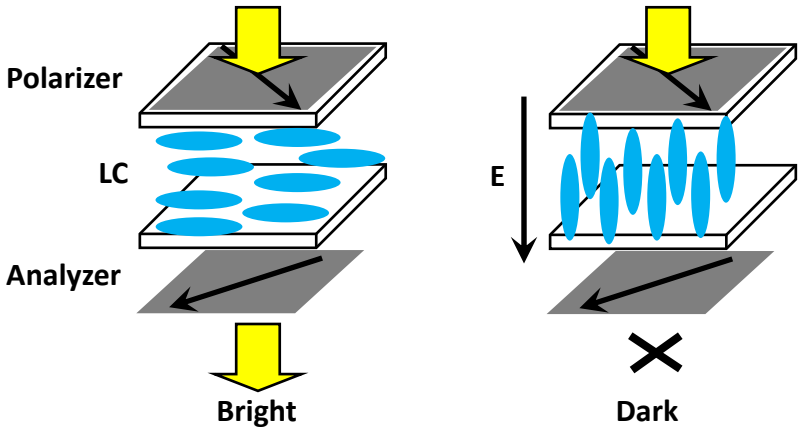

Figure 1-6. Schematic showing the way to generate on and off state with a positive $\Delta\varepsilon$ LC material.

The propagation of a polarized optical beam in a LC cell can be properly described with Jones matix formalism [3]. For an analysis, we first introduce a coordinate system with x- and y-axis lying on the plane of the LC cell. A Jones vector is used to describe the state of polarization of light with a complex envelope that represents the amplitude and phase of the optical field:

$$\mathbf{V} = \begin{pmatrix} V_x \\ V_y \end{pmatrix} = \begin{pmatrix} V_{x0}\, e^{i\varphi_x} \\ V_{y0}\, e^{i\varphi_y} \end{pmatrix}. \tag{1.7}$$

The resulting intensity is given by:

$$I = \mathbf{V}\mathbf{V}^* = |V_x|^2 + |V_y|^2 . \tag{1.8}$$

By the description, we can construct a Jones matrix to connect the incoming and the outgoing wave in a vector form:

$$\mathbf{V}_{\mathbf{out}} = \mathbf{J}\mathbf{V}_{\mathbf{in}} = \begin{pmatrix} J_{11} & J_{12} \\ J_{21} & J_{22} \end{pmatrix} \mathbf{V}_{\mathbf{in}}, \tag{1.9}$$

When calculating light propagation through a birefringent slab with thickness d and

refractive indices n_1 and n_2, inserted between crossed polarizers. By taking into account the optical axis of the LC cell relative to the laboratory frame, we can derive an expression for the system in Jones matrix representation:

$$\mathbf{V_{out}} = \mathbf{P_y R}(-\varphi)\mathbf{J_{slab}}\mathbf{R}(\varphi)\mathbf{P_x V_{in}}, \tag{1.10}$$

where $\mathbf{P_i}(i = x, y)$ denotes the polarizer, $\mathbf{R}(\varphi)$ is the rotation matrix, and φ is the angle of the optical axis of the birefringent slab relative to the x-axis of the laboratory frame. By substituting each matrix into Eq. (1.10), the result becomes:

$$\begin{aligned}\begin{pmatrix} V_x^{out} \\ V_y^{out} \end{pmatrix} &= \begin{pmatrix} 0 & 0 \\ 0 & 1 \end{pmatrix}\begin{pmatrix} \cos\varphi & -\sin\varphi \\ \sin\varphi & \cos\varphi \end{pmatrix}\begin{pmatrix} e^{-\frac{2\pi i}{\lambda}n_1 d} & 0 \\ 0 & e^{-\frac{2\pi i}{\lambda}n_1 d} \end{pmatrix}\begin{pmatrix} \cos\varphi & \sin\varphi \\ -\sin\varphi & \cos\varphi \end{pmatrix}\begin{pmatrix} 1 & 0 \\ 0 & 0 \end{pmatrix}\begin{pmatrix} V_x^{in} \\ V_y^{in} \end{pmatrix} \\ &= \begin{pmatrix} 0 \\ iV_x^{in} e^{-\frac{\pi i}{\lambda}(n_1+n_2)d} \sin(2\varphi)\sin\left(\frac{\pi(n_1-n_2)d}{\lambda}\right) \end{pmatrix}.\end{aligned} \tag{1.11}$$

From Eq. (1.8) and Eq. (1.11), we can further obtain the output light intensity:

$$\begin{aligned} I &= |V_x|^2 + |V_y|^2 \\ &= \left| iV_x^{in} e^{-\frac{\pi i}{\lambda}(n_1+n_2)d} \sin(2\varphi)\sin\left(\frac{\pi(n_1-n_2)d}{\lambda}\right)\right|^2 . \\ &= \left(V_x^{in}\right)^2 \sin^2(2\varphi)\sin^2\left(\frac{\pi(n_1-n_2)d}{\lambda}\right). \end{aligned} \tag{1.12}$$

Eq. (1.12) is useful to analyze the light propagation through a LC slab (Figure 1-7(a)). For a planar aligned LC with a pretilt angle θ with respect to the cell surface, the optical plane wave traveling through the LC cell will experience an effective refractive index of

$$n_{eff} = \frac{n_e n_o}{\sqrt{n_e^2 \sin^2\theta + n_o^2 \cos^2\theta}}. \tag{1.13}$$

By substituting $n_1 = n_{eff}$ and $n_2 = n_o$ into Eq. (1.12), it becomes:

$$I = \left(V_x^{in}\right)^2 \sin^2(2\varphi) \sin^2\left(\frac{\pi d}{\lambda}\left(\frac{n_e n_o}{\sqrt{n_e^2 \sin^2\theta + n_o^2 \cos^2\theta}} - n_o\right)\right). \tag{1.14}$$

For a hybrid LC cell (see Figure 1.7(b)) with a LC director profile a linear variation of distance, we can derive the output light intensity to be

$$I = \left(V_x^{in}\right)^2 \sin^2(2\varphi) \sin^2\left(\frac{\pi}{\lambda}\left(\int_0^d \frac{n_e n_o}{\sqrt{n_e^2 \sin^2\theta(z) + n_o^2 \cos^2\theta(z)}} dz - dn_o\right)\right). \tag{1.15}$$

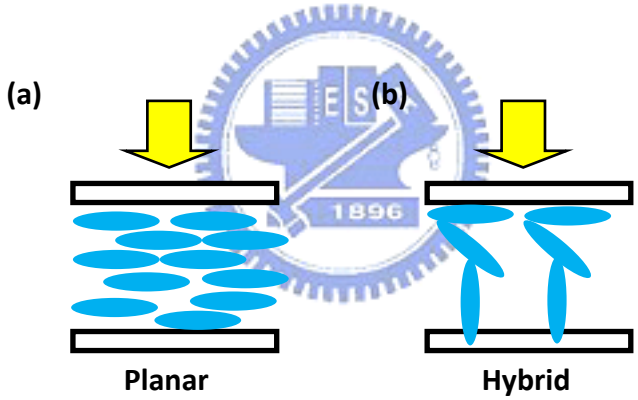

Figure 1-7. Shcematic showing two kinds of LC alignment: (a) planar, (b) hybrid.

Chapter 2

Models of the LC Alignment Structure and the Optical Response

Over the past several years, liquid crystal has been widely used for information display applications. As the technology becomes more and more sophisticated, computer simulation on LC devices becomes more important. Simulation can help researchers probing into the static and dynamic behaviors of LC and the optical properties thereafter. By calculating the director configuration and optical response of LC, we can predict what kinds of defects might develop and what optical responses could be yielded. To compute the director profile, it is required to express the free energy density of LC as shown in Eq. (1.3). By minimizing the free energy density, the LC alignment configuration can be obtained.

We found in Eq. (1.3) that it does not include the order parameter, S, which is one of the important parameters of nematic LC. By including the order parameter S into the free energy density, the defect formation can be described with the solution in a more intuitive way. In addition, we also discover that Eq. (1.3) is in the vector representation. The free energy density expression may have different values for n

and $-n$ [4]. However, for a real nematic LC, n and $-n$ shall be equivalent and possess the same free energy based on the symmetry argument. By using the Landau-de Gennes's Q-tensor representation of free energies [5, 6] to calculate the LC director configuration, the above-mentioned difficulty can be avoided. The equivalence between the Frank-Oseen's vector representation and Landau-de Gennes's Q-tensor representation has been proved by Dickman [7].

Once we have retrieved the director profile of a nematic LC, we can analyze its optical response to reveal more useful information for its application properties. In the chapter 1, we have introduced the Jones matrix method which is a powerful tool to analyze the optical properties of a layer-stacked medium at normal incidence. But to calculate the optical properties of a layer-stacked medium at high incident angle with multiple reflections, the Jones matrix method does not give a precise result. For this reason, we choose the Berreman 4×4 matrix method [8], which is based on the assumption of plane wave propagation in a stratified medium.

2.1 The *Q*-Tensor Formalism

Consider the 3×3 matrix,

$$\mathbf{M} = S\left(\vec{n}\otimes\vec{n}\right), \tag{2.1}$$

where S is the scalar order parameter, and the operator $\otimes$ indicates a

mathematical operation on the director vector $\vec{n} = \left(n_x, n_y, n_z\right)$ with the rule

$$\vec{n} \otimes \vec{n} = \begin{pmatrix} n_x n_x & n_x n_y & n_x n_z \\ n_y n_x & n_y n_y & n_y n_z \\ n_z n_x & n_z n_y & n_z n_z \end{pmatrix}. \tag{2.2}$$

We note that the director vector is an unit vector with $|\vec{n}| = 1$ and this makes the trace of $\mathbf{M}$ to be S. The other property of the matrix $\mathbf{M}$ is the symmetric property. We can then define *Q*-tensor as

$$\mathbf{Q} = S\left(\vec{n} \otimes \vec{n} - \frac{1}{3}\mathbf{I}\right), \tag{2.3}$$

which is symmetric and traceless. With the definition, we can derive the *Q*-tensor formalism of free energy from the Frank-Oseen free energy density.

We first define some elastic free energy density parameters, corresponding to each terms present in Eq. (1.3):

$$\begin{aligned} F_1 &= (\nabla \cdot \vec{\mathbf{n}})^2 \\ F_2 &= (\vec{\mathbf{n}} \cdot \nabla \times \vec{\mathbf{n}})^2 \\ F_3 &= (\vec{\mathbf{n}} \times \nabla \times \vec{\mathbf{n}})^2 \\ F_4 &= \nabla \cdot [\vec{\mathbf{n}}(\nabla \cdot \vec{\mathbf{n}}) + \vec{\mathbf{n}} \times (\nabla \times \vec{\mathbf{n}})] \\ F_5 &= \vec{\mathbf{n}} \cdot \nabla \times \vec{\mathbf{n}} \end{aligned} \tag{2.4}$$

and then construct the following vectors:

$$\begin{aligned} \mathbf{F} &= [F_1, F_2, F_3, F_4, F_5]^T \\ \mathbf{K_F} &= [\frac{K_{11}}{2}, \frac{K_{22}}{2}, \frac{K_{33}}{2}, -\frac{K_{22} + K_{24}}{2}, -q_0 K_{22}]^T. \end{aligned} \tag{2.5}$$

By using Eq. (2.4) and Eq. (2.5), we can rewrite the elastic free energy density in an inner product of row and column matrices by

$$f_{elastic} = \mathbf{K_F^T} \cdot \mathbf{F}. \tag{2.6}$$

In the next step, some convenient parameters, which are bilinear forms of the elastic free energy density parameters defined in Eq. (2.4), can be defined

$$f_1 = \left(n_{j,j}\right)^2,\ f_2 = n_{j,k}n_{j,k},\ f_3 = n_j n_k n_{l,j} n_{j,k},\ f_4 = n_{j,k}n_{k,j},\ f_5 = n_j n_{l,k} e_{jkl}, \tag{2.7}$$

where Einstein summation convention is invokes, e_{jkl} is the Levi-Civita symbol defined by $e_{xyz} = e_{yzx} = e_{zxy} = 1, e_{xzy} = e_{yxz} = e_{zyx} = -1,$ and all other $e_{jkl} = 0$, and $n_{j,k}$ is defined as:

$$n_{j,k} = \frac{\partial n_j}{\partial k}, \quad j,k \in \{x, y, z\}. \tag{2.8}$$

We prepared a vector **f** that possesses the components of Eq. (2.7):

$$\mathbf{f} = \left[f_1, f_2, f_3, f_4, f_5\right]^T. \tag{2.9}$$

The relationship between the two vectors $\mathbf{F}$ and $\mathbf{f}$ can be found

$$\mathbf{F} = \mathbf{A}\mathbf{f}, \tag{2.10}$$

with

$$\mathbf{A} = \begin{bmatrix} 1 & 0 & 0 & 0 & 0 \\ 0 & 1 & -1 & -1 & 0 \\ 0 & 0 & 1 & 0 & 0 \\ 1 & 0 & 0 & -1 & 0 \\ 0 & 0 & 0 & 0 & 1 \end{bmatrix}. \tag{2.11}$$

After the necessary preparation, the elastic free energy density in Eq. (1.3) can be expressed as a linear combination of the vector $\mathbf{f}$ and an elastic constant vector $\mathbf{K_f}$:

$$f_s = \mathbf{K_F^T F} = \mathbf{K_F^T A f} = \mathbf{K_f^T f}. \tag{2.12}$$

Here $\mathbf{K_f}$ can be obtained by:

$$\mathbf{K_f} = \mathbf{A^T K_F}$$
$$= \left[\frac{K_{11} - K_{22} - K_{24}}{2}, \frac{K_{22}}{2}, \frac{K_{33} - K_{22}}{2}, \frac{K_{24}}{2}, -q_0 K_{22} \right]^T . \tag{2.13}$$

We can define bilinear Q-tensor terms by using the same approach detailed in Eq. (2.7):

$$\begin{aligned} G_1 &= Q_{jk,l} Q_{jk,l}, \\ G_2 &= Q_{jk,k} Q_{jl,l}, \\ G_3 &= Q_{jk,l} Q_{jl,k}, \\ G_4 &= e_{jkl} Q_{jm} Q_{km,l}, \text{ and} \\ G_5 &= Q_{jk} Q_{lm,j} Q_{lm,k} \end{aligned} \tag{2.14}$$

where $Q_{jk} = S\left(n_j n_k - \frac{\delta_{jk}}{3} \right)$, δ_{jk} is Kronecker's delta, and S is the scalar order parameter. We then define a vector in terms of the bilinear Q-tensor components as:

$$\mathbf{g} = \left[\frac{G_1}{S^2}, \frac{G_2}{S^2}, \frac{G_3}{S^2}, \frac{G_4}{S^2}, \frac{G_5}{S^3} \right]^T . \tag{2.15}$$

The relationship between $\mathbf{f}$ and $\mathbf{g}$ is now clear to be

$$\mathbf{g} = \mathbf{Bf} \tag{2.16}$$

with

$$\mathbf{B} = \begin{bmatrix} 0 & 2 & 0 & 0 & 0 \\ 1 & 0 & 1 & 0 & 0 \\ 2 & \frac{2}{3} & 1 & 1 & 0 \\ 0 & 0 & 0 & 0 & -1 \\ 0 & -1 & 3 & 0 & 0 \end{bmatrix}. \tag{2.17}$$

By defining a new elastic constant vector $\mathbf{K_g}$ for vector $\mathbf{g}$, the elastic free energy density can be rewritten as:

$$f_s = \mathbf{K}_\mathbf{g}^\mathbf{T}\mathbf{g} = \mathbf{K}_\mathbf{g}^\mathbf{T}\mathbf{B}\mathbf{f} = \mathbf{K}_\mathbf{g}^\mathbf{T}\mathbf{B}\mathbf{A}^{-1}\mathbf{F}. \tag{2.18}$$

Comparing Eq. (2.6), Eq. (2.12) and Eq. (2.18), we obtain

$$\mathbf{K}_\mathbf{g} = \mathbf{B}^{-\mathbf{T}}\mathbf{A}^\mathbf{T}\mathbf{K}_\mathbf{F} = \mathbf{B}^{-\mathbf{T}}\mathbf{K}_\mathbf{f} \tag{2.19}$$

where $\mathbf{B}^{-\mathbf{T}} = \left(\mathbf{B}^{-1}\right)^\mathbf{T} = \left(\mathbf{B}^\mathbf{T}\right)^{-1}$. By using Eq. (2.13) and Eq. (2.17), we can also find that

$$\mathbf{K}_\mathbf{g} = \begin{bmatrix} \frac{1}{12}\left(K_{33} - K_{11} + 3K_{22}\right) \\ \frac{1}{2}\left(K_{11} - K_{22} - 3K_{24}\right) \\ \frac{1}{2}K_{24} \\ q_0 K_{22} \\ \frac{1}{6}\left(K_{33} - K_{11}\right) \end{bmatrix}^\mathbf{T} \tag{2.20}$$

Finally, by substituting Eq. (2.15) and Eq. (2.20) into Eq. (2.18), the Q tensor representation of the elastic free energy density becomes

$$\begin{aligned} f_s = {} & \frac{1}{12}\left(K_{33} - K_{11} + 3K_{22}\right)\frac{G_1}{S^2} + \frac{1}{2}\left(K_{11} - K_{22} - 3K_{24}\right)\frac{G_2}{S^2} + \frac{1}{2}K_{24}\frac{G_3}{S^2} \\ & + q_0 K_{22}\frac{G_4}{S^2} + \frac{1}{6}\left(K_{33} - K_{11}\right)\frac{G_5}{S^3} \end{aligned} \tag{2.21}$$

To include the electric free energy density of Eq. (1.4) into Eq. (2.21), we can express it in terms of the *Q*-tensor representation by following the Einstein summation convention

$$
\begin{aligned}
f_{electric} &= \frac{1}{2}\varepsilon_0\left(\bar{\varepsilon}V_{,j}^2 + \Delta\varepsilon V_{,j}V_{,k}\frac{Q_{jk}}{S}\right),\\
\bar{\varepsilon} &= \frac{2\varepsilon_\perp + \varepsilon_\parallel}{3},\\
\Delta\varepsilon &= \varepsilon_\perp - \varepsilon_\parallel,\\
V_{,j} &= \frac{\partial V}{\partial j}.
\end{aligned}
\tag{2.22}
$$

For the surface free energy density, the Q-tensor representation is

$$
f_{surface} = \frac{W}{2S_s^2}\left(\mathbf{Q}-\mathbf{Q_s}\right)^2, \tag{2.23}
$$

where S_s is the preferred surface order parameter. Thus, by combining Eq. (2.21), Eq. (2.22), and Eq. (2.23) together, we finally obtain the Euler-Lagrange equation in the Q-tensor representation

$$
\begin{aligned}
&\frac{\partial f_G}{dQ_{jk}} - \frac{d}{dx}\left(\frac{\partial f_G}{dQ_{jk,x}}\right) - \frac{d}{dy}\left(\frac{\partial f_G}{dQ_{jk,y}}\right) - \frac{d}{dz}\left(\frac{\partial f_G}{dQ_{jk,z}}\right) = 0,\\
&\text{and}\\
&\frac{\partial f_G}{dV} - \frac{d}{dx}\left(\frac{\partial f_G}{dV_{,x}}\right) - \frac{d}{dy}\left(\frac{\partial f_G}{dV_{,y}}\right) - \frac{d}{dz}\left(\frac{\partial f_G}{dV_{,z}}\right) = 0.
\end{aligned}
\tag{2.24}
$$

We can calculate the director profile of LC with the Q-tensor formalism. For example, by solving the eigen-modes of Eq. (2.24) we can produce the static LC director profiles for our LC design. The LC dynamic response is also an important issue for LC application. By using Erickson-Leslie theory and neglecting the inertial momentum of LC molecules, the dynamic visco-elastic behaviors of nematic LC can be analyzed with a modified version of Eq. (2.24) shown below

$$\gamma \frac{\partial Q_{jk}}{\partial t} = -\left(\frac{\partial f_G}{dQ_{jk}} - \frac{d}{dx}\left(\frac{\partial f_G}{dQ_{jk,x}} \right) - \frac{d}{dy}\left(\frac{\partial f_G}{dQ_{jk,y}} \right) - \frac{d}{dz}\left(\frac{\partial f_G}{dQ_{jk,z}} \right) \right),$$
$$\frac{\partial f_G}{dV} - \frac{d}{dx}\left(\frac{\partial f_G}{dV_{,x}} \right) - \frac{d}{dy}\left(\frac{\partial f_G}{dV_{,y}} \right) - \frac{d}{dz}\left(\frac{\partial f_G}{dV_{,z}} \right) = 0, \tag{2.25}$$

where γ denotes the rotational viscosity of nematic LC.

We examined Q tensor in Eq. (2.3) and found that it meets the following two criteria: zero trace ($\sum_i Q_{ii} = 0$) and a unit vector ($\sum_i n_{ii} = 1$) of LC director. Based on our experience of calculating the director profile under an electric field, we often encountered that our solution cannot converge and LC director is not a unit vector during iteration. These difficulties had also been reported in literature [9]. Therefore, to solve Eq. (2.25), the conditions of zero trace ($\sum_i Q_{ii} = 0$) and a unit vector ($\sum_i n_{ii} = 1$) of LC must be maintained at each time step. To meet the traceless condition, we renew the diagonal terms of Q tensor with the replacing scheme

$$Q_{ii}^{new} = Q_{ii}^{old} - \frac{Trace\left(\mathbf{Q}^{\mathbf{old}}\right)}{3}. \tag{2.26}$$

For the normalization condition of LC director, it can be implemented simply as:

$$n_i^{new} = \frac{n_i^{old}}{\sqrt{n_x^2 + n_y^2 + n_z^2}}. \tag{2.27}$$

We also derive new off-diagonal components of Q tensor to be

$$
\begin{aligned}
Q_{ij}^{new} &= S'\left(\frac{n_i n_j}{n_x^2+n_y^2+n_z^2}\right) \\
&= S'(n_i n_j)\times\frac{1}{(n_x^2+n_y^2+n_z^2)} \\
&= S'(n_i n_j)\times\frac{S'}{S'(n_x^2+n_y^2+n_z^2-1)+S'} \\
&= Q^{old}\left(\frac{S'}{S'+Trace\left(\mathbf{Q}^{\mathbf{old}}\right)}\right).
\end{aligned}
\tag{2.28}
$$

For the diagonal components of Q tensor, the following normalization conditions can be used

$$
\begin{aligned}
Q_{ii}^{new} &= S'\left(\frac{n_i^2}{n_x^2+n_y^2+n_z^2}-\frac{1}{3}\right) \\
&= S'\left(\frac{n_i^2}{n_x^2+n_y^2+n_z^2}-\frac{n_x^2+n_y^2+n_z^2}{3(n_x^2+n_y^2+n_z^2)}\right) \\
&= S'\left(n_i^2-\frac{n_x^2+n_y^2+n_z^2}{3}\right)\times\frac{1}{(n_x^2+n_y^2+n_z^2)} \\
&= S'\left(n_i^2-\frac{1}{3}-\frac{(n_x^2+n_y^2+n_z^2-1)}{3}\right)\times\frac{S'}{S'(n_x^2+n_y^2+n_z^2-1)+S'} \\
&= \left(S'\left(n_i^2-\frac{1}{3}\right)-S'\frac{(n_x^2+n_y^2+n_z^2-1)}{3}\right)\times\frac{S'}{S'(n_x^2+n_y^2+n_z^2-1)+S'} \\
&= \left(Q^{old}-\frac{Trace\left(\mathbf{Q}^{\mathbf{old}}\right)}{3}\right)\left(\frac{S'}{S'+Trace\left(\mathbf{Q}^{\mathbf{old}}\right)}\right).
\end{aligned}
\tag{2.29}
$$

The S' in Eq. (2.28) and Eq. (2.29) is not the same value as we use at the beginning of simulation. To illustrate this problem, let us take a look at the Q tensor at the beginning:

$$\mathbf{Q}=\begin{bmatrix} S(n_x n_x-\frac{1}{3}) & S(n_x n_y) & S(n_x n_z) \\ S(n_y n_x) & S(n_y n_y-\frac{1}{3}) & S(n_y n_z) \\ S(n_z n_x) & S(n_z n_y) & S(n_z n_z-\frac{1}{3}) \end{bmatrix}. \tag{2.30}$$

It is clear that Eq. (2.30) has the following eigenvalues

$$\lambda=\begin{bmatrix} -\frac{S}{3} & -\frac{S}{3} & \frac{[-S+3S(n_x^2+n_y^2+n_z^2)]}{3} \end{bmatrix}=\begin{bmatrix} -\frac{S}{3} & -\frac{S}{3} & \frac{2S}{3} \end{bmatrix}. \tag{2.31}$$

The new S' therefore shall be evaluated with the eigenvalues of $\mathbf{Q}^{\mathbf{old}}$ instead of using the initial value at the beginning.

2.2 The Berreman Matrix Method

Based on the Maxwell's equations

$$\begin{aligned} &\nabla\times\mathbf{E}=-\frac{\partial\mathbf{B}}{\partial t}, \\ &\nabla\times\mathbf{H}=-\frac{\partial\mathbf{D}}{\partial t}, \\ &\nabla\cdot\mathbf{B}=0, \text{ and} \\ &\nabla\cdot\mathbf{D}=0, \end{aligned} \tag{2.32}$$

we can describe the wave propagation in a layered medium in a matrix formalism. This can be done by expressing curl and divergence operation as a matrix

$$\nabla\times=\begin{pmatrix} 0 & -\frac{\partial}{\partial z} & \frac{\partial}{\partial y} \\ \frac{\partial}{\partial z} & 0 & -\frac{\partial}{\partial x} \\ -\frac{\partial}{\partial y} & \frac{\partial}{\partial x} & 0 \end{pmatrix},\quad \nabla\cdot=\begin{pmatrix} \frac{\partial}{\partial x} \\ \frac{\partial}{\partial y} \\ \frac{\partial}{\partial z} \end{pmatrix}. \tag{2.33}$$

By substituting Eq. (2.33) into Eq. (2.32), the wave propagation of all field

components can be properly described as follows:

$$\begin{pmatrix} 0 & 0 & 0 & 0 & -\frac{\partial}{\partial z} & \frac{\partial}{\partial y} \\ 0 & 0 & 0 & \frac{\partial}{\partial z} & 0 & -\frac{\partial}{\partial x} \\ 0 & 0 & 0 & -\frac{\partial}{\partial y} & \frac{\partial}{\partial x} & 0 \\ 0 & \frac{\partial}{\partial z} & -\frac{\partial}{\partial y} & 0 & 0 & 0 \\ -\frac{\partial}{\partial z} & 0 & \frac{\partial}{\partial x} & 0 & 0 & 0 \\ \frac{\partial}{\partial y} & -\frac{\partial}{\partial x} & 0 & 0 & 0 & 0 \end{pmatrix} \begin{pmatrix} E_x \\ E_y \\ E_z \\ H_x \\ H_y \\ H_z \end{pmatrix} = \begin{pmatrix} \frac{\partial D_x}{\partial t} \\ \frac{\partial D_y}{\partial t} \\ \frac{\partial D_z}{\partial t} \\ \frac{\partial B_x}{\partial t} \\ \frac{\partial B_y}{\partial t} \\ \frac{\partial B_z}{\partial t} \end{pmatrix}. \tag{2.34}$$

Eq. (2.34) can be expressed in a matrix form as:

$$\mathbf{OG} = \frac{\partial \mathbf{C}}{\partial t}. \tag{2.35}$$

In the absence of spatial dispersion and nonlinear optical effects, the constitutive relations $\mathbf{D} = \varepsilon_0 \boldsymbol{\varepsilon} \mathbf{E}$ and $\mathbf{B} = \mu_0 \boldsymbol{\mu} \mathbf{H}$ can be easily included in Eq. (2.34). For simplicity, we use time harmonic optical fields, in which the $e^{i\omega t}$ factor can be taken out of the field components. Under the condition, Eq. (2.35) can be simplified as:

$$\begin{aligned} \mathbf{OG} &= \mathbf{M}\frac{\partial \mathbf{G}}{\partial t}, \\ \mathbf{O}\left(e^{i\omega t}\right)\boldsymbol{\Gamma} &= \mathbf{M}\left(i\omega e^{i\omega t}\right)\boldsymbol{\Gamma}, \text{ and} \\ \mathbf{O}\boldsymbol{\Gamma} &= i\omega \mathbf{M}\boldsymbol{\Gamma}, \end{aligned} \tag{2.36}$$

where $\mathbf{M} = \begin{pmatrix} \varepsilon_0\varepsilon_{11} & \varepsilon_0\varepsilon_{12} & \varepsilon_0\varepsilon_{13} & 0 & 0 & 0 \\ \varepsilon_0\varepsilon_{21} & \varepsilon_0\varepsilon_{22} & \varepsilon_0\varepsilon_{23} & 0 & 0 & 0 \\ \varepsilon_0\varepsilon_{31} & \varepsilon_0\varepsilon_{32} & \varepsilon_0\varepsilon_{33} & 0 & 0 & 0 \\ 0 & 0 & 0 & \mu_0\mu_{11} & \mu_0\mu_{12} & \mu_0\mu_{13} \\ 0 & 0 & 0 & \mu_0\mu_{21} & \mu_0\mu_{22} & \mu_0\mu_{23} \\ 0 & 0 & 0 & \mu_0\mu_{31} & \mu_0\mu_{32} & \mu_0\mu_{33} \end{pmatrix}$ and $\boldsymbol{\Gamma}$ is the spatial part

of $\mathbf{G}$.

As shown in Figure 2-1, we consider a monochromatic plane wave obliquely incident from an isotropic medium to a homogeneous anisotropic layer medium with the surface normal along the z-axis.

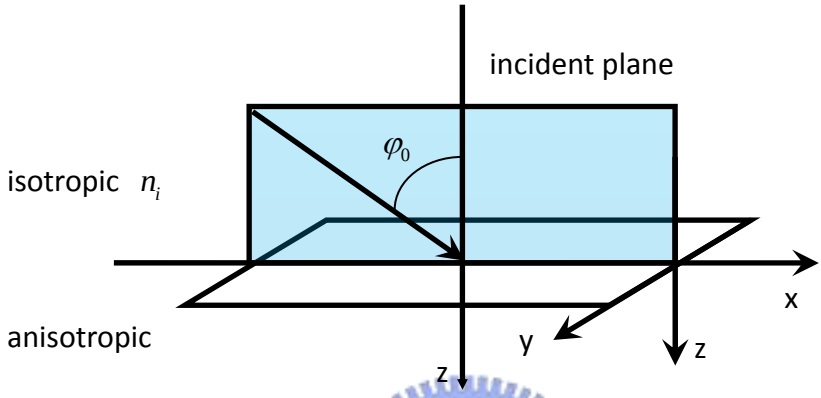

Figure 2-1. An optical beam incidents on a homogeneous anisotropic layer at an angle φ_0.

The problem is invariant along the y-direction, so all derivatives along y can be set to zero

$$\frac{\partial}{\partial y} = 0. \tag{2.37}$$

The incident plane wave $\mathbf{E} = E_0 e^{i(\omega t - \mathbf{kr})}$ must have the same spatial dependence on x. The x-component of the wave vector k_x in the ambient medium of index n_i is:

$$\xi = k_0 n_i \sin\varphi_0, \tag{2.38}$$

where φ_0 is the angle of incidence and $k_0 = \frac{\omega}{c}$. The variation of all fields in the x-direction is proportional to $e^{-i\xi x}$, so we can get:

$$\frac{\partial}{\partial x} = -i\xi. \tag{2.39}$$

We assume that the magnetic permeability $\boldsymbol{\mu}$ of a nematic LC is isotropic and the dielectric permittivity tensor can be related to the pretilt and azimuthal angle of the LC director by

$$\boldsymbol{\mu} = \begin{pmatrix} \mu & 0 & 0 \\ 0 & \mu & 0 \\ 0 & 0 & \mu \end{pmatrix}, \text{ and}$$
$$\boldsymbol{\varepsilon} = \begin{pmatrix} n_o^2 + \Delta\varepsilon\cos^2\theta\cos^2\phi & \Delta\varepsilon\cos^2\theta\sin\phi\cos\phi & \Delta\varepsilon\sin\theta\cos\theta\cos\phi \\ \Delta\varepsilon\cos^2\theta\sin\phi\cos\phi & n_o^2 + \Delta\varepsilon\cos^2\theta\sin^2\phi & \Delta\varepsilon\sin\theta\cos\theta\sin\phi \\ \Delta\varepsilon\sin\theta\cos\theta\cos\phi & \Delta\varepsilon\sin\theta\cos\theta\sin\phi & n_o^2 + \Delta\varepsilon\sin^2\theta \end{pmatrix} \tag{2.40}$$

where θ denotes the pretilt angle and ϕ denotes the azimuthal angle. Combining Eq. (2.38), Eq. (2.39) and Eq. (2.40) into Eq. (2.36), we obtain the wave propagation equations for all field components

$$\begin{pmatrix} i\omega\varepsilon_0\varepsilon_{11} & i\omega\varepsilon_0\varepsilon_{12} & i\omega\varepsilon_0\varepsilon_{13} & 0 & \frac{\partial}{\partial z} & 0 \\ i\omega\varepsilon_0\varepsilon_{21} & i\omega\varepsilon_0\varepsilon_{22} & i\omega\varepsilon_0\varepsilon_{23} & -\frac{\partial}{\partial z} & 0 & -i\zeta \\ i\omega\varepsilon_0\varepsilon_{31} & i\omega\varepsilon_0\varepsilon_{32} & i\omega\varepsilon_0\varepsilon_{33} & 0 & i\zeta & 0 \\ 0 & -\frac{\partial}{\partial z} & 0 & i\omega\mu_0\mu & 0 & 0 \\ \frac{\partial}{\partial z} & 0 & i\zeta & 0 & i\omega\mu_0\mu & 0 \\ 0 & -i\zeta & 0 & 0 & 0 & i\omega\mu_0\mu \end{pmatrix} \begin{pmatrix} E_x \\ E_y \\ E_z \\ H_x \\ H_y \\ H_z \end{pmatrix} = 0. \tag{2.41}$$

The third and the sixth row equations of Eq. (2.41) can be reduced to

$$E_z = -\frac{\xi}{\varepsilon_0\varepsilon_{33}\omega} H_y - \frac{\varepsilon_{31}}{\varepsilon_{33}} E_x - \frac{\varepsilon_{32}}{\varepsilon_{33}} E_y, \text{ and}$$
$$H_z = \frac{\xi}{\mu_0\mu\omega} E_y, \tag{2.42}$$

which show that the field components E_z and H_z are linearly dependent on the

other field components. Replacing E_z and H_z of Eq. (2.41) with of Eq. (2.42), four linear, first-order differential equations for the field components E_x, E_y, $-H_x$ (minus sign for convenience and simplicity), and H_y are obtained

$$\frac{\partial}{\partial z}\begin{pmatrix} E_x \\ H_y \\ E_y \\ -H_x \end{pmatrix} = -i\omega \begin{pmatrix} -\frac{\xi\varepsilon_{31}}{\omega\varepsilon_{33}} & \mu_0\mu - \frac{\xi^2}{\omega^2\varepsilon_0\varepsilon_{33}} & -\frac{\xi\varepsilon_{32}}{\omega\varepsilon_{33}} & 0 \\ \varepsilon_0\varepsilon_{11} - \frac{\varepsilon_0\varepsilon_{13}\varepsilon_{31}}{\varepsilon_{33}} & -\frac{\xi\varepsilon_{13}}{\omega\varepsilon_{33}} & \varepsilon_0\varepsilon_{12} - \frac{\varepsilon_0\varepsilon_{13}\varepsilon_{32}}{\varepsilon_{33}} & 0 \\ 0 & 0 & 0 & \mu_0\mu \\ \varepsilon_0\varepsilon_{21} - \frac{\varepsilon_0\varepsilon_{23}\varepsilon_{31}}{\varepsilon_{33}} & -\frac{\xi\varepsilon_{23}}{\omega\varepsilon_{33}} & \varepsilon_0\varepsilon_{22} - \frac{\varepsilon_0\varepsilon_{23}\varepsilon_{32}}{\varepsilon_{33}} - \frac{\xi^2}{\omega^2\mu_0\mu} & 0 \end{pmatrix} \begin{pmatrix} E_x \\ H_y \\ E_y \\ -H_x \end{pmatrix}, \tag{2.43}$$

or in a matrix form

$$\frac{\partial}{\partial z}\mathbf{\Psi} = -i\omega\mathbf{\Pi}\mathbf{\Psi}. \tag{2.44}$$

Here $\mathbf{\Pi}$ denotes the differential propagation matrix. Eq. (2.44) can be solved to yield an analytic solution of

$$\mathbf{\Psi}(z+h) = e^{-iwh\mathbf{\Pi}}\mathbf{\Psi}(z). \tag{2.45}$$

This yields a generalized field vector $\mathbf{\Psi}$ at $z+h$ if $\mathbf{\Psi}$ is known at z. Here h is a finite propagation distance. For a multilayer structure with a total thickness of $d = \sum_i h_i$, we obtain

$$\mathbf{\Psi}_{\mathbf{out}}(d) = e^{-iwh_n\mathbf{\Pi}_\mathbf{n}} \ldots e^{-iwh_2\mathbf{\Pi}_2} e^{-iwh_1\mathbf{\Pi}_1}\mathbf{\Psi}_{\mathbf{in}}(0). \tag{2.46}$$

Berreman matrix method can also be used to yield Fresnel equations and the reflected wave and transmitted wave. Figure 2-2 depicts the case with an anisotropic stratified

medium sandwiched between two isotropic media with indices of refraction n_0 and n_2.

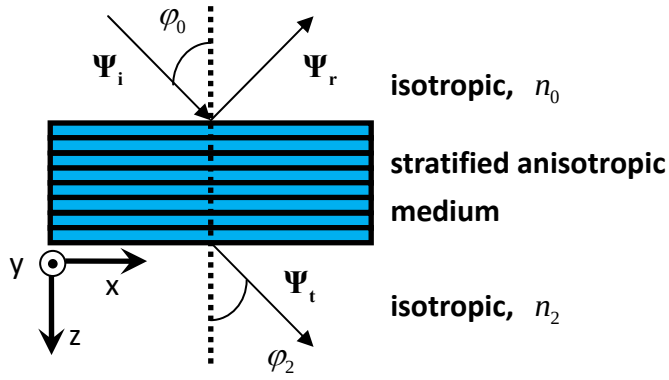

Figure 2-2. Schematic showing the coordinates system and a stratified anisotropic medium between two isotropic media.

With Fresnel equations, we can get the fields in incidence (*i*), reflection (*r*) and transmission (*t*):

$$\begin{aligned} \frac{H_{ix}}{E_{iy}} &= \frac{H_{iy}}{E_{ix}} = \sqrt{\frac{\varepsilon_0}{\mu_0}} n_0, \\ \frac{H_{rx}}{E_{ry}} &= \frac{H_{ry}}{E_{rx}} = \sqrt{\frac{\varepsilon_0}{\mu_0}} n_0, \text{ and} \\ \frac{H_{tx}}{E_{ty}} &= \frac{H_{ty}}{E_{tx}} = \sqrt{\frac{\varepsilon_0}{\mu_0}} n_2. \end{aligned} \tag{2.47}$$

According to Eq. (2.47), the generalized field vectors in each region can be found to be:

$$\mathbf{\Psi_i} = \begin{pmatrix} E_{ix}\cos\varphi_0 \\ E_{ix}\sqrt{\frac{\varepsilon_0}{\mu_0}}n_0 \\ E_{iy} \\ E_{iy}\cos\varphi_0\sqrt{\frac{\varepsilon_0}{\mu_0}}n_0 \end{pmatrix},$$

$$\mathbf{\Psi_r} = \begin{pmatrix} -E_{rx}\cos\varphi_0 \\ E_{rx}\sqrt{\frac{\varepsilon_0}{\mu_0}}n_0 \\ E_{ry} \\ -E_{ry}\cos\varphi_0\sqrt{\frac{\varepsilon_0}{\mu_0}}n_0 \end{pmatrix}, \text{ and}$$

$$\mathbf{\Psi_t} = \begin{pmatrix} E_{tx}\cos\varphi_2 \\ E_{tx}\sqrt{\frac{\varepsilon_0}{\mu_0}}n_2 \\ E_{ty} \\ E_{ty}\cos\varphi_2\sqrt{\frac{\varepsilon_0}{\mu_0}}n_2 \end{pmatrix}. \tag{2.48}$$

Thus, Eq. (2.45) can be modified to be

$$\mathbf{\Psi_t} = P(\mathbf{\Pi})\left(\mathbf{\Psi_i} + \mathbf{\Psi_r}\right), \tag{2.49}$$

where $P(\mathbf{\Pi})$ is the propagation matrix. Substituting Eq. (2.48) into Eq. (2.49), we then have:

$$\mathbf{T_2}\begin{pmatrix} E_{tx} \\ E_{ty} \\ 0 \\ 0 \end{pmatrix} = P(\mathbf{\Pi})\mathbf{T_1}\begin{pmatrix} E_{ix} \\ E_{iy} \\ E_{rx} \\ E_{ry} \end{pmatrix}, \tag{2.50}$$

which results in

$$\begin{pmatrix} E_{tx} \\ E_{ty} \\ 0 \\ 0 \end{pmatrix} = \mathbf{U_b} \begin{pmatrix} E_{ix} \\ E_{iy} \\ E_{rx} \\ E_{ry} \end{pmatrix}, \tag{2.51}$$

with

$$\mathbf{U_b} = \mathbf{T_2^{-1}} P(\mathbf{\Pi}) \mathbf{T_1}, \tag{2.52}$$

where

$$\mathbf{T_1} = \begin{pmatrix} \cos\varphi_0 & 0 & -\cos\varphi_0 & 0 \\ \sqrt{\frac{\varepsilon_0}{\mu_0}} n_0 & 0 & \sqrt{\frac{\varepsilon_0}{\mu_0}} n_0 & 0 \\ 0 & 1 & 0 & 1 \\ 0 & \cos\varphi_0 \sqrt{\frac{\varepsilon_0}{\mu_0}} n_0 & 0 & -\cos\varphi_0 \sqrt{\frac{\varepsilon_0}{\mu_0}} n_0 \end{pmatrix}, \text{ and}$$

$$\mathbf{T_2} = \begin{pmatrix} \cos\varphi_2 & 0 & 0 & 0 \\ \sqrt{\frac{\varepsilon_0}{\mu_0}} n_2 & 0 & 0 & 0 \\ 0 & 1 & 0 & 0 \\ 0 & \cos\varphi_2 \sqrt{\frac{\varepsilon_0}{\mu_0}} n_2 & 0 & 0 \end{pmatrix}.$$

The projection matrices $P(\mathbf{\Pi})$ can be found to be:

$$\mathbf{P_+} = \begin{pmatrix} 1 & 0 & 0 & 0 \\ 0 & 1 & 0 & 0 \\ 0 & 0 & 0 & 0 \\ 0 & 0 & 0 & 0 \end{pmatrix}, \text{ and}$$

$$\mathbf{P_-} = \begin{pmatrix} 0 & 0 & 0 & 0 \\ 0 & 0 & 0 & 0 \\ 0 & 0 & 1 & 0 \\ 0 & 0 & 0 & 1 \end{pmatrix}. \tag{2.53}$$

By using Eq. (2.51) and Eq. (2.53), we can derive the components of transmitted and reflected waves as:

$$\begin{pmatrix} E_{tx} \\ E_{ty} \\ 0 \\ 0 \end{pmatrix} = \mathbf{U_b} \begin{pmatrix} E_{ix} \\ E_{iy} \\ E_{rx} \\ E_{ry} \end{pmatrix}, \tag{2.54}$$

which leads to $\mathbf{P}_+ \begin{pmatrix} E_{tx} \\ E_{ty} \\ E_{rx} \\ E_{ry} \end{pmatrix} = \mathbf{U_b} \begin{pmatrix} E_{ix} \\ E_{iy} \\ 0 \\ 0 \end{pmatrix} + \mathbf{U_b} \begin{pmatrix} 0 \\ 0 \\ E_{rx} \\ E_{ry} \end{pmatrix}$ and $\mathbf{P}_+ \begin{pmatrix} E_{tx} \\ E_{ty} \\ E_{rx} \\ E_{ry} \end{pmatrix} - \mathbf{U_b}\mathbf{P}_- \begin{pmatrix} E_{tx} \\ E_{ty} \\ E_{rx} \\ E_{ry} \end{pmatrix} = \mathbf{U_b} \begin{pmatrix} E_{ix} \\ E_{iy} \\ 0 \\ 0 \end{pmatrix}$.

Therefore $\begin{pmatrix} E_{tx} \\ E_{ty} \\ E_{rx} \\ E_{ry} \end{pmatrix} = \left(\mathbf{P}_+ - \mathbf{U_b}\mathbf{P}_-\right)^{-1} \mathbf{U_b} \begin{pmatrix} E_{ix} \\ E_{iy} \\ 0 \\ 0 \end{pmatrix}$ or in the matrix notation simply as

$$\left(\mathbf{\Psi_t} + \mathbf{\Psi_r}\right) = \mathbf{B} \cdot \mathbf{\Psi_i} = \left(\mathbf{P}_+ - \mathbf{U_b}\mathbf{P}_-\right)^{-1} \mathbf{U_b}\mathbf{\Psi_i}. \tag{2.55}$$

By using Eq. (2.55), we can calculate the TM and TE components of the transmitted and reflected waves for given incident TM and TE waves.

Although the Berreman 4×4 matrix method is a fast and powerful method, it is usually difficult to be used to solve a three-dimensional problem, especially when the geometry is complex. We therefore introduce a modified Jones matrix method to analyze the light transmission for a twisted nematic (TN) LC. The theoretical derivation had been reported by the group of Oldano [10] by using a perturbative approach. The transmission matrix of a TN LC cell was found to be

$$\mathbf{T} = e^{ik_a d} \begin{pmatrix} e^{\frac{i\delta}{2}} & it \\ it^* & e^{-\frac{i\delta}{2}} \end{pmatrix}, \tag{2.56}$$

where * indicates the complex conjugation operation, $k_a = \pi\left(n_e + n_o\right)/\lambda$,

$\delta = \Delta kd = \dfrac{2\pi\left(n_e - n_o\right)d}{\lambda}$ and t is a perturbative parameter defined as

$$t = \frac{\eta}{\Delta k}\left[e^{\frac{-i\Delta kd}{2}} \left.\frac{d\phi}{dz}\right|_2 - e^{\frac{i\Delta kd}{2}} \left.\frac{d\phi}{dz}\right|_1 \right], \tag{2.57}$$

where $\left.\dfrac{d\phi}{dz}\right|_1$ and $\left.\dfrac{d\phi}{dz}\right|_2$ are the derivatives of director angle at surfaces locating at $-\dfrac{d}{2}$ and $\dfrac{d}{2}$, respectively. Combining Eq. (2.56) and Eq. (2.57), we get,

$$\mathbf{T} = \begin{bmatrix} e^{i\delta_e} & i\left(ae^{i\delta_e} + be^{i\delta_o}\right) \\ i\left(ae^{i\delta_o} + be^{i\delta_e}\right) & e^{i\delta_o} \end{bmatrix}, \tag{2.58}$$

where $\delta_e = \dfrac{2\pi n_e d}{\lambda}$, $\delta_o = \dfrac{2\pi n_o d}{\lambda}$, $a = -\dfrac{\eta_1}{\Delta k}\left.\dfrac{d\phi}{dz}\right|_1$, $b = -\dfrac{\eta_1}{\Delta k}\left.\dfrac{d\phi}{dz}\right|_2$ and $\eta_1 = \dfrac{1}{2}\left(\sqrt{\dfrac{n_e}{n_o}} + \sqrt{\dfrac{n_o}{n_e}}\right)$. By using Eq. (2.58), we can derive the electric field of output light as:

$$E_{out} = E_e^{out} e^{i\delta_e} + E_o^{out} e^{i\delta_o} \tag{2.59}$$

where

$$E_e^{out} = \left(E_e^{in} + ia\sqrt{\frac{n_o}{n_e}} E_o^{in} \right)\hat{n} + ib\sqrt{\frac{n_e}{n_o}} E_e^{in}\hat{h} \tag{2.60}$$

and

$$E_o^{out} = ib\sqrt{\frac{n_o}{n_e}} E_o^{in}\hat{n} + \left(E_o^{in} + ia\sqrt{\frac{n_e}{n_o}} E_e^{in} \right)\hat{h}. \tag{2.61}$$

The $\hat{n}$ and $\hat{h}$ in Eq. (2.60) are the unit vectors parallel and orthogonal to the director at the surface $\dfrac{d}{2}$.

2.3 The Application Examples

In this section, we combine the *Q*-tensor approach and the Berrman matrix method to analyze several application examples of LC. Finite element method (FEM) was implemented to solve the partial differential equations of Eq. (2.25) [11]. FEM has the advantages of structure-flexible simulation and less computation time than that with finite difference method. We will focus on the topics that we are interested in. The coupled partial differential equations solver is implemented with COMSOL Multiphysics [12] and is linked to MATLAB. Figure 2-3 shows the flowchart of our simulation procedure.

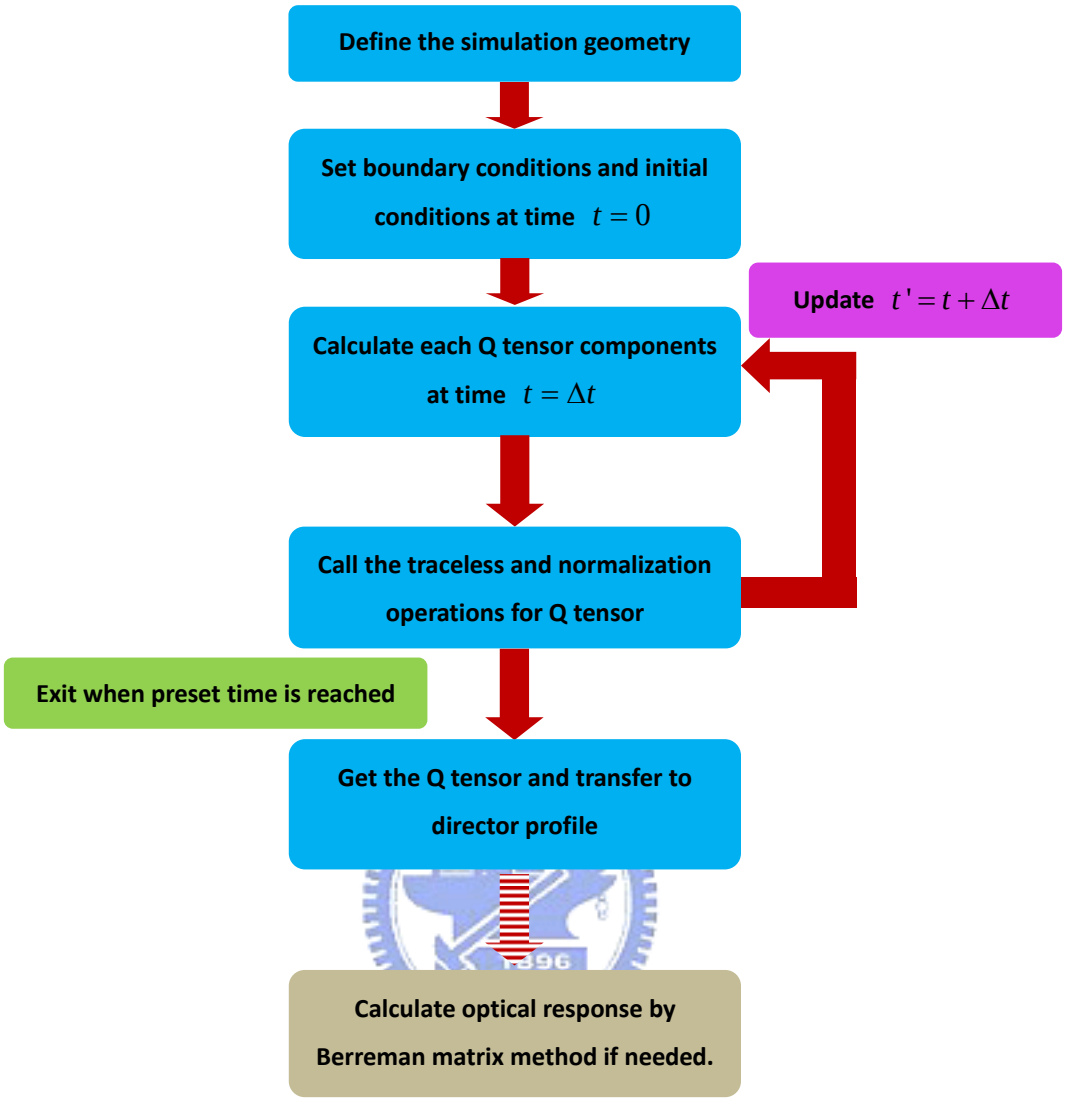

Figure 2-3. The flowchart of the simulation used to calculate the alignment configuration and optical response of nematic LC.

Example 1

In this example, we aim to design a LC cell with each side possessing a square-shaped defect of $1\mu m$ each side. The structure of the cell is depicted in Figure 2-4 (a). The material parameters of the LC used are given in Table 2-1. The

alignment layers are at the top and bottom of the cell. The cell gap is $4\mu m$. The pretilt angle for the alignment layer is 70°. We use a mesh that has a higher density near the defect region than that in the rest area. The result is shown in Figure 2-4 (b).

As we can see, the LC molecules near the both sides of the defect square can deviate from the alignment direction. The lowest pretilt angle is close to 40° which is almost 30° different from the surface condition. The affected length is around $0.7\mu m$ started from the square defect. This example illustrates that the smoothness of the substrates used is important for the fabrication of a good LC cell.

Table 2-1: The material parameters of LC used for the simulation.

K_{11}	11.3pN	n_o	1.506
K_{22}	7.7pN	γ	213 mPaS
K_{33}	15.8pN	$\varepsilon_{\parallel}$	14.1
n_e	1.675	$\varepsilon_{\perp}$	4.0

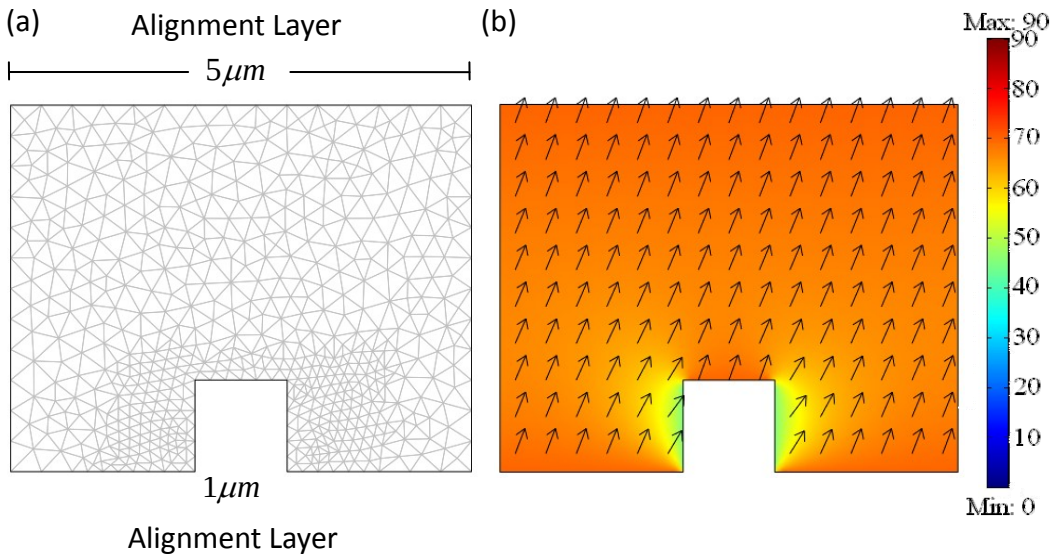

Figure 2-4. The simulation structure with a square of defect. (a) The mesh plot. (b) The plot of simulation result.

Example 2

In this example, we discuss the anchoring effect on a LC cell. We set up the LC cell with a pretilt angle of 6°. The schematic showing the distribution of LC pretilt angle from the bottom to the top plate is presented in Figure 2-5 (a). We discuss the LC alignment effect with four different surface anchoring energies: infinity, 10^{-3}, 10^{-6} and 10^{-12} (J). The result is shown in Figure 2-5(b). The infinite anchoring energy has an identical pretilt angle of 6° across the thickness of LC cell. The maximum angular deviation across the thickness by using alignment surfaces with an anchoring energy of 10^{-12} J can be as large as 2.3°. This example illustrates that the LC molecules in the center area are not fully aligned with the surface condition when the

surface anchoring energy is weak.

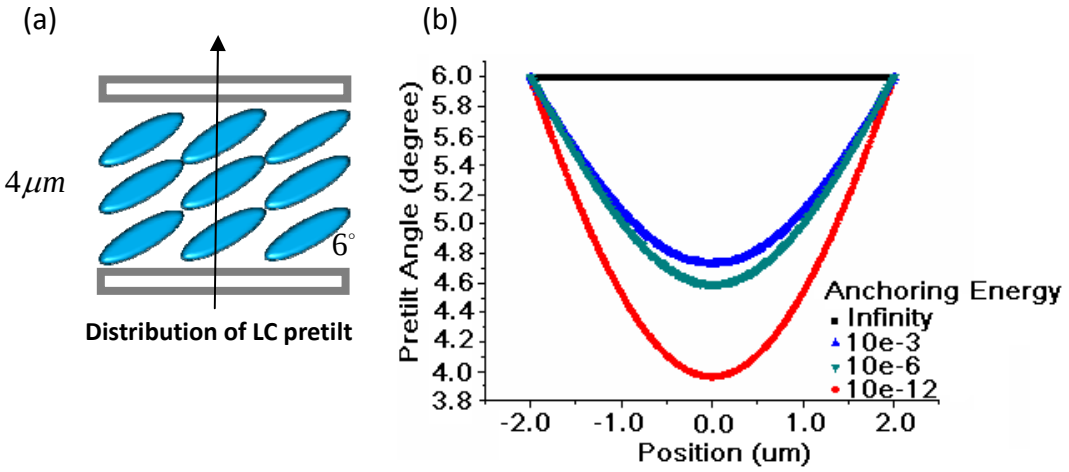

Figure 2-5. (a) The schematic showing the distribution of LC pretilt angle from the bottom to the top plate. (b) The pretilt angle distribution of a LC cell with different anchoring energies.

Example 3

In this example, we will focus on the influence of the separation of in-plane electrodes on LC alignment. We design a LC cell with a cell dimension of $28\mu m$ and a cell gap of $4\mu m$ but with two different separations of the in-plane electrodes. The electrodes lie on the top surface of the cell. By applying a voltage of 5V, the results are shown in Figure 2-5 with the pretilt angle plot and the potential contour. We find the influence range of the electric field is quite wide. The influence range for the $4\mu m$ width of the electrode is $\sim 20\mu m$ and for the $2\mu m$ is $\sim 15\mu m$. This result suggests that for a liquid crystal on silicon (LCOS), whose cell structure is similar to

this simulated cell, the inter-pixel crosstalk should be taken into account, especially when the pixel size approaches its cell gap.

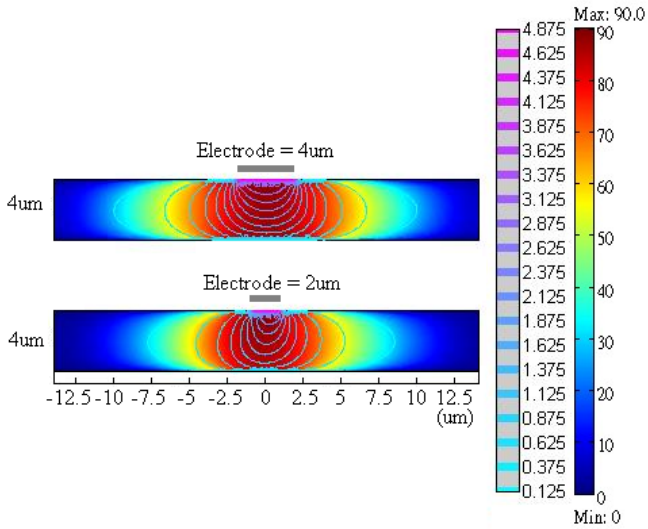

Figure 2-6. The simulation results revealing the influence of the separation of in-plane electrodes on LC alignment.

Example 4

In this example, the Berreman matrix method is used to calculate the optical transmittance of a LC cell, which has both a homeotropic and hybrid alignment zones inside. The parameters of the LC used are presented in Table 2-1. The transmittance of LC between cross polarizers is calculated. The wavelength of the light source is $632.8nm$. The simulation result is shown in Figure 2-7. The homeotropic area has a higher transmittance than hybrid area. This example illustrates the transmittance result of the LC molecules under different alignment and the Berreman matrix method is a useful tool to analysis the LC devices.

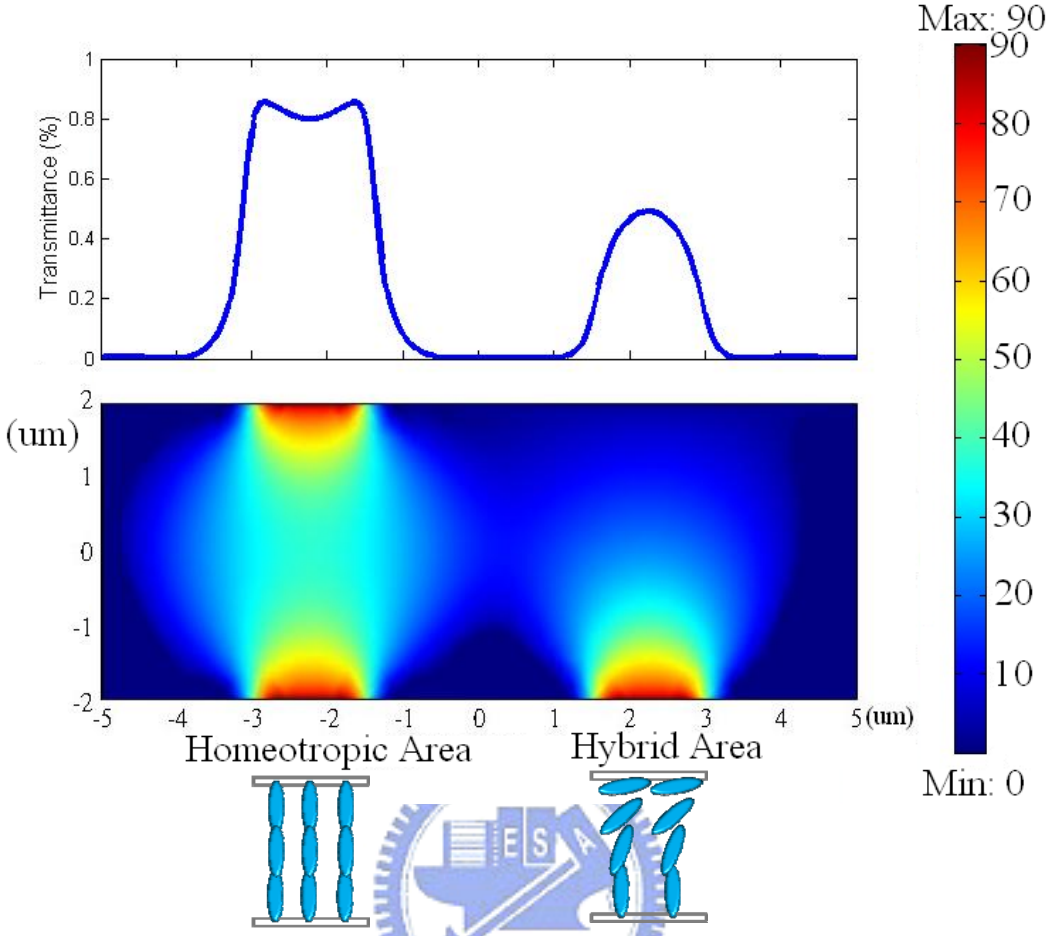

Figure 2-7. The calculated optical transmittance of a LC cell, which has both a homeotropic and hybrid alignment zones inside, and the pretilt angle distribution are plotted.

In summary, simulation technique on the LC director and optical response is developed with Q tensor approach and the Berreman matrix method. We offer some examples to demonstrate the efficacy of the technique. The simulation tools also prove to be extremely useful to help us interpreting the dynamic optical probing data of hybrid alignment LC cells to be reported in Chapter 3.

Chapter 3

Simulation and Dynamic Optical Probing for Hybrid Alignment Liquid Crystal Cells

3.1 Introduction

Liquid crystal has been widely used as flat panel displays in a variety of information system. Conventional TN-mode LCDs are slow response and have a viewing angle problem, are therefore not suitable for displaying high quality video pictures. Recently, π-cells or LC cells in an optically compensated bend mode (OCB-mode) have been successfully developed to offer wider viewing angle and fast speed [13]. Figure 3-1(a) shows the typical structure of an OCB cell with parallelly rubbed alignment surfaces, which render the LC configuration in splay alignment at zero applied voltage. When an applied voltage is raised, the OCB cell tends to make a transition from the splay configuration to the bend-1 state (see Figure 3-1(b)). Figure 3-1(c) depicts the LC configuration in the bend-2 state as the applied voltage is further increased to a higher level. When the voltage is removed, the cell makes a configurational transition from the bend-2 state to the bend-1 state. After in the bend-1 state, the cell does not return to the splay state. A twist configuration may be

generated during the bend-1 to the splay state transition. The typical operation mode of an OCB cell is transition between the bend-1 state and the bend-2 state, which makes OCB attractive for its fast switching characteristics [14].

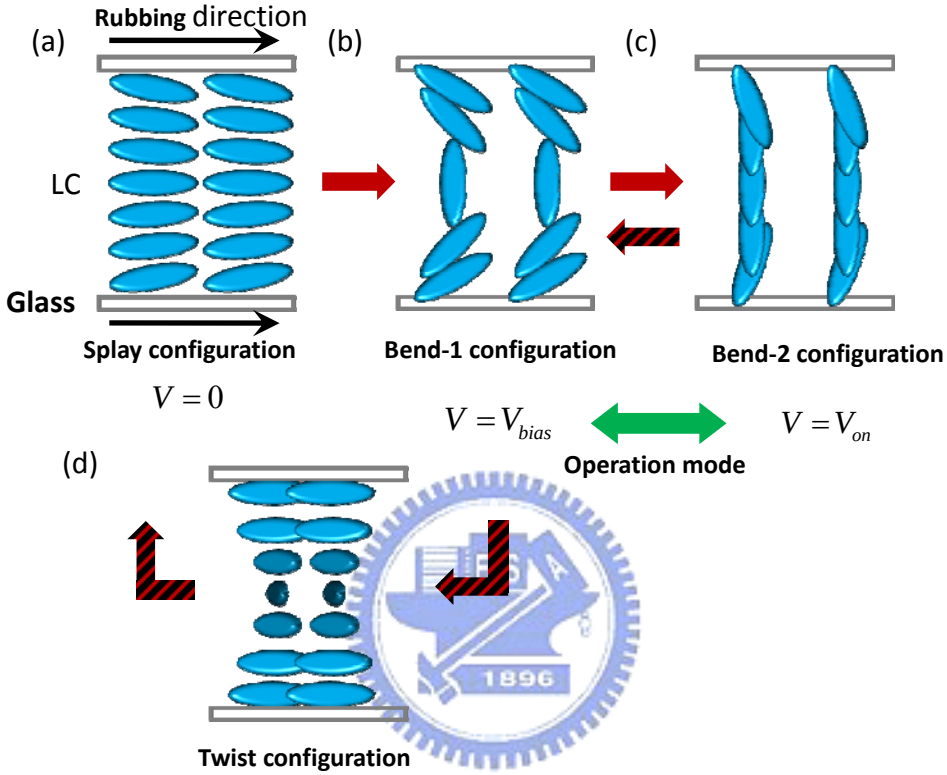

Figure 3-1. The geometric transition of the OCB cell as applied voltage. (a) Splay configuration. (b) Bend 1 configuration. (c) Bend 2 configuration. (d) Twist configuration.

3.2 The Modification of The Existing OCB Cell

A major problem with a typical OCB cell is the need to convert the device from the splay configuration to the bend-1 configuration before use. Based on our observation on an OCB with $4\mu m$ cell gap at 5V, it needs about 40~60 seconds to

complete the transition. The warm-up period is needed because a transition from two topologically distinct configurations (such as from the splay configuration to the bend-1 configuration) takes time to complete and the transition is discontinuous [15, 16]. Another issue in an OCB cell is its poor contrast ratio. In the switching operation between the bend-1 to the bend-2 configuration, the contrast ratio of optical transmittance between the two states is low. The finite warm-up time and low contrast ratio of an OCB cell are becoming the major issues, which are often coupled together. If the operation begins at the splay configuration, higher contrast ratio can be yielded. However, the discontinuous transition between the splay state and the bend-1 state causes another difficulty for application. The transitional discontinuity with an applied electric field may be caused by several meta-states occurring between the splay and the bend-1 state. If we can apply a vertical force on LC molecules in an OCB cell before the electric field is applied, the transition time or warm up time might be reduced. The motivation is to design an OCB structure that can eliminate these drawbacks while keeps the fast switching characteristics. As shown Figure 3-2, we implemented a periodic hybrid alignment zones in an OCB cell in order to produce the effects that we hope for.

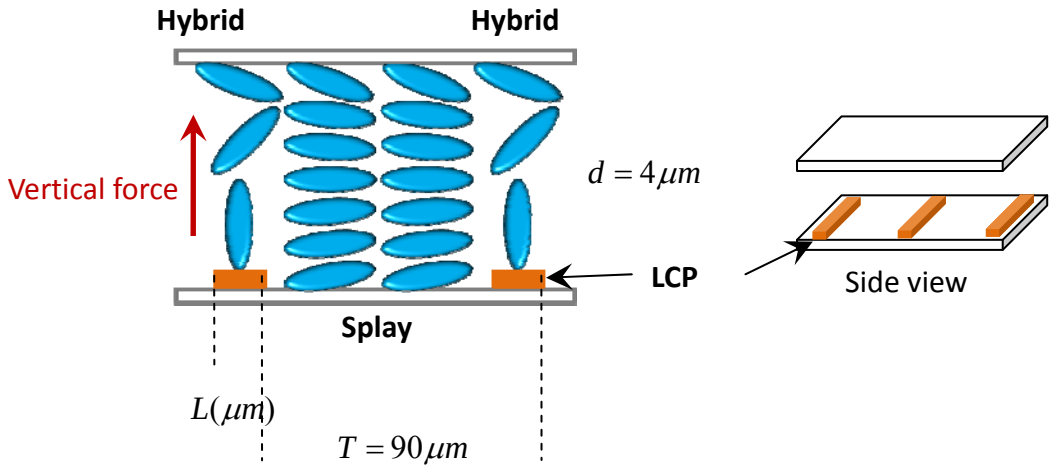

Figure 3-2 The schematic and the side view of our modified OCB cell.

3.3 Experimental Setup of the Dynamic Optical Probing Apparatus

We prepared LC alignment layers on ITO glass substrates with parallel rubbing to yield a LC pretilt angle of 6°. Then we deposited a thin layer of liquid crystal polymer (LCP) on one of the substrates via spin coating and patterned the resulting LCP to make LC molecules nearly vertically aligned at an angle of 85° to the surface. The line pattern of LCP has a period of $90\mu m$. The line-width of LCP stripes is designed to be either $2\mu m$ or $4\mu m$ to yield two different alignment patterns. The cells with $4\mu m$ cell gap are filled with nematic LC 5128 from Chisso. The material characteristics are presented in Table 3-1.

Table 3-1: The LC cell and material parameters used in this experiment.

K_{11}	11.3pN	γ	213 mPaS
K_{22}	7.7pN	$\varepsilon_{\parallel}$	14.1
K_{33}	15.8pN	$\varepsilon_{\perp}$	4.0
n_e	1.675	D (cell gap)	$4\mu m$
n_o	1.506	LC pretilt angle on surface	6°

Figure 3-3 (a) shows the schematic of the measurement setup. An **E**lectron **M**ultiplying **CCD** (**EMCCD**) is used to acquire the image of an inverted optical microscope. EMCCD provides the benefits of fine temporal resolution and high sensitivity, which is crucial for our dynamic optical probing study. EMCCD can rapidly take an image exposure, however, the frame read out speed is limited to below $34ms$. Since the dynamic optical probing event for LC is repeatable, we use a pump-probe scheme to retrieve the dynamic response of the OCB cell by using a delay generator to trigger the EMCCD and the LC sample repeatedly. The sample is driven by a pulse whose duration is $4ms$ and pulse period is $75ms$. The waveform is shown in Figure 3-3 (b). The EMCCD exposure time is set for $0.5ms$. After a multiple of exposure with a delay time t, a time-resolved dynamic image of the LC sample is acquired. By varying the delay time *t*, a series of dynamic images can be acquired.

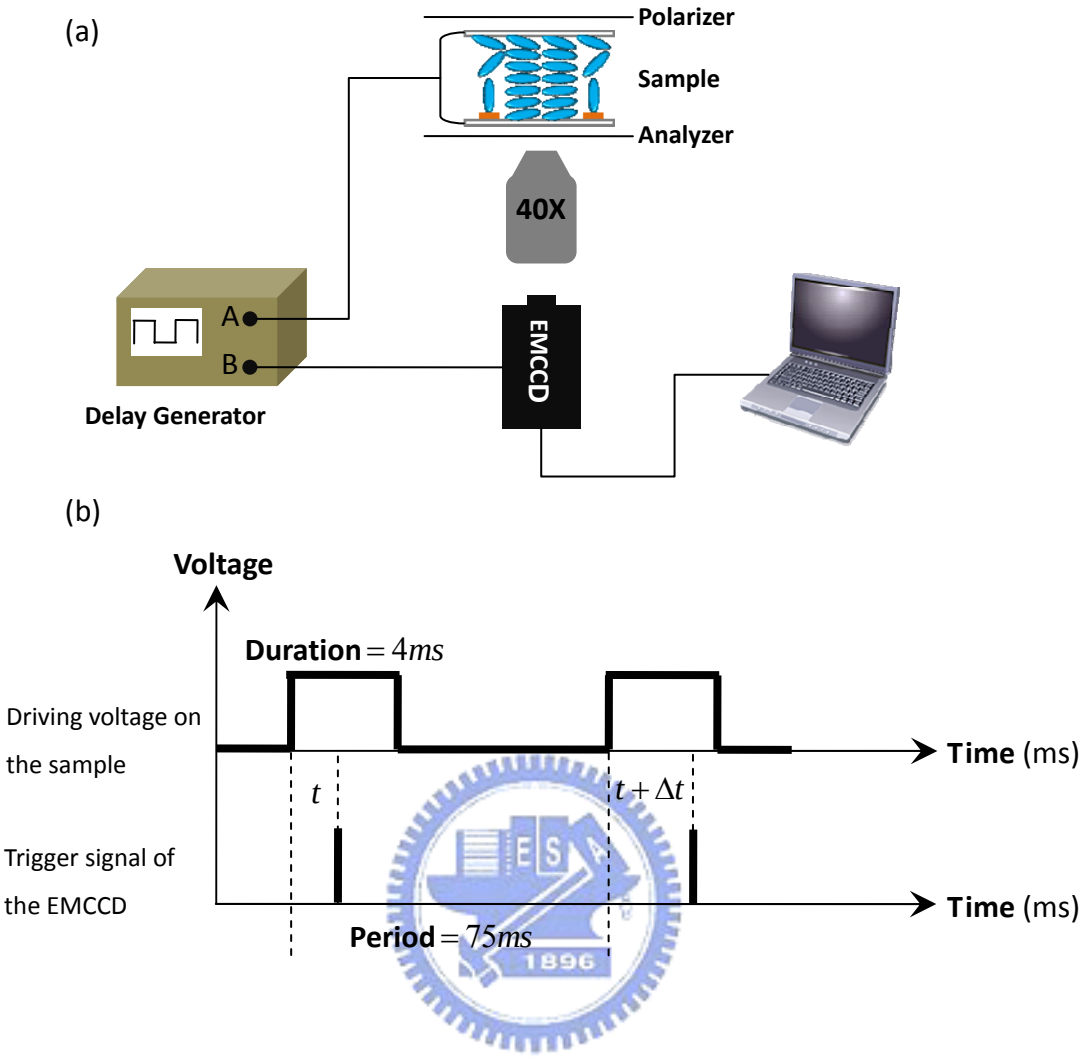

Figure 3-3 (a) The setup of dynamic optical probing comprising of a delay generator to control the time delay. (b) The waveform and the trigger signal applied on the sample and the EMCCD.

3.4 Results and Discussion

Figure 3-4 shows the on and off response curves of the LC cells measured with crossed polarizers. Four different LC cells of homogeneous OCB, homogeneous hybrid cell, and $2\mu m$ - and $4\mu m$ -line patterned hybrid OCB cells. The homogeneous

OCB cell is measured after being warming up for about 40-60 seconds with 5 volts. The other LC cells are measured without warm up process. We notice that the off times of both line-patterned hybrid cells are about the same as that of the homogeneous hybrid cell. From Figure 3-4, by including a line pattern in a hybrid LC cell, we found that the optical transmittance in the dark state can be improved, whereas the bright state is degraded. Figure 3-5 exhibits the behaviors of the optical transmittances of the LC cells after the voltage on the cells is removed. It shows that the twist motion in the OCB cell during the transition between the bend and the splay configuration takes 200 seconds but the other cells do not show such a characteristic.

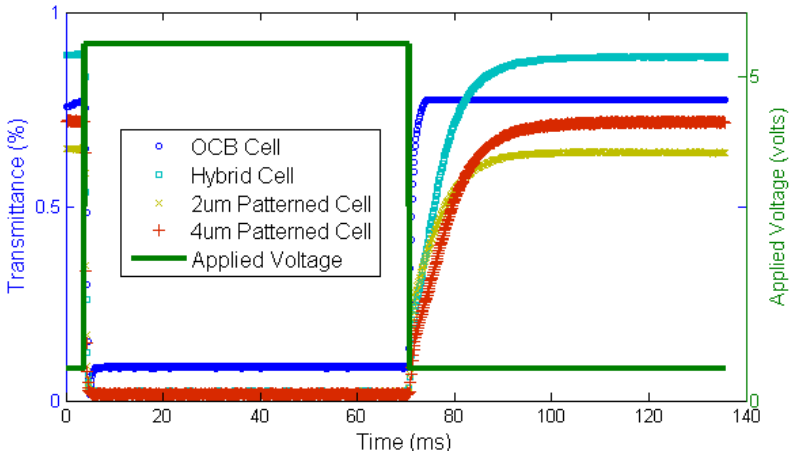

Figure 3-4 Optical response curves of four different LC cells (homogeneous OCB, homogeneous hybrid, and $2\mu m$ - and $4\mu m$ -line patterned hybrid OCB cells.

Table 3-2: The response times of each cells are given.

Types of LC cells	ON (ms)	OFF (ms)
OCB	1.45	4.68
Hybrid	1.15	32.69
$2\mu m$ pattern	1.09	33.37
$4\mu m$ pattern	1.12	35.3

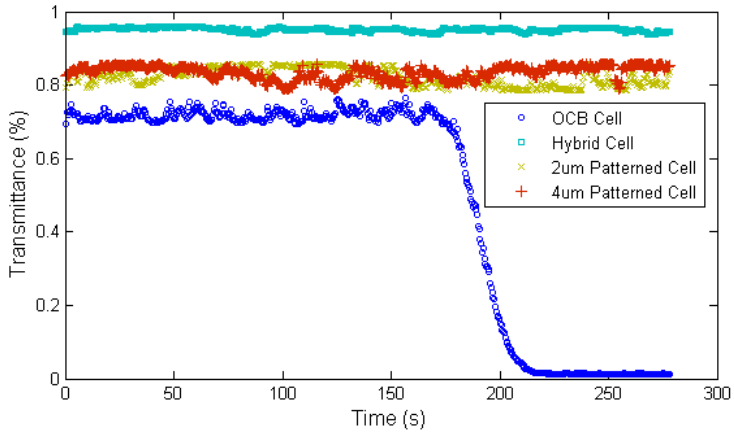

Figure 3-5 The optical transmittance is measured after the applied voltage is removed. The measurement results reveal the LC twist motion in each cells.

For detailed analysis, we use the apparatus described in the section 3.3 to probe the $2\mu m$- and $4\mu m$-line patterned hybrid OCB cells. The optical images of the line-patterned cells are given in Figure 3-6. The separation distance between two neighboring lines is $90\mu m$, corresponding to 222 pixels in the image. We use this

calibration to calculate the line width of the LC cells. The $2\mu m$-line patterned cell looks like a homogeneous cell while the observed linewidth for the $4\mu m$-line patterned cell is about $1.62\mu m$.

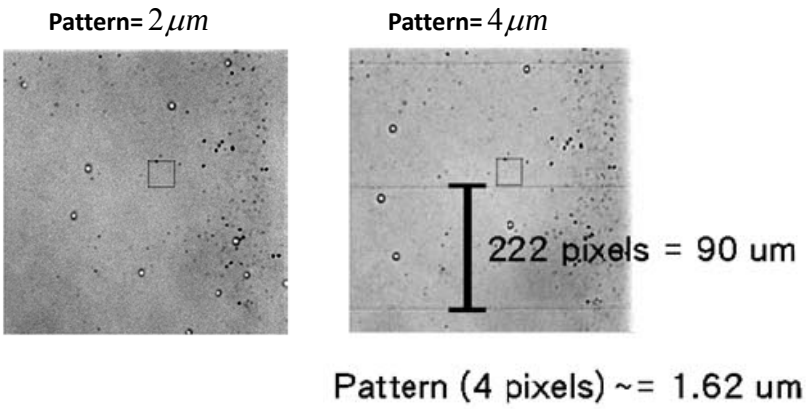

Figure 3-6 The optical micrographic images of the line-patterned hybrid cells. The resolution of the microscope is about $0.3\mu m$.

Figure 3-7 (a) shows the optical transmittance images of the two line-patterned LC cells in a region covering one period ($90\mu m$). The images were taken with crossed polarizer and analyzer. The $4\mu m$-line patterned cell exhibits a clear stripe whereas the $2\mu m$-line patterned cell is somewhat like homogeneous. Figure 3-7 (b) shows the measured image and the simulated optical transmittance distribution of the $4\mu m$-line patterned cell. For a quantitative comparison, the gray-level line profile taken by cutting through the images horizontally at the middle of the line stripe. Both of the simulation and the measured line profiles reveal two dark stripes locating at the

positions of pixel number 30 and 70, respectively.

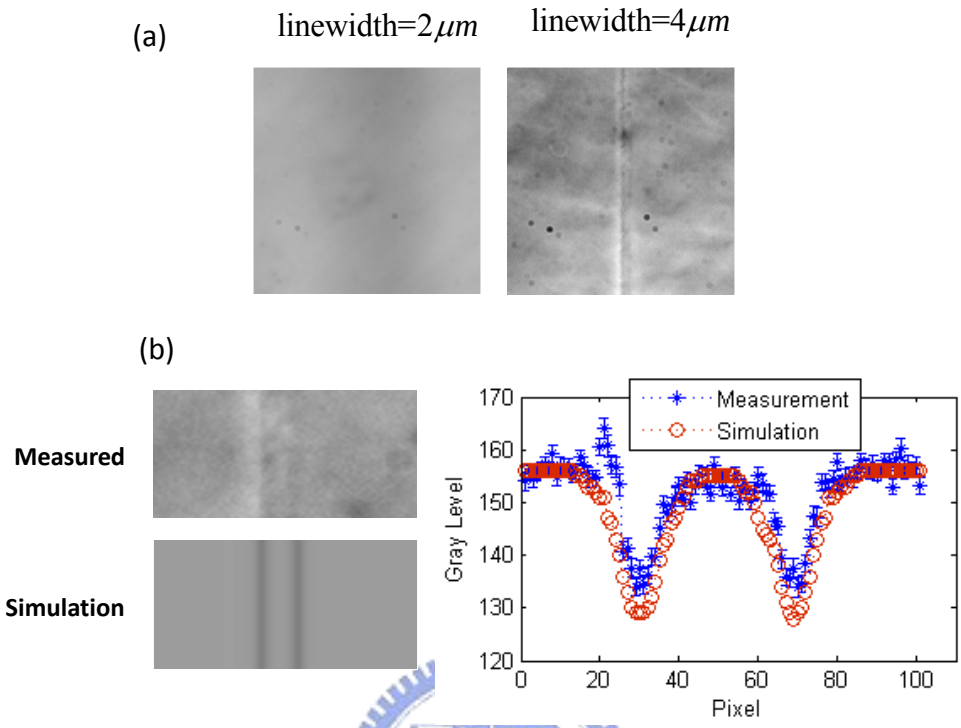

Figure 3-7. (a) The measured and calculated optical transmittance images of two line-patterned LC hybrid alignment cells in a region covering one period ($90\mu m$). (b) The measured and the simulated optical transmittance images of the $4\mu m$-line patterned cell and the gray level profiles horizontally cut through the images at the center of the vertical position.

The dynamic optical probing results of the cells are summarized in Table 3-3 at different delay times. Each image shows the optical transmittance with crossed polarizers over an area covering one period ($90\mu m$) of the line-patterned cells. The direction of the line stripes is marked with the red arrow. We can see that during the

field-on period from $0ms$ to $4ms$, the $4\mu m$-line patterned cell is darker than the $2\mu m$-line patterned cell. After turning off the voltage, the LC molecules relax to the original configuration. The $4\mu m$-line patterned cell becomes brighter than the $2\mu m$-line patterned cell at the delay time of $75ms$. With our optical apparatus, the brightest and darkest gray levels are 120 and 9, respectively, in an 8-bits TIFF image format. We sum the gray-level values over a region covering one period. The summed gray-level value as a function of delay time is presented in Figure 3-8. The response times of the two line-patterned cells have values of $1ms$ and $30ms$ for the on and the off times, respectively, affirming the observation shown in Table 3-2. Within the field-on duration from $0ms$ to $4ms$, the $4\mu m$-line patterned cell reaches the darkest gray level faster than the $2\mu m$-line patterned cell does.

Table 3-3: The optical images of the two line-patterned cells at different delay times.

Delay time	0 (ms)	0.5 (ms)	1 (ms)	1.5 (ms)
$2\mu m$				
$4\mu m$				
Delay time	2 (ms)	2.5 (ms)	3 (ms)	15 (ms)

$2\mu m$				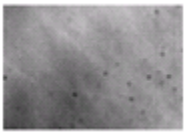
$4\mu m$				
Delay time	20 (ms)	25 (ms)	30 (ms)	75 (ms)
$2\mu m$	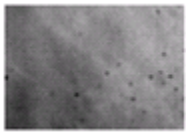	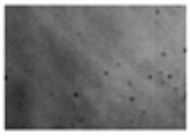	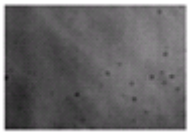	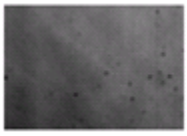
$4\mu m$	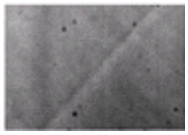	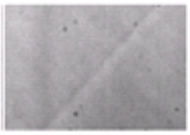	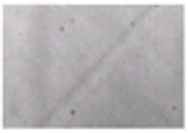	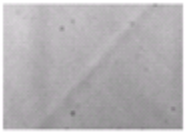

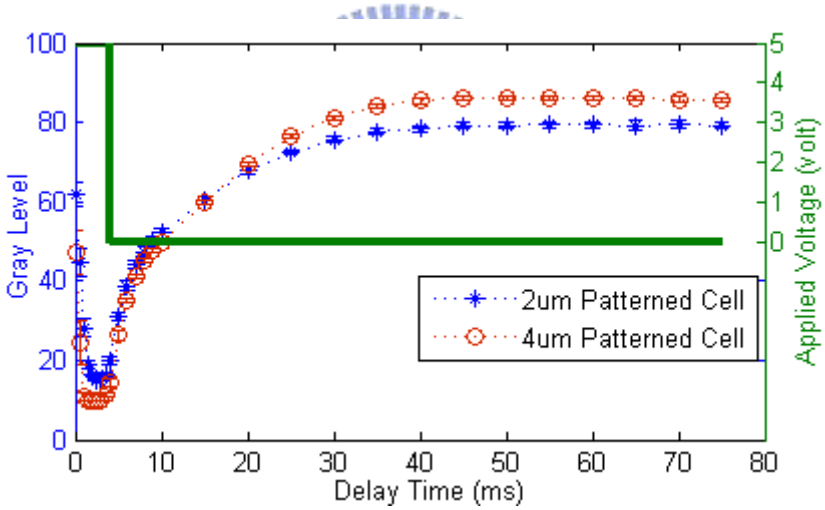

Figure 3-8. The summed gray-level value over a region covering one period in each image of Table 3-3 is plotted as a function of delay time.

We analyze the LC configuration above the LCP line stripe and above the region between the neighboring LCP lines. Note that the LC molecules above the LCP line stripe are in hybrid alignment configuration (**Hybrid**) while LC molecules form a

typical OCB splay configuration (**OCB**) above the region without LCP. Figure 3-9 presents the optical transmittance of the $2\mu m$ and $4\mu m$-line patterned cells measured under crossed polarizers. The summed gray-level values over the region with hybrid alignment configuration (Hybrid) and over the region with OCB splay configuration (Splay) are plotted as a function of delay time. The result shows that the response curves in the Hybrid and the OCB regions are almost identical and indistinguishable.

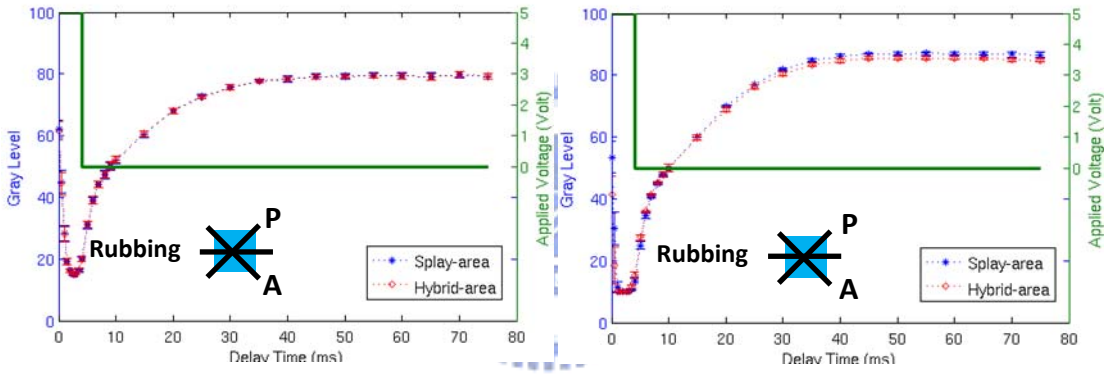

(a) The $2\mu m$ patterned cell **(b) The $4\mu m$ patterned cell**

Figure 3-9. The optical transmittance (in terms of gray-level) of the $2\mu m$ and $4\mu m$-line patterned cells was measured under a crossed polarizer-analyzer. The summed gray-level values over the region with hybrid alignment configuration (Hybrid) and over the region with OCB splay configuration (Splay) are plotted as a function of delay time.

Based on the result of OCB cell described in the section 3.1, we found that a LC

twist motion can occur as the OCB cell makes a transition from the bend to the splay configuration by removing the applied voltage. Therefore, to probe into the line-patterned cells we specifically arrange the directions of polarizer and analyzer to allow us observing the LC twist motion. This can be achieved by aligning the direction of the polarizer with the rubbing direction of the cell and then let the analyzer to cross with the polarizer. Figure 3-10 shows the measurement results. By using the simulation tool developed with the elastic free energy density of Eq. 1-3, two LC configurations with minimum free energy can be found: (1) the LC pretilt can be at any tilt angle without twist, or (2) the LC pretilt is fixed at 0° while with a twist angle of 0°, 90° or 180°. From our previous study on splay configuration, there exists a 180° twist motion in the cell when the LC molecules are allowed to relax as depicted in Figure 3-1. We further use the simulation tool described in section 2.2 to calculate the optical response of a twist cell with a twist angle varying from 0° to 180°. In Figure 3-11, we present the results for two LC cells with different cell gap. For the LC cell with $10\mu m$ cell gap, the LC configuration with 180° twist angle cannot yield any gray-level change. But for the LC cell with a $4\mu m$ cell gap the gray-level can be changed by 60 and can be easily measured. However, no gray-level change was detectable for the LC cell with a $4\mu m$ cell gap. Thus, we conclude that no twist motion occurs during the relaxation after removing the applied field.

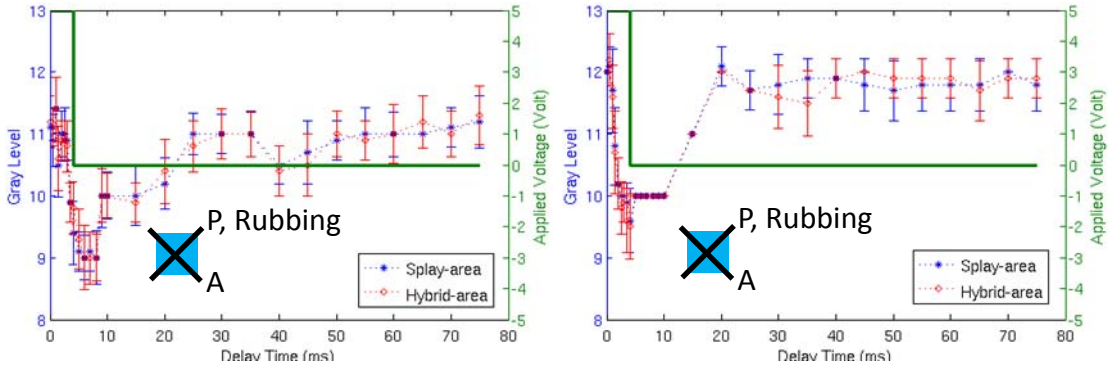

(a) The $2\mu m$ patterned cell (b) The $4\mu m$ patterned cell

Figure 3-10. The measured optical transmittance (in terms of gray-level) of the $2\mu m$ and $4\mu m$-line patterned cells is plotted as a function of delay time. The direction of the polarizer is aligned with the rubbing direction and the analyzer is set to cross with the polarizer.

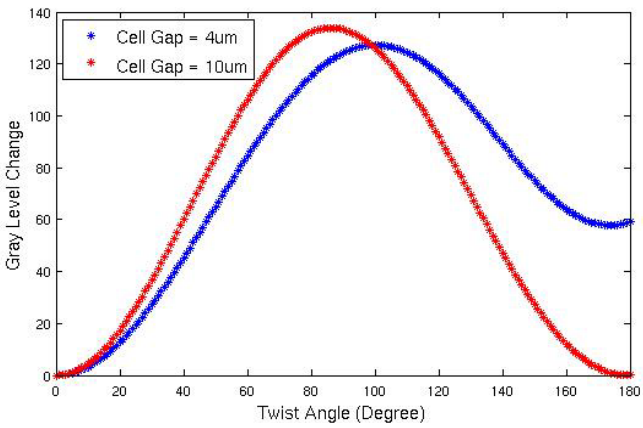

Figure 3-11. The calculated optical transmittance variation (in terms of gray-level change) of a TN cell with a twist angle varying from 0° to 180°. Two TN cells with cell gaps 4 and 10 μm were used for the simulation.

Because no twist motion occurs during the relaxation inside the line-patterned

cells, we can employ a two-dimensional model to simulate the device structure and compare with the measurement results. The device and LC material parameters used are shown in Table 3-1. Figure 3-12 gives the plots of the director profile and optical transmittance of the simulation on the $4\mu m$ line-patterned cell at relaxation time of $5ms$, $15ms$, $25ms$ and $75ms$. There are ripples in the optical transmittance curve can be observed, which could be due to some defect areas caused by the finite elements method.

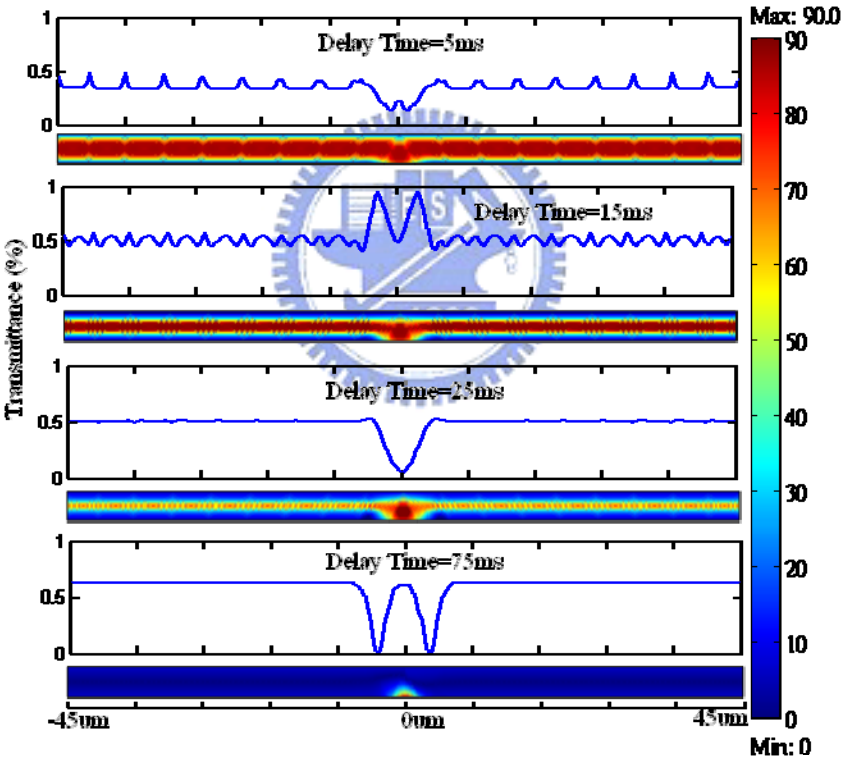

Figure 3-12. The calculated director profile and optical transmittance of the $4\mu m$ line-patterned cell at delay time of $5ms$, $15ms$, $25ms$ and $75ms$.

As shown in Figure 3-10, the gray-level steady value of the on-state is about 2 or

3 higher than the darkest level (~9) of our apparatus. The slightly higher brightness in the dark state may originate from that LC molecules are misaligned or misaligned rubbing direction and polarizer. The observed higher gray-level by 3 indicates the angular deviation must be less than 1.82° in the $4\mu m$ line-patterned cell. We therefore set the direction of the polarizer to deviate from the rubbing direction by 1.82° in our simulation (Fig. 3.10 (b)). Based on the calibration, we can make a direct comparison between the measured data and the simulation. The measured and simulated optical transmittance (in terms of gray-level) as a function of delay time are plotted in Figure 3-13. As shown, the simulation result agrees well with the measured data of the $4\mu m$ line-patterned cell. For the $2\mu m$ line-patterned cell, since we cannot observe the LCP lines in Figure 3-6, so the simulation result cannot be used to compare with the measured data.

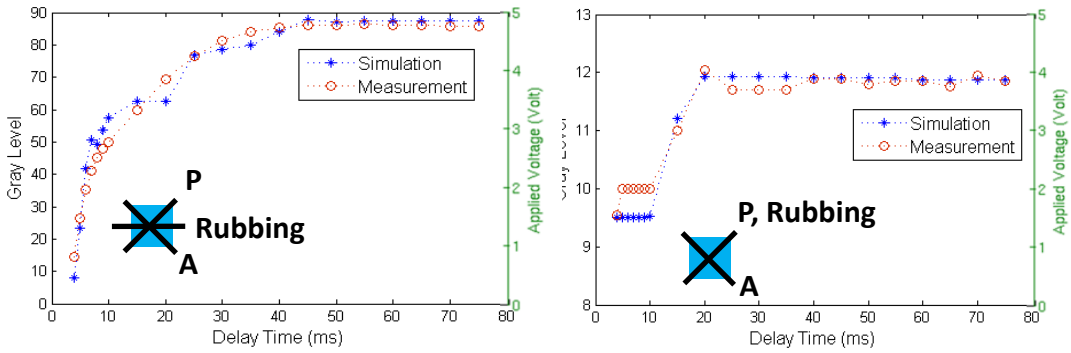

Figure 3-13. The measured and simulated optical transmittance variation (in terms of gray-level change) is plotted as a function of delay time. The $4\mu m$ line-patterned cell was inserted between a cross polarizer-analyzer with (a) the

direction of the polarizer aligning to the rubbing direction, (b) the direction of the polarizer deviating from the rubbing direction by 1.82°**.**

In summary, by including a periodic LCP line pattern in an OCB cell, we show that the resulting hybrid OCB cell can eliminate the need of warm up. The zones of hybrid LC configuration also prevent LC twist motion during the transition from the bend to the splay configuration after the voltage is removed. However, the hybrid LC configuration above the LCP lines also significantly influences the LC relaxation and makes the cells relax slowly.

This work is supported by Taiwan TFT LCD Association (TTLA) and useful discussions with the members of the group are acknowledged.

Chapter 4

Inverse Problem of Liquid Crystal Director Profile

In Chapter 3, a model extraction technique has been implemented by comparing the model simulation result with the measured data to retrieve the model parameters. However, in the case of LC, the direct retrieval of a LC director profile from the measured data is difficult to check its accuracy and reliability. Recently, C. J. P. Newton in Hewlett-Packard Laboratories investigated the possibility of inverse problem to retrieve the LC director profile with singular value decomposition scheme [17]. Although it is inspiring, the work is limited to the stability and converging properties of inverse problem technique developed. No practical applications on the LC director profile retrieval from experimentally measured data were reported. In this chapter, we go one further step by deriving the necessary equations and detailed steps to successfully achieve the target of the LC director profile retrieval from the measured data.

4.1 Introduction to the Inverse Problem

The relation between the inverse problem and the forward problem can be understood as follows: In Eq. 4.1, a model of a physical system is described by a matrix $\mathbf{A}$ and a state vector $\mathbf{x}$ depicts the system status. Then the forward problem is that we can predict the system response $\mathbf{b}$ with Eq. 4.1

$$\mathbf{Ax} = \mathbf{b}. \tag{4.1}$$

The inverse problem can then be easily understood as follows: Based on the measured system response vector $\mathbf{b}$ and the model matrix $\mathbf{A}$, we can retrieve the parameters of the physical system $\mathbf{x}$.

$$\mathbf{x} = \mathbf{A}^{-1}\mathbf{b}. \tag{4.2}$$

In the past, inverse problems are usually treated as a data fitting procedure with forward problem. This can be done by varying the state vector $\mathbf{x}$ to obtain the best fit. However, some problems are not suitable for data fitting because either it may be difficult to fit the response data to a model or the best fit could yield a spurious solution. Hadamard introduced some useful criteria to categorize the problems: [18]

Criterion 1: *For all admissible data, a solution exists.*

Criterion 2: *For all admissible data, the solution is unique.*

Criterion 3: *The solution depends continuously on the data.*

A problem that violates any of the three criteria is called ill-posed. The third criterion is actually the stability condition, which requires that a small perturbation to the input

does not produce a large change in the output. When a problem is ill-posed, it is not easy to determine the true solution objectively. We will start from a simple mathematical problem to illustrate the difficulties of an inverse problem.

Assuming that the model matrix $\mathbf{A}$ and the input vector $\mathbf{x}$ are:

$$\mathbf{A} = \begin{bmatrix} 1 & \frac{1}{2} & \frac{1}{3} & \frac{1}{4} \\ \frac{1}{2} & \frac{1}{3} & \frac{1}{4} & \frac{1}{5} \\ \frac{1}{3} & \frac{1}{4} & \frac{1}{5} & \frac{1}{6} \\ \frac{1}{4} & \frac{1}{5} & \frac{1}{6} & \frac{1}{7} \end{bmatrix}, \qquad \mathbf{x} = \begin{bmatrix} 1 \\ 1 \\ 1 \\ 1 \end{bmatrix}. \tag{4.3}$$

It is clear that for any given $\mathbf{x}$, we can obtain a unique $\mathbf{b}$. By evaluating $\mathbf{b}$ to the four-digit accuracy,

$$\mathbf{b} = \mathrm{A} \cdot \mathrm{x} = \begin{bmatrix} 1 & \frac{1}{2} & \frac{1}{3} & \frac{1}{4} \\ \frac{1}{2} & \frac{1}{3} & \frac{1}{4} & \frac{1}{5} \\ \frac{1}{3} & \frac{1}{4} & \frac{1}{5} & \frac{1}{6} \\ \frac{1}{4} & \frac{1}{5} & \frac{1}{6} & \frac{1}{7} \end{bmatrix} \begin{bmatrix} 1 \\ 1 \\ 1 \\ 1 \end{bmatrix} = \begin{bmatrix} 2.0833 \\ 1.2833 \\ 0.95 \\ 0.7595 \end{bmatrix}. \tag{4.4}$$

Therefore, the first two Hadamard criteria are satisfied. To analyze the stability criterion, we add noise to $\mathbf{x}$ with a noise level around 0.1 percent of $\mathbf{x}$. We then introduce the following parameters to reveal the instability of a problem with *S*:

$$s_{in} = \frac{|\mathbf{x}' - \mathbf{x}|}{|\mathbf{x}|},$$

$$s_{out} = \frac{|\mathbf{b}' - \mathbf{b}|}{|\mathbf{b}|}, \text{ where } |\mathbf{x}| = \sqrt{(\sum_i x_i^2)}, \text{ and} \tag{4.5}$$

$$S \equiv \frac{s_{out}}{s_{in}}.$$

We apply Eq. 4.5 to calculate S by adding 10,000 different random noise to $\mathbf{x}$ and present the distribution of S in Figure 4-1(a). We can find that most of the values fall between 0 and 1.1, which indicates that a small the perturbation to $\mathbf{x}$ does not generate a large variation in **b**. Thus a stable solution can be obtained for this problem.

For the inverse problem, we repeat the calculation by adding small noise to $\mathbf{b}$ and estimate the variation of $\mathbf{x}$ and the resulting instability parameter S is plotted in Figure 4-1(b). By comparing Figure 4-1(b) to Figure 4-1(a), it is clear to find that the instability parameter S of the inverse problem is 10 thousand times larger than that of the forward problem. Therefore, the inverse problem fails to satisfy Hadamard's third criterion of stability and is ill-posed in nature.

(a) (b)

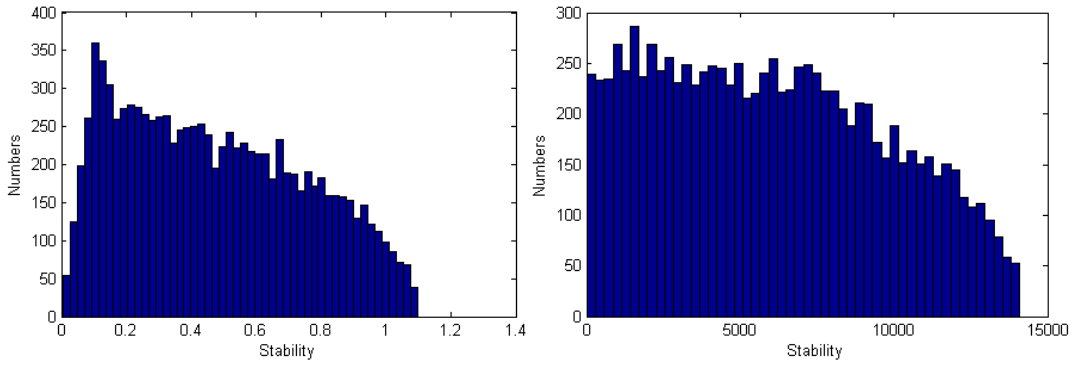

Figure 4-1. (a) The Stability distribution of $\mathbf{x}$. (b) The Stability distribution of $\mathbf{b}$.

By looking further into $\mathbf{Ax} = \mathbf{b}$, in a general case with $\mathbf{A} \in \mathbf{R}^{M \times N}$, $\mathbf{x} \in \mathbf{R}^{N}$, and $\mathbf{b} \in \mathbf{R}^{M}$. To find a solution **x**, we can encounter the following three situations:

(1) If $M = N$, we encounter a linear system of N variables with N equations. If $\mathbf{A}$ is nonsingular with $\det(\mathbf{A}) \neq 0$, the system possesses a unique solution. On the other hand if $\mathbf{A}$ is singular (*i.e.*, $\det(\mathbf{A}) = 0$), the system has infinitely many solutions.

(2) If $M < N$, we have a linear system with less equations than variables, which is called under-determined. This problem can be reduced to the situation (1) by expanding matrix $\mathbf{A}$ and matrix $\mathbf{b}$ with $N - M$ rows of zero, respectively.

(3) If $M > N$, we have a linear system with more equations than variables, which is called over-determined and ill-posed. However, we can find the least-squares solution

of $\mathbf{Ax} = \mathbf{b}$ by finding a vector $\mathbf{x}$ in R^n that minimizes $\|A\mathbf{x} - \mathbf{b}\|$.

Let us return to our simple problem. Since the problem is ill-posed, any matrix inversion algorithm will fail to find the desired solution $\mathbf{x}$. Therefore, specialized technique must be invoked to solve the inverse problem. One of the successful approaches is the so-called *regularization* [19]. We will briefly describe the idea of the regularization scheme, known as Tikhonov regularization. As noted above, we can find the least-squares solution of $\mathbf{Ax} = \mathbf{b}$ by finding a vector $\mathbf{x}$ in R^n that minimizes $\|A\mathbf{x} - \mathbf{b}\|^2$ [20]. The key issue is how to choose the sensible solution from the space of reasonable solutions. An idea is to reduce the size of the solution space by invoking additional constraints. We can implement this idea by adding an additional term to $\|A\mathbf{x} - \mathbf{b}\|^2$ with a carefully selected regularization parameter λ

$$\mathbf{x} = \min_{\mathbf{x}} \left\{ \|\mathbf{Ax} - \mathbf{b}\|^2 + \|\lambda \mathbf{Ix}\|^2 \right\}. \tag{4.6}$$

A graphical tool, which is termed as the *L-curve*, can be used to help us choosing the regularization parameter. The *L-curve* graphical technique plots the $\|\lambda \mathbf{Ix}\|^2$ on the y-axis and the $\|\mathbf{Ax} - \mathbf{b}\|^2$ on the x-axis by varying λ. Figure 4-2 exhibits the *L-curve* for our illustrative example, which explains the name of the *L-curve* to be due to the shape of the plot. The optimal value of λ is at the corner of the curve. By using this value, we can find the solution $\mathbf{x} = [1.0163 \quad 0.9188 \quad 1.0481 \quad 1.0429]^T$, which is very close to the known state vector $\mathbf{x}$ given in Eq. 4.3.

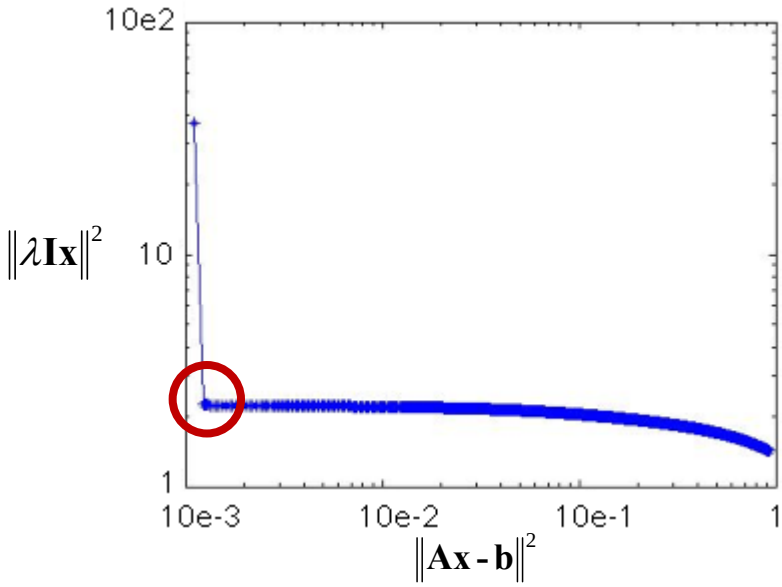

Figure 4-2. The *L-curve* is a curve in a log-log scale with $\|\lambda \mathbf{Ix}\|^2$ on the y-axis and $\|\mathbf{Ax}-\mathbf{b}\|^2$ on the x-axis by varying λ from 10^{-5} to 1. The optimal value of λ is be chosen is at the corner of the curve labeled with the red circle.

4.2 The Inverse Problem of Liquid Crystal Director Profile

Inverse problem has been widely used in medical diagnostic imaging, such as magnetic resonance imaging (MRI) and computed tomography (CT). The goal is to non-invasively diagnose the internal structure of a patient's body. The two medical imaging methods are accomplished by measuring the scattered field at various incident angles and then solving the inverse problem to yield the cross section image of the patient's body.

In the case of LC, we want to know the director profile in a LC cell. This goal is the same as MRI and CT. So we refer to the CT concept and convert it for LC. The

scheme implemented to collect the data with various incident angles of light is illustrated in Figure 4-3.

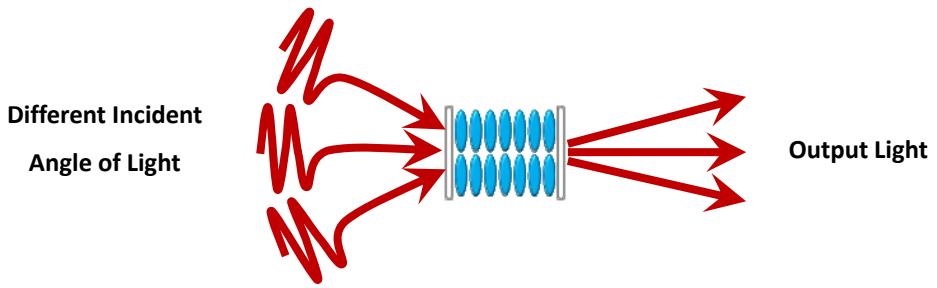

Figure 4-3. The schematic showing the setup implemented to collect the data with various incident angles of light.

The forward problem in the case of LC is that a LC director profile $\boldsymbol{\theta}(z)$, which is generated from a simulation, is first converted to the dielectric-constant profile $\boldsymbol{\varepsilon}(z)$ and then calculate the resulting optical transmittance via the Berreman matrix method (see Eq. (2.40)). The output light relates to the dielectric-constant profile as shown in Eq. (4.7) or Eq. (2.55).

$$\boldsymbol{\Psi}_{\text{output}} = \mathbf{B}\left(\boldsymbol{\varepsilon}\left(\boldsymbol{\theta}\right)\right)\boldsymbol{\Psi}_{\text{in}}. \tag{4.7}$$

By applying the inverse problem technique to LC [13], the HP group used singular value decomposition (SVD) to retrieve the dielectric-constant profile from the simulated data. We note that the dielectric constant of a uniaxial film is described by a symmetric 3×3 matix, which has 6 independent matrix elements. But its corresponding optical axis, which is the pretilt angle of LC, can be described by only

two components. If we set up an inverse problem to retrieve the dielectric-constant profile from the measured optical data, we have to solve the inverse problem with 6 unknown variables. The 6 variables leads to a higher level of noise than the less variables. To avoid the drawback, we develop a new formalism of inverse problem, which goes directly from the optical fields to the pretilt profile. Figure 4-4(a) shows the difference between our new approach and the HP group's method.

The inverse problem is ill-posed, so that in lack of a priori information it is difficult to find a solution. Fortunately, we have some priori information about the initial director profile $\boldsymbol{\theta}_0(z)$ from the surface condition and the simulation result. We also have the measured transmittance of output light. We can rewrite Eq. (4.7) as:

$$\boldsymbol{\Psi}_{\text{output}} = \mathbf{B}(\boldsymbol{\theta}_0)\boldsymbol{\Psi}_{\text{in}} + \delta\boldsymbol{\Psi}, \tag{4.8}$$

where $\delta\boldsymbol{\Psi}$ is the difference of the measured transmittance of output light from simulation. We concentrate on $\delta\boldsymbol{\Psi}$ and derive an equation to show how the director profile change would change $\delta\boldsymbol{\Psi}$. The result is similar to the inverse problem that we search for a $\delta\boldsymbol{\theta}(z)$ to minimize $\delta\boldsymbol{\Psi}$:

$$\delta\boldsymbol{\Psi} = \frac{\partial\mathbf{B}}{\partial\boldsymbol{\theta}} \cdot \delta\boldsymbol{\theta} = \mathbf{J} \cdot \delta\boldsymbol{\theta}, \tag{4.9}$$

where $\mathbf{J}$ is the Jacobian matrix with an element $J_{ij} = \dfrac{\partial B_i}{\partial \theta_j}$.

The flowchart of searching for the LC director profile with optical transmittance data is described in Figure 4-4.

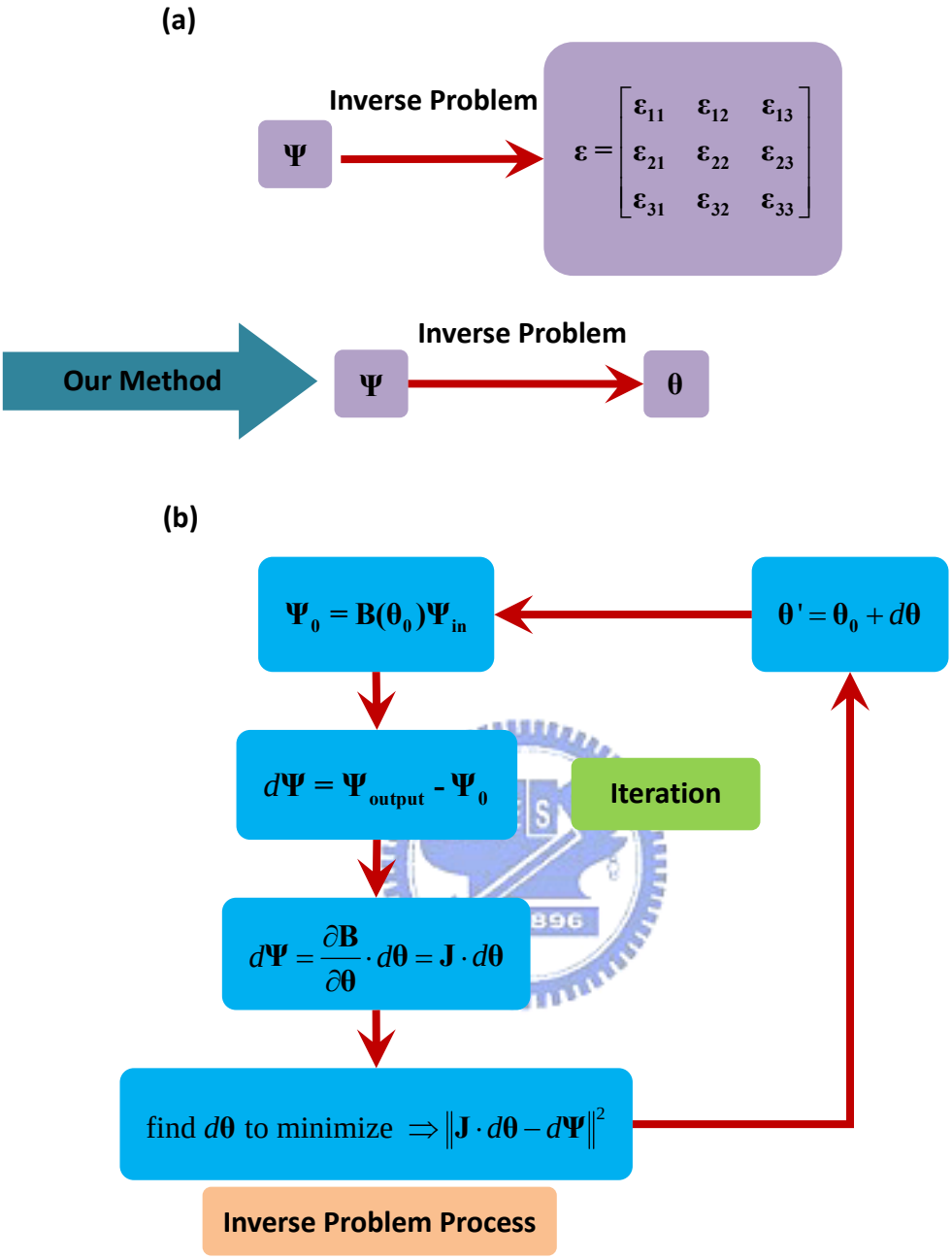

Figure 4-4. (a) Schematic showing the difference between our new approach and the HP group's method. (b) The flowchart of searching for the LC director profile with optical transmittance data.

4.3 Theoretical Details

To reveal the mathematical features of the inverse problem in LC, we begin with the Berreman matrix method and show the details of our method. Eq. (4.10) is an ODE form of wave propagation based on the Berreman matrix formalism with ξ the parameter relating to the incident angle of input light.

$$\left(\frac{d}{dz}+i\omega\mathbf{\Pi}_{\xi}\right)\mathbf{\Psi}_{\xi}=0. \tag{4.10}$$

A perturbation of pretilt angle results in a change of Berreman matrix from $\mathbf{\Pi}$ to $\mathbf{\Pi}+\delta\mathbf{\Pi}$. A change in Berreman matrix further leads to a change in optical field from $\mathbf{\Psi}$ to $\mathbf{\Psi}+\delta\mathbf{\Psi}$. To include the perturbation effect of $\theta(z)$ into Eq. (4.10), we obtain:

$$\left(\frac{d}{dz}+i\omega(\mathbf{\Pi}+\delta\mathbf{\Pi})\right)(\mathbf{\Psi}+\delta\mathbf{\Psi})=0, \tag{4.11}$$

or

$$\left(\frac{d}{dz}+i\omega\mathbf{\Pi}\right)\delta\mathbf{\Psi}=-i\omega\left(\delta\mathbf{\Pi}\,\mathbf{\Psi}+\delta\mathbf{\Pi}\,\delta\mathbf{\Psi}\right), \tag{4.12}$$

where $\left(\frac{d}{dz}+i\omega\mathbf{\Pi}\right)\mathbf{\Psi}=0$ is used. Eq. (4.12) is a differential equation, which can be casted into an operator form

$$L\cdot u=f, \tag{4.13}$$

where $L=\left(\frac{d}{dz}+i\omega\mathbf{\Pi}\right)$, $u=\delta\mathbf{\Psi}$, and $f=-i\omega\left(\delta\mathbf{\Pi}\,\mathbf{\Psi}+\delta\mathbf{\Pi}\,\delta\mathbf{\Psi}\right)$. The solution of Eq. (4.13) is given as

$$u=H\cdot u(0)+G[f], \tag{4.14}$$

where G is the operator notation of Eq. (4.13). By using the initial condition of $u(0)=0$, Eq. (4.12) can be rewritten as

$$\left(\frac{d}{dz}+i\omega\mathbf{\Pi}\right)\delta\mathbf{\Psi}=-i\omega\left(\delta\mathbf{\Pi}\,\mathbf{\Psi}+\delta\mathbf{\Pi}\,\delta\mathbf{\Psi}\right)$$
$$\Rightarrow\left(1+i\omega G\,\delta\mathbf{\Pi}\right)[\delta\mathbf{\Psi}]=-i\omega G[\delta\mathbf{\Pi}\,\mathbf{\Psi}] \tag{4.15}$$
$$\Rightarrow\delta\mathbf{\Psi}=-i\omega G[\delta\mathbf{\Pi}\,\mathbf{\Psi}],$$

where the Neumann series

$$\left(1+i\omega G\delta\mathbf{\Pi}\right)^{-1}=\left(1+\left(-i\omega G\delta\mathbf{\Pi}\right)+\left(-i\omega G\delta\mathbf{\Pi}\right)^{2}+...\right), \tag{4.16}$$

is kept up to the first-order term in view of $\|\omega G\,\delta\mathbf{\Pi}\|<1$. We can convert the Green's function to an integral form and transform Eq. (4.15) into an integral equation

$$\delta\mathbf{\Psi}\left(d\right)=-i\omega\int_{0}^{d}g\left(d,z\right)\delta\mathbf{\Pi}\left(z\right)\mathbf{\Psi}\left(z\right)dz. \tag{4.17}$$

By substituting $\mathbf{\Psi}(z)=e^{-i\omega\mathbf{\Pi}z}\mathbf{\Psi}(0)$ and $g(d,z)=e^{-i\omega(d-z)\mathbf{\Pi}}$ into Eq. (4.17), we obtain

$$\begin{aligned}\delta\mathbf{\Psi}\left(d\right)&=-i\omega\int_{0}^{d}e^{-i\omega(d-z)\mathbf{\Pi}}\delta\mathbf{\Pi}\left(z\right)e^{-i\omega\mathbf{\Pi}z}\,\mathbf{\Psi}(0)dz\\&=-i\omega\,e^{-i\omega d\mathbf{\Pi}}\int_{0}^{d}e^{i\omega z\mathbf{\Pi}}\delta\mathbf{\Pi}\left(z\right)e^{-i\omega z\mathbf{\Pi}}\,\mathbf{\Psi}(0)dz.\end{aligned} \tag{4.18}$$

Note that $\mathbf{\Pi}$ is a function of incident angle. Since Eq. (4.18) is an integral operation, a wide range of incident angle would offer more information and yield tighter constrain on the solution space. The term $\int_{0}^{d}e^{i\omega z\mathbf{\Pi}}dz$ in Eq. (4.18) can be viewed as Fourier transform, which may lead to an oscillation in LC director profile from the inverse problem retrieval procedure.

From Eq. (2.40), Eq. (2.46), and Eq. (2.55), $\mathbf{\Psi}$ becomes a function of pretilt angle profile $\{\theta(z)\}_{z=z_1,z_2,...,z_n}=\{\theta_1,\theta_2,...,\theta_n\}$ where n is the number of LC layers

$$\mathbf{\Psi}_{\mathbf{output}}\left(\theta_1,\theta_2,...,\theta_n\right)=\mathbf{B}\left(\theta_1,\theta_2,...,\theta_n\right)\mathbf{\Psi}_{\mathbf{in}}. \tag{4.19}$$

The equation for the inverse problem of LC is given:

$$\begin{aligned} d\mathbf{\Psi} &= \mathbf{J}\cdot d\boldsymbol{\theta} \\ &= \left(\frac{\partial\mathbf{B}}{\partial\theta_1}d\theta_1+\frac{\partial\mathbf{B}}{\partial\theta_2}d\theta_2+...+\frac{\partial\mathbf{B}}{\partial\theta_n}d\theta_n\right)\mathbf{\Psi}_{\mathbf{in}}. \end{aligned} \tag{4.20}$$

The Jacobian matrix in Eq. (4.20) can be obtained by using Eq. (4.19) and (2.55):

$$\begin{aligned} \mathbf{J} &= \frac{\partial\mathbf{B}}{\partial\boldsymbol{\theta}} \\ &= \frac{\partial[\left(\mathbf{P}_+ - \mathbf{U}_\mathbf{b}\mathbf{P}_-\right)^{-1}\mathbf{U}_\mathbf{b}\mathbf{\Psi}_{\mathbf{in}}]}{\partial\boldsymbol{\theta}} \\ &= \left(\frac{\partial[\left(\mathbf{P}_+ - \mathbf{U}_\mathbf{b}\mathbf{P}_-\right)^{-1}]}{\partial\boldsymbol{\theta}}\cdot\mathbf{U}_\mathbf{b}+\left(\mathbf{P}_+ - \mathbf{U}_\mathbf{b}\mathbf{P}_-\right)^{-1}\frac{\partial\mathbf{U}_\mathbf{b}}{\partial\boldsymbol{\theta}}\right)\mathbf{\Psi}_{\mathbf{in}}. \end{aligned} \tag{4.21}$$

The inverse matrix in Eq. (4.21) is given by following the mathematical operation

$$\begin{aligned} &\mathbf{A}^{-1}\left(\mathbf{x}\right)\mathbf{A}\left(\mathbf{x}\right)=\mathbf{I} \\ &\Rightarrow \frac{\partial\left(\mathbf{A}^{-1}\mathbf{A}\right)}{\partial x}=0 \\ &\Rightarrow \frac{\partial\mathbf{A}^{-1}}{\partial x}\cdot\mathbf{A}+\mathbf{A}^{-1}\frac{\partial\mathbf{A}}{\partial x}=0 \\ &\Rightarrow \frac{\partial\mathbf{A}^{-1}}{\partial x}\cdot\mathbf{A}=-\mathbf{A}^{-1}\frac{\partial\mathbf{A}}{\partial x} \\ &\Rightarrow \frac{\partial\mathbf{A}^{-1}}{\partial x}=-\mathbf{A}^{-1}\frac{\partial\mathbf{A}}{\partial x}\cdot\mathbf{A}^{-1}. \end{aligned} \tag{4.22}$$

By substituting Eq. (4.20) into Eq. (4.19) we obtain

$$
\begin{aligned}
\mathbf{J} &= \left(\frac{\partial\left(\left(\mathbf{P}_{+} - \mathbf{U}_{\mathbf{b}}\mathbf{P}_{-}\right)^{-1}\right)}{\partial\boldsymbol{\theta}} \cdot \mathbf{U}_{\mathbf{b}} + \left(\mathbf{P}_{+} - \mathbf{U}_{\mathbf{b}}\mathbf{P}_{-}\right)^{-1} \frac{\partial\left(\mathbf{U}_{\mathbf{b}}\right)}{\partial\boldsymbol{\theta}} \right) \boldsymbol{\Psi}_{\mathbf{in}} \\
&= \begin{pmatrix} -\left(\mathbf{P}_{+} - \mathbf{U}_{\mathbf{b}}\mathbf{P}_{-}\right)^{-1} \cdot \dfrac{\partial\left(\left(\mathbf{P}_{+} - \mathbf{U}_{\mathbf{b}}\mathbf{P}_{-}\right)\right)}{\partial\boldsymbol{\theta}} \cdot \left(\mathbf{P}_{+} - \mathbf{U}_{\mathbf{b}}\mathbf{P}_{-}\right)^{-1} \cdot \mathbf{U}_{\mathbf{b}} \\ +\left(\mathbf{P}_{+} - \mathbf{U}_{\mathbf{b}}\mathbf{P}_{-}\right)^{-1} \cdot \dfrac{\partial\left(\mathbf{U}_{\mathbf{b}}\right)}{\partial\boldsymbol{\theta}} \end{pmatrix} \boldsymbol{\Psi}_{\mathbf{in}} \\
&= \begin{pmatrix} \left(\mathbf{P}_{+} - \mathbf{U}_{\mathbf{b}}\mathbf{P}_{-}\right)^{-1} \cdot \dfrac{\partial\left(\mathbf{U}_{\mathbf{b}}\right)}{\partial\boldsymbol{\theta}} \cdot \mathbf{P}_{-} \cdot \left(\mathbf{P}_{+} - \mathbf{U}_{\mathbf{b}}\mathbf{P}_{-}\right)^{-1} \cdot \mathbf{U}_{\mathbf{b}} \\ +\left(\mathbf{P}_{+} - \mathbf{U}_{\mathbf{b}}\mathbf{P}_{-}\right)^{-1} \cdot \dfrac{\partial\left(\mathbf{U}_{\mathbf{b}}\right)}{\partial\boldsymbol{\theta}} \end{pmatrix} \boldsymbol{\Psi}_{\mathbf{in}}.
\end{aligned}
\tag{4.23}
$$

And by substituting Eq. (2.52) into Eq. (4.21), we have

$$
\begin{aligned}
\mathbf{J} &= \begin{pmatrix} \left(\mathbf{P}_{+} - \mathbf{U}_{\mathbf{b}}\mathbf{P}_{-}\right)^{-1} \cdot \dfrac{\partial\left(\mathbf{U}_{\mathbf{b}}\right)}{\partial\boldsymbol{\theta}} \cdot \mathbf{P}_{-} \cdot \left(\mathbf{P}_{+} - \mathbf{U}_{\mathbf{b}}\mathbf{P}_{-}\right)^{-1} \cdot \mathbf{U}_{\mathbf{b}} \\ +\left(\mathbf{P}_{+} - \mathbf{U}_{\mathbf{b}}\mathbf{P}_{-}\right)^{-1} \cdot \dfrac{\partial\left(\mathbf{U}_{\mathbf{b}}\right)}{\partial\boldsymbol{\theta}} \end{pmatrix} \boldsymbol{\Psi}_{\mathbf{in}} \\
&= \begin{pmatrix} \left(\mathbf{P}_{+} - \mathbf{U}_{\mathbf{b}}\mathbf{P}_{-}\right)^{-1} \cdot \mathbf{T}_{2}^{-1} \cdot \dfrac{\partial\left(P(\boldsymbol{\Pi})\right)}{\partial\boldsymbol{\theta}} \cdot \mathbf{T}_{1} \cdot \mathbf{P}_{-} \cdot \left(\mathbf{P}_{+} - \mathbf{U}_{\mathbf{b}}\mathbf{P}_{-}\right)^{-1} \cdot \mathbf{U}_{\mathbf{b}} \\ +\left(\mathbf{P}_{+} - \mathbf{U}_{\mathbf{b}}\mathbf{P}_{-}\right)^{-1} \cdot \mathbf{T}_{2}^{-1} \cdot \dfrac{\partial\left(P(\boldsymbol{\Pi})\right)}{\partial\boldsymbol{\theta}} \cdot \mathbf{T}_{1} \end{pmatrix} \boldsymbol{\Psi}_{\mathbf{in}}.
\end{aligned}
\tag{4.24}
$$

Furthermore, from Eq. (2.45), there are two ways to calculate $P(\boldsymbol{\Pi}) = e^{-iwh\boldsymbol{\Pi}}$

$$
\begin{aligned}
e^{-iwh\boldsymbol{\Pi}} &= e^{-iwh\mathbf{QDQ}^{-1}} \\
&= \mathbf{Q}e^{-iwh\mathbf{D}}\mathbf{Q}^{-1} \\
&= \mathbf{Q} \cdot \begin{bmatrix} e^{-iwhd_1} & 0 & \cdots \\ 0 & e^{-iwhd_2} & \cdots \\ \cdots & \cdots & \cdots \end{bmatrix} \cdot \mathbf{Q}^{-1},
\end{aligned}
\tag{4.25}
$$

or

$$
e^{-iwh\boldsymbol{\Pi}} = I + \left(-iwh\boldsymbol{\Pi}\right) + \left(-iwh\boldsymbol{\Pi}\right)^{2} + \left(-iwh\boldsymbol{\Pi}\right)^{3} + \left(-iwh\boldsymbol{\Pi}\right)^{4} + \ldots. \tag{4.26}
$$

Eq. (4.25) uses the matrix diagonalization technique to solve an eigenvalue-eigenvector problem of $\boldsymbol{\Pi}$ and $\mathbf{Q}$ is the resulting unitary matrix formed by the eigenvectors of $\boldsymbol{\Pi}$. Eq. (4.26) uses the Taylor expansion of an exponential

function. Eq. (4.25) is more accurate in calculating exponential function than Eq. (4.26) since we cannot include infinite orders of the expansion. But the advantage of Eq. (4.26) is that the derivative can be performed quite easily

$$\begin{aligned}\frac{\partial P(\mathbf{\Pi})}{\partial \boldsymbol{\theta}} &= \frac{\partial[\mathbf{I}+(-iwh\mathbf{\Pi})+(-iwh\mathbf{\Pi})^2+(-iwh\mathbf{\Pi})^3+(-iwh\mathbf{\Pi})^4+...]}{\partial \boldsymbol{\theta}} \\ &= \frac{\partial[\mathbf{I}+(-iwh\mathbf{\Pi})+(-iwh\mathbf{\Pi})^2+(-iwh\mathbf{\Pi})^3+(-iwh\mathbf{\Pi})^4+...]}{\partial \boldsymbol{\varepsilon}} \cdot \frac{\partial \boldsymbol{\varepsilon}}{\partial \boldsymbol{\theta}},\end{aligned} \tag{4.27}$$

where $\mathbf{\Pi}$ is a function of dielectric tensor $\boldsymbol{\varepsilon}$ while $\boldsymbol{\varepsilon}$ a function of $\boldsymbol{\theta}$ as shown in Eq. (2.36) and Eq. (2.40).

$\mathbf{\Psi}$ carries the entire information about the intensity and phase of an optical wave. For a measurement, which the phase of the optical wave is perturbed by an external factor with a significant noise level, the noise influence can be amplified and seriously degrades the solution accuracy. Therefore, we convert the equation in the field representation to the form of intensity representation. This can be done by first separating $\frac{\partial \mathbf{\Psi}}{\partial \boldsymbol{\theta}}$ into the real and the imaginary part

$$\frac{\partial \mathbf{\Psi}}{\partial \boldsymbol{\theta}} = \frac{\partial(\mathrm{Re}\,\mathbf{\Psi})}{\partial \boldsymbol{\theta}} + i\frac{\partial(\mathrm{Im}\,\mathbf{\Psi})}{\partial \boldsymbol{\theta}}. \tag{4.28}$$

The intensity of an optical wave is represented as:

$$\mathbf{I} = \mathbf{E}^2 = (\mathrm{Re}\,\mathbf{\Psi})^2 + (\mathrm{Im}\,\mathbf{\Psi})^2. \tag{4.29}$$

So the derivative of the intensity to the pretilt angle can be written as

$$\frac{\partial \mathbf{I}}{\partial \boldsymbol{\theta}} = 2(\mathrm{Re}\,\mathbf{\Psi})\cdot\frac{\partial(\mathrm{Re}\,\mathbf{\Psi})}{\partial \boldsymbol{\theta}} + 2(\mathrm{Im}\,\mathbf{\Psi})\cdot\frac{\partial(\mathrm{Im}\,\mathbf{\Psi})}{\partial \boldsymbol{\theta}}. \tag{4.30}$$

Eq. (4.20), Eq. (4.24), Eq. (4.27), and Eq. (4.30) form the mathematical ground for

solving the inverse problem based on the Berreman matrix model of LC.

4.4 Simulation Results and Discussion

We first developed an experimental technique to acquire high-quality data for the inverse problem of LC. As shown in Figure 4-6, A He-Ne laser is used for the light source. The optical transmittance is resolved into T_x and T_y with an analyzer and detected with a CCD. As noted in Section 4.3, the more independent data are collected, the higher accurate solution be retrieved. Therefore, we combine a polarizer and a quarter wave plate to collect more data by setting the incident light at four different polarization states: three linear (22.5°, 67.5° and 112.5° to the laboratory x-axis) and one left circularly polarized light. A rotation stage is used to adjust the incident angle into the LC cell. We should let the covering range of incident angle as wide as possible. However, due to the experimental constrain, the widest range of incident angle with this apparatus only covers from -50° to 50°. But "how wide the range is sufficient to serve our purpose" is not easy to answer.

A $4\mu m$-thick planar alignment LC cell with 1° pretilt is used for the test run of the inverse problem. The director profile of the LC cell is generated with *Q*-tensor approach by using with a finite element PDE solver. The optical transmittance of the LC cell is predicted with an optical model based on the Berreman matrix method.

From the simulation data, the test run aims to investigate the effect of data regularization, the noise influence, and the finite range of incident angle for the LC inverse problem. Finally, we will demonstrate a complete procedure to retrieve the LC director profile by using the inverse problem method developed.

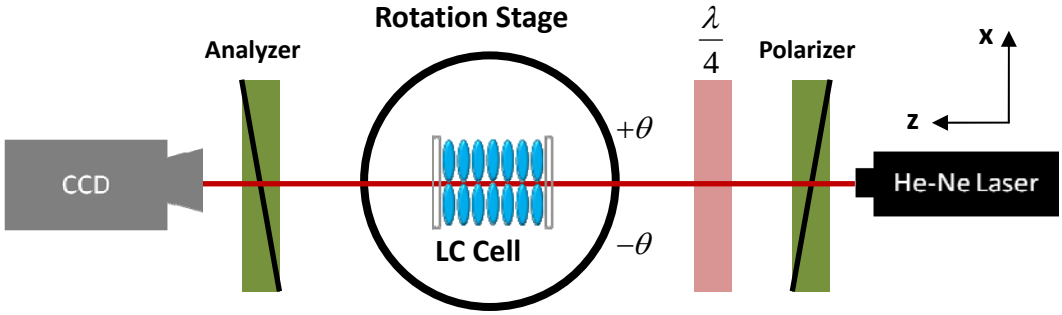

Figure 4-5. The experimental setup used to measure the optical transmittance data for inverse problem retrieval of LC director profile.

We first investigate the question about how many layers are needed to decompose the LC cell in order to yield an accurate prediction of optical transmittance. We discovered that the error mainly comes from the use of Taylor expansion shown in Eq. (4.26). Assuming the geometry depicted in Figure 4-6 is used, the calculation results with the two different methods Eq. (4.25) and Eq. (4.26) are compared in Table 4-1. We can see clearly that Eq. (4.25) yields an exact result which shall be independent of the layer number while Eq. (4.26) with an expansion up to the fourth order of Taylor expansion requires at least 200 layers in order to yield a result

with similar accuracy.

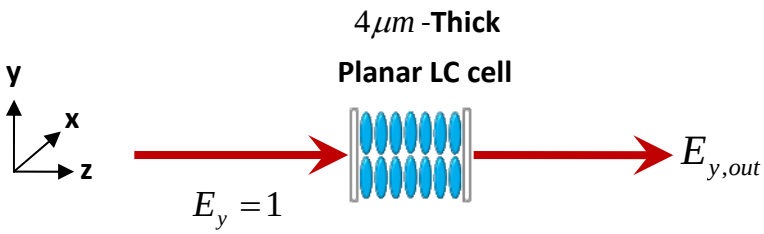

Figure 4-6. The schematic showing an idea that decomposes a LC cell into several layers to facilitate the calculation of optical transmittance.

Table 4-1: Comparison of the calculation results with the two different methods based on Eq. (4.25) and Eq. (4.26). Eq. (4.26) is calculated to the fourth order of Taylor expansion.

	200 layers	100 layers	50 layers
Eq. (4.25)	$0.9193 \cdot e^{1.4646i}$	$0.9193 \cdot e^{1.4646i}$	$0.9193 \cdot e^{1.4646i}$
Eq. (4.26)	$0.9173 \cdot e^{1.4711i}$	$0.8624 \cdot e^{1.556i}$	$0.1735 \cdot e^{2.2348i}$

How to choose a proper regularization parameter is a crucial issue for inverse problem. To answer the question, we set up a test run by adding one percent of noise to the simulated transmittance data and retrieve the LC director profile with inverse

problem method. The regularization parameter λ is chosen to be single constant value. Figure 4-7 (a) presents the retrieved LC director profile (line with cross symbol). Significant oscillation in the retrieved LC director profile can be clearly seen. By comparing to the simulated LC director profile from our PDE solver with FEM, we conclude that single constant regularization parameter does not give a reasonable solution. To solve the problem, we borrow some knowledge from the physics of LC, which demands the profile of the LC to be continuous and cannot change abruptly. However, we have to find an appropriate way to include the LC physics into the data regularization procedure.

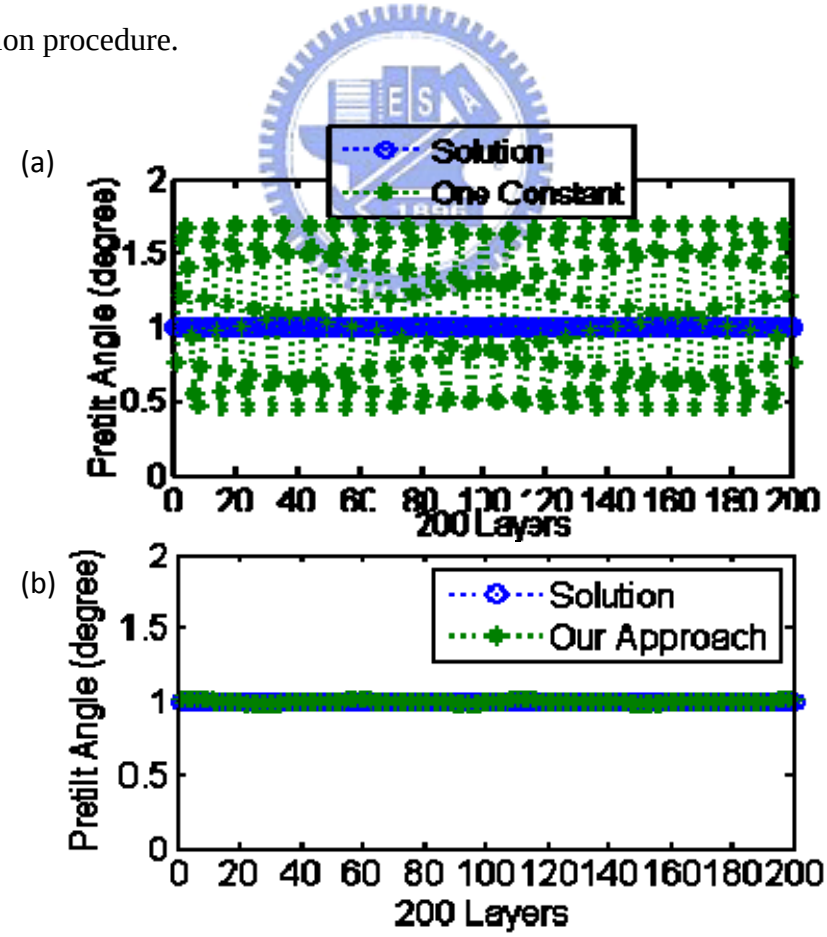

Figure 4-7. Comparison of the retrieved LC director profiles by using different

regularization methods. The transmittance data are prepared first with the finite element simulation based on Q-tensor approach and then added with one percentage of noise. (a) LC director profile retrieval by using one-constant regularization parameter λ. (b) LC director profile retrieval by using our new regularization scheme.

By looking into the one constant regularization method more deeply, Eq. (4.31) depict the entry point that introduces the data regularization parameter to solve an inverse problem.

$$\|\mathbf{Ax}-\mathbf{b}\|^2+\|\lambda\mathbf{Ix}\|^2. \tag{4.31}$$

We aim to find the most suitable $\mathbf{x}$ to minimize $\|\mathbf{Ax}-\mathbf{b}\|^2+\|\lambda\mathbf{Ix}\|^2$. However, it is quite opaque to probe into the meaning of the regularization parameter. Therefore, we introduce the singular value decomposition (SVD) to clarify it. The solution $\mathbf{x}$ with SVD is:

$$\mathbf{x}=\sum_i \frac{\sigma_i^2}{\sigma_i^2+\lambda^2}\cdot\frac{1}{\sigma_i}\mathbf{u_i^T b v_i}, \tag{4.32}$$

where

$$\begin{aligned}
&\mathbf{A}=\mathbf{UQV^T},\\
&\mathbf{U}=[\mathbf{u_1}\ \mathbf{u_2}\ \mathbf{u_3}...],\\
&\mathbf{Q}=\begin{bmatrix}\sigma_1 & 0 & ...\\ 0 & \sigma_2 & ...\\ 0 & 0 & ...\end{bmatrix}, \text{ and}\\
&\mathbf{V}=[v_1\ v_2\ v_3...]\quad .
\end{aligned} \tag{4.33}$$

The purpose of the regularization parameter λ can thus be understood with Eq. (4.32). The term of $\frac{\sigma_i^2}{\sigma_i^2+\lambda^2}$ can be viewed as a weighting which controls the importance of the singular values. Since the regularization parameter appears in the weighting factor, we can use Eq. (4.32) as the entry point to introduces LC physics into the data regularization procedure. We have known the director profile of LC must be continuous, so that a LC molecule and its surrounding nearest LC molecules shall share the same pointing direction. So the regularization parameter shall not be a single constant. We therefore propose the regularization parameter to be an array with a matrix form defined in Eq. (4.44). We assume that each LC molecule can experience a distance-dependent constraint from the neighboring LC molecules, resulting in a regularization matrix **λ** shown below

$$\boldsymbol{\lambda}=\begin{bmatrix} \lambda & 0.1\lambda & 0.01\lambda & 0 & 0 & \dots & \dots \\ 0.1\lambda & \lambda & 0.1\lambda & 0.01\lambda & 0 & 0 & \dots \\ 0.01\lambda & 0.1\lambda & \lambda & 0.1\lambda & 0.01\lambda & 0 & \dots \\ 0 & 0.01\lambda & 0.1\lambda & \lambda & 0.1\lambda & 0.01\lambda & \dots \\ 0 & 0 & 0.01\lambda & 0.1\lambda & \lambda & 0.1\lambda & \dots \\ 0 & 0 & \dots & \dots & \dots & \dots & \dots \\ \dots & \dots & \dots & \dots & \dots & \dots & \dots \end{bmatrix} \tag{4.34}$$

From the electrical engineering point of view, the data regularization procedure behaves like a signal filter, which depends on the range between singular values and λ. If the value of regularization parameter is close to the minimum singular value, it is easy to generate an oscillating behavior due to that during the iteration, the solution is modified too big. In this regard, we borrow a concept from global optimization that

uses small step at the initial stage and as soon as the solution is close enough to the correct answer, bigger steps are taken. Figure 4-8(b) displays the retrieved LC director profile by using the idea. Apparently, the oscillation has been efficiently eliminated as we expect.

Noise plays an important role in an inverse problem with experimental data. The noise in the measured data can be amplified and seriously affect the retrieved solution. To test the reliability of our new inverse problem technique, we add 1% to 30% noise level to the simulated data for a $4\mu m$-thick planar alignment LC cell with 1° pretilt angle. The results are shown in Figure 4-8(a). It is exciting to find that even at the 10% noise level the retrieved profile still agrees well with the true profile (shown by the curve with open circles). The average pretilt angles calculated from the retrieved profiles at 1% to 10% noise level are 1°, 0.99°, and 1.01°, respectively. The sum of absolute squared deviations of the retrieved profiles from the true profile as a function of the inserted noise level is plotted in Figure 4-8(b), indicating the root-mean squared (rms) deviation per data point as low as 0.02° can be achieved even with noisy data at 30% noise level.

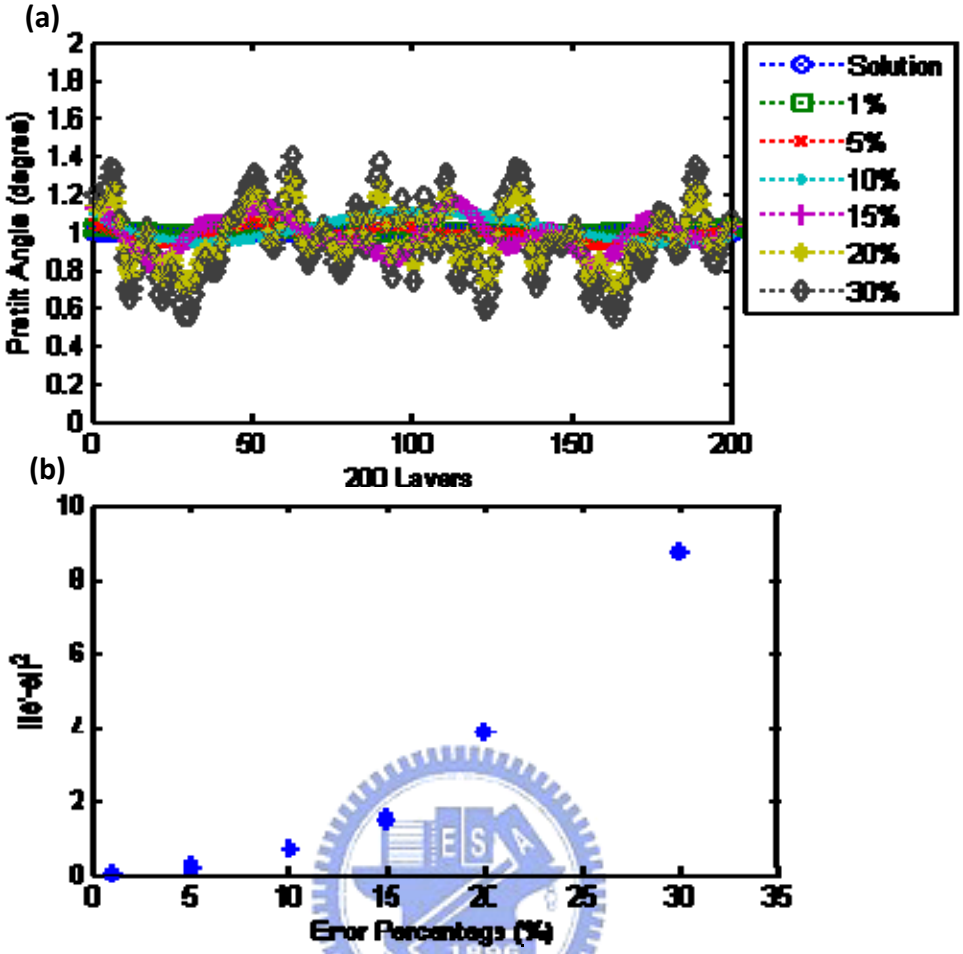

Figure 4-8. LC director profiles retrieved with the transmittance data. The data are prepared first with the finite element simulation based on Q-tensor approach and then added with 1%, 5%, 10%, 15%, 20%, 30% of noise. (a) The retrieved LC director profiles. (b) The statistics of the total deviation of the profiles to the true solution.

Note that the range of the incident angle shall contain similar information as that of the size of the solution space. We follow the previous procedure to analyze the influence of the range of incident angle. The following three ranges are used: I

$(+10^\circ \sim -10^\circ)$, II$(+30^\circ \sim -30^\circ)$, and III$(+50^\circ \sim -50^\circ)$. The sample remains the same $4\mu m$-thick planar alignment LC cell with 1° pretilt angle. The simulated LC optical transmittance data are assumed to be contaminated with 5% noise level. Figure 4-9 shows the retrieved LC director profiles with the three ranges of data. We see that the LC director profile from the data ranges I and II are not smooth with small deviation to the true profile by about 1.85° and 0.72°, respectively. The profile fluctuation reflects the problem due to the insufficient information containing in the input data I and II for the inverse problem retrieval.

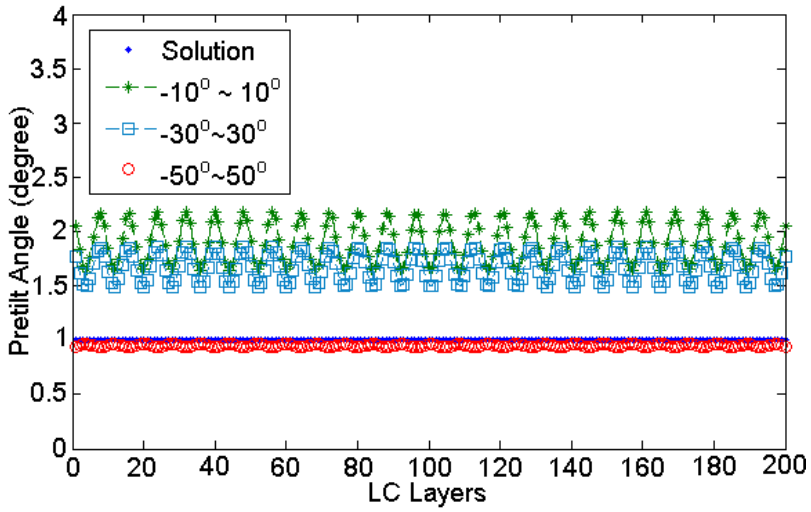

Figure 4-9. The retrieved LC director profiles with the three ranges of simulated optical transmittance data: I $(+10^\circ \sim -10^\circ)$, II$(+30^\circ \sim -30^\circ)$, and III$(+50^\circ \sim -50^\circ)$.

In summary, a new procedure was developed for the inverse problem retrieval of LC director profile. The performance of the new inverse problem technique was proven by investigating the effect of data regularization, the noise influence, and the finite range of incident angle for the LC inverse problem. A new data regularization method was proposed by implementing the LC physics into the inverse problem retrieval procedure. The integrated procedure was proven to be highly successful in the retrieval of LC director profile even that only a limited range of noisy data is available.

Chapter 5

Inverse Retrieval of Liquid Crystal Director Profile from Measured Optical Transmittance Data

In chapter 4, we developed a practical inverse problem procedure to retrieve the LC director profile from simulated data. The theoretical investigation indicates our method to be authentic even when the data have been contaminated with noise as high as 10%. In this chapter, we plan to use the inverse problem retrieval technique to recover the LC director profile from real measured data. The apparatus is to be described in details below.

5.1 Experimental Apparatus for Inverse Problem Retrieval

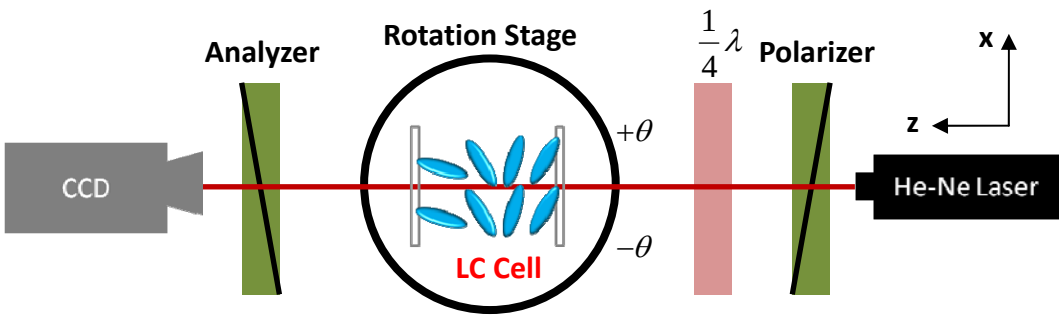

Figure 5-1. The experimental setup used to measure the optical transmittance data for inverse problem retrieval of LC director profile.

The experimental setup used to measure optical transmittance data for inverse problem retrieval of LC director profile is shown in Figure 5-1. A He-Ne laser is used for the light source. The optical transmittance is resolved into T_x and T_y with an analyzer and detected with a CCD. As noted in Section 4.3, the more independent data are collected, the higher accurate solution be retrieved. Therefore, we combine a polarizer and a quarter wave plate to collect more data by setting the incident light at four different polarization states: three linear (22.5°, 67.5° and 112.5° to the laboratory x-axis) and one left circularly polarized light. A rotation stage is used to adjust the incident angle into the LC cell. We should let the covering range of incident angle as wide as possible. However, due to the experimental constrain, the widest range of incident angle with this apparatus only covers from -50° to 50°.

The samples we measured are a $4\mu m$-thick LC cell in a splay alignment mode (OCB) and a $4\mu m$-thick LC cell with hybrid alignment. The measurement procedure of the two samples is repeated for three times by using different applied voltages of 0V, 2.5V, 5V.

5.2 Experimental Results and Discussion

The polarization-resolved optical transmittance measurement results of the LC

cell with hybrid alignment are presented in Figure 5-2 to Figure 5-4, with three different applied voltages of 0V, 2.5V, 5V, respectively. Similar measurement results of the OCB cell are presented in Figure 5-5 to Figure 5-7. Each figure comprises of T_x- and T_y-resolved optical transmittance plots by using an input light wave at four different polarization states. In each figure, the optical transmittance data (cross symbols) and the simulation curve (open squares) are compared. Deviations between the two curves can be observed and are used to adjust the calculated LC director profile during the inverse problem retrieval process. Figure 5-8 shows the retrieved LC director profiles for the hybrid cell with different applied voltages of 0V, 2.5V, 5V. Figure 5-9 presents the similar results for the OCB cell. In the Figures, two LC director profiles are plotted. One profile (blue symbols) is obtained from the FEM simulation on the LC cell with Q-tensor approach, and the other profile (red symbols) is retrieved from the measured optical transmittance data with our inverse problem retrieval technique. We also note that our inverse problem retrieval technique always converge to an almost identical result even the initial input profile is quite different. Although small oscillations remain on the retrieved profile at nonzero applied voltages, the overall agreement between the retrieved and the simulated profiles are excellent, indicating our inverse problem retrieval technique is fairly reliable and accurate for practical applications. The same conclusion can also be drawn for the

OCB cell presented in Figure 5-9.

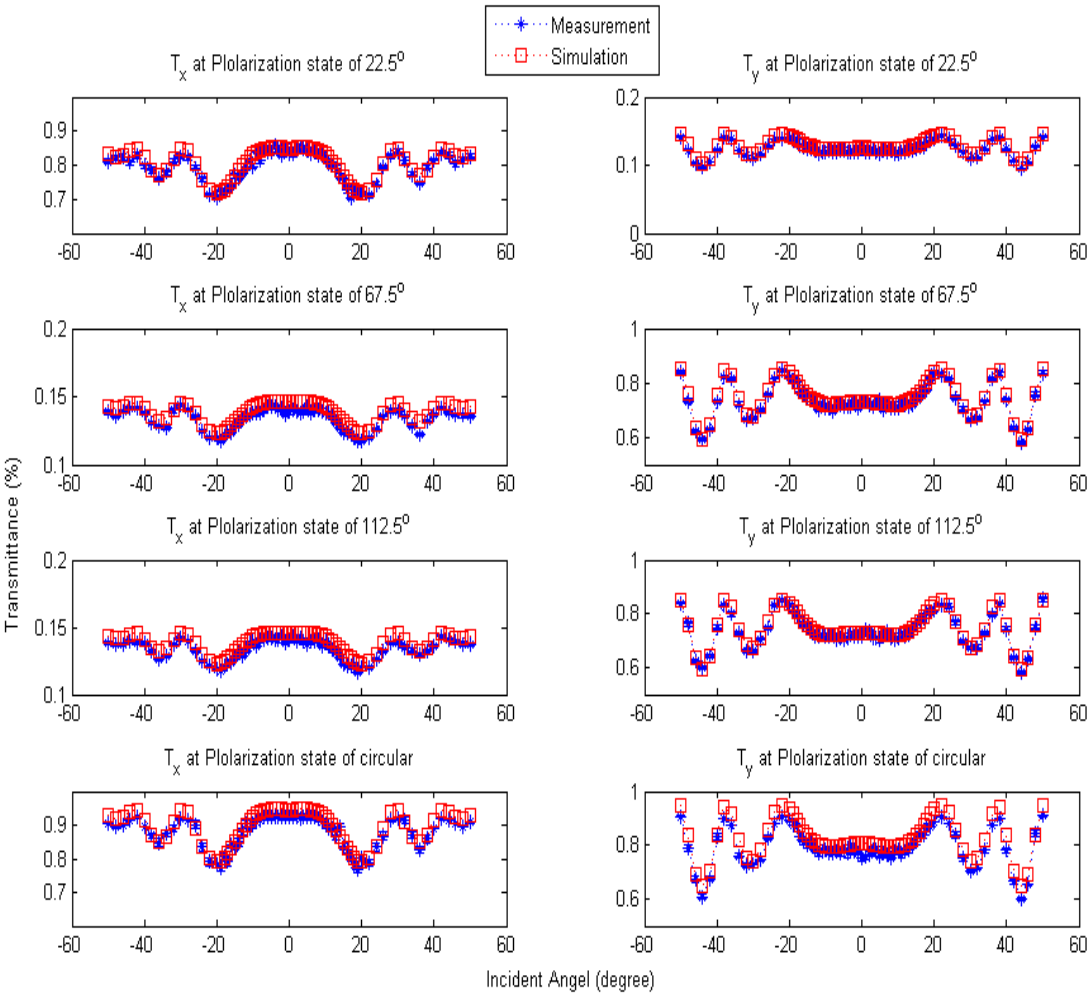

Figure 5-2. The polarization-resolved optical transmittance measurement results T_x and T_y of the LC cell with hybrid alignment are presented by using four different input polarization states (22.5°, 67.5°, 112.5°, and CP). The LC cell was applied with 0V. Two curves are included for comparison: red open squares: simulated curve with Berreman matrix technique, and blue cross symbols: the measured transmittance as a function of optical incident angle.

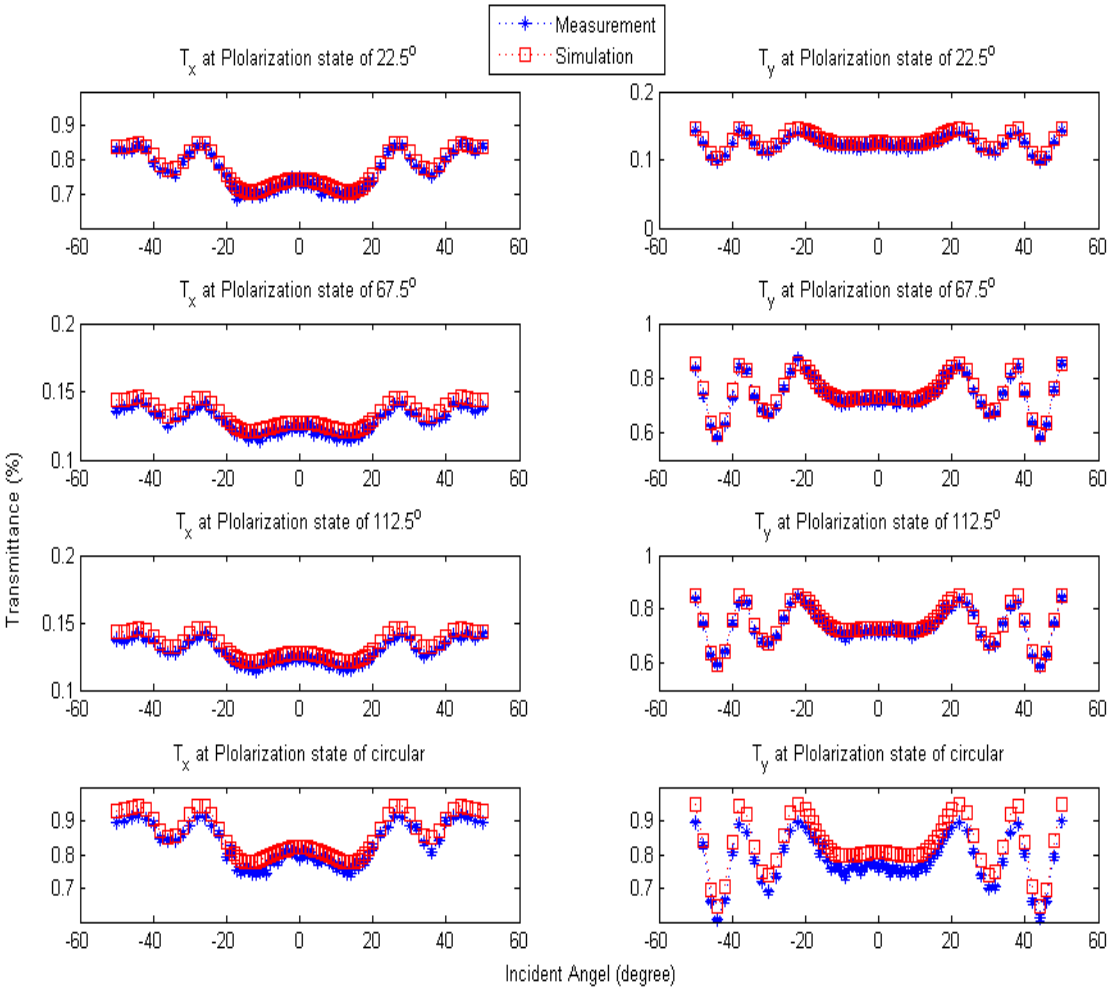

Figure 5-3. The polarization-resolved optical transmittance measurement results T_x and T_y of the LC cell with hybrid alignment are presented by using four different input polarization states (22.5°, 67.5°, 112.5°, and CP). The LC cell was applied with 2.5V. Two curves are included for comparison: red open squares: simulated curve with Berreman matrix technique, and blue cross symbols: the measured transmittance as a function of optical incident angle.

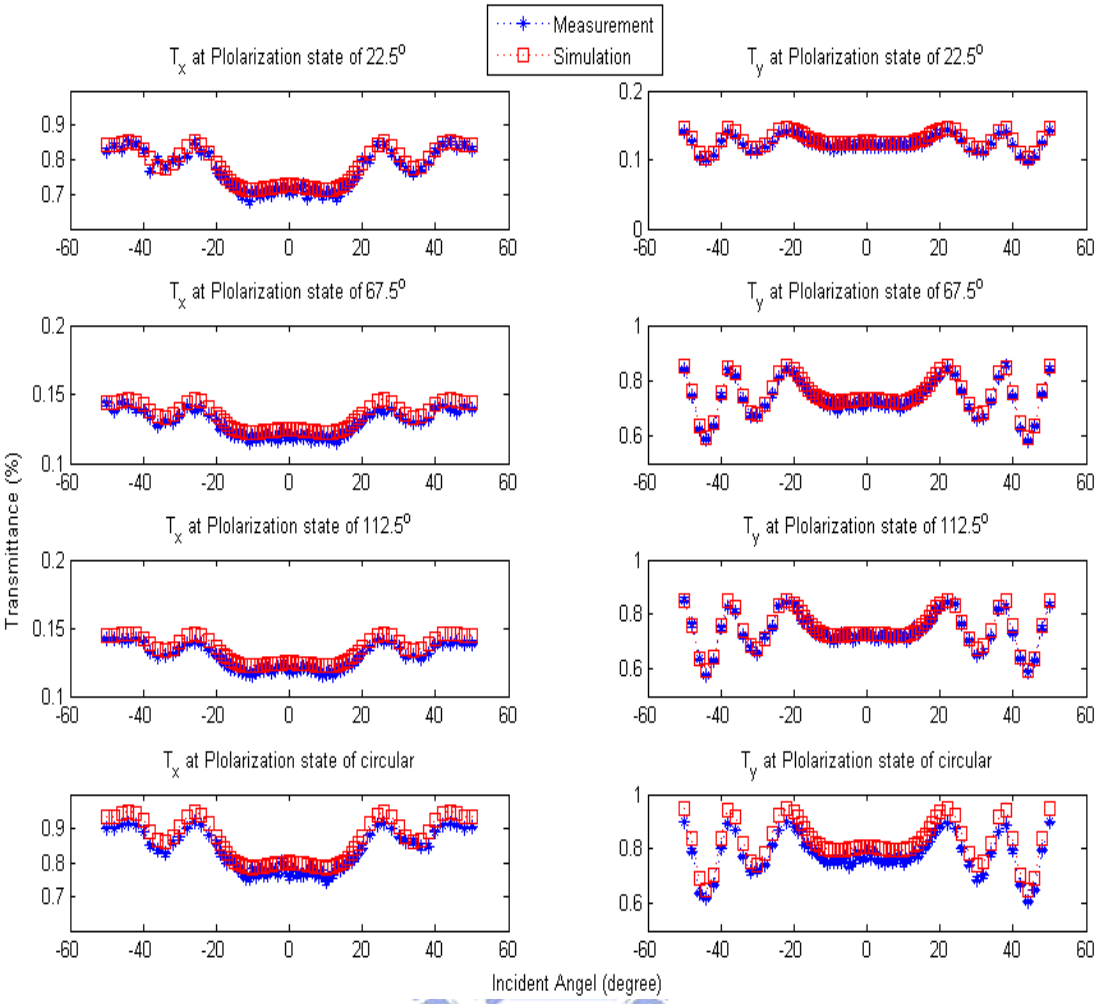

Figure 5-4. The polarization-resolved optical transmittance measurement results T_x and T_y of the LC cell with hybrid alignment are presented by using four different input polarization states (22.5°, 67.5°, 112.5°, and CP). The LC cell was applied with 5V. Two curves are included for comparison: red open squares: simulated curve with Berreman matrix technique, and blue cross symbols: the measured transmittance as a function of optical incident angle.

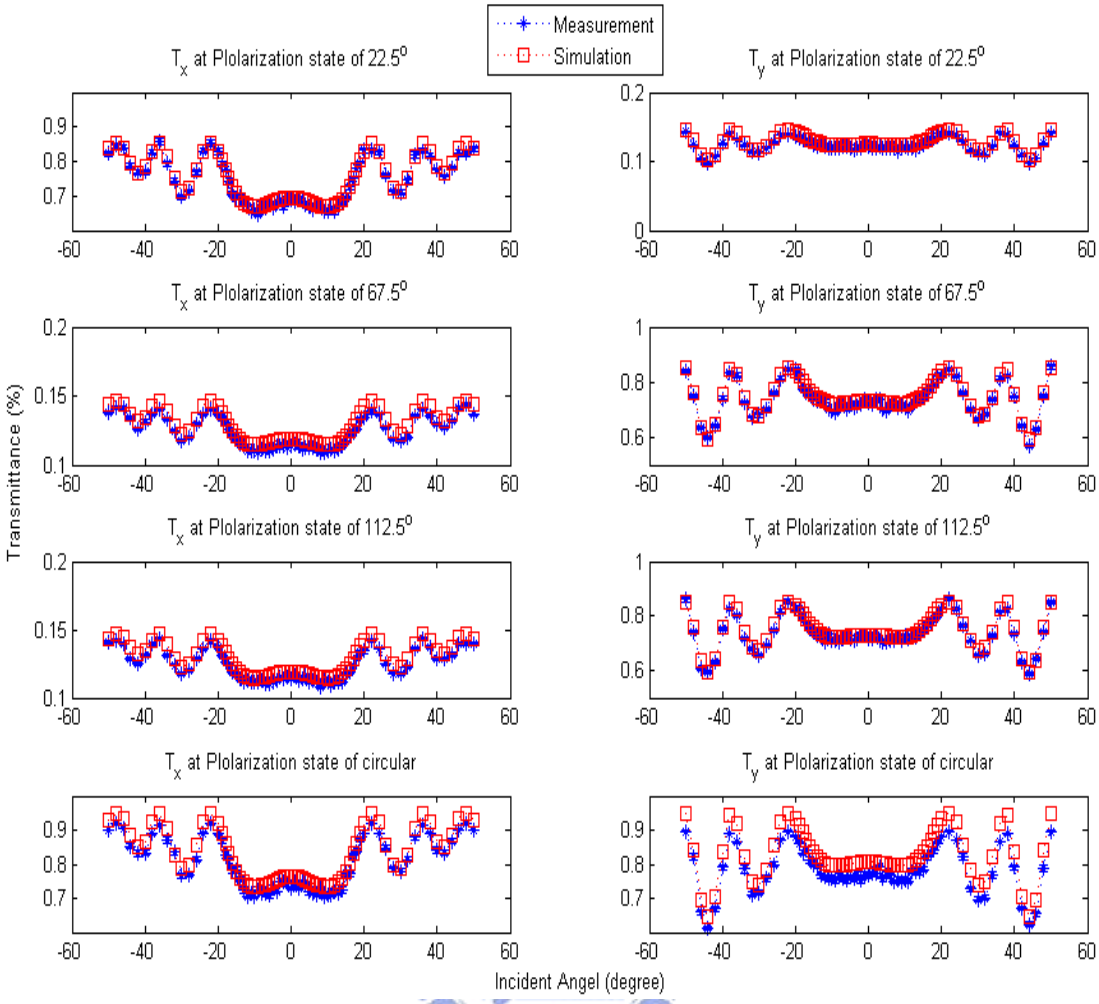

Figure 5-5. The polarization-resolved optical transmittance measurement results T_x and T_y the OCB cell with bend-splay alignment are presented by using four different input polarization states (22.5°, 67.5°, 112.5°, and CP). The LC cell was applied with 0V. Two curves are included for comparison: red open squares: simulated curve with Berreman matrix technique, and blue cross symbols: the measured transmittance as a function of optical incident angle.

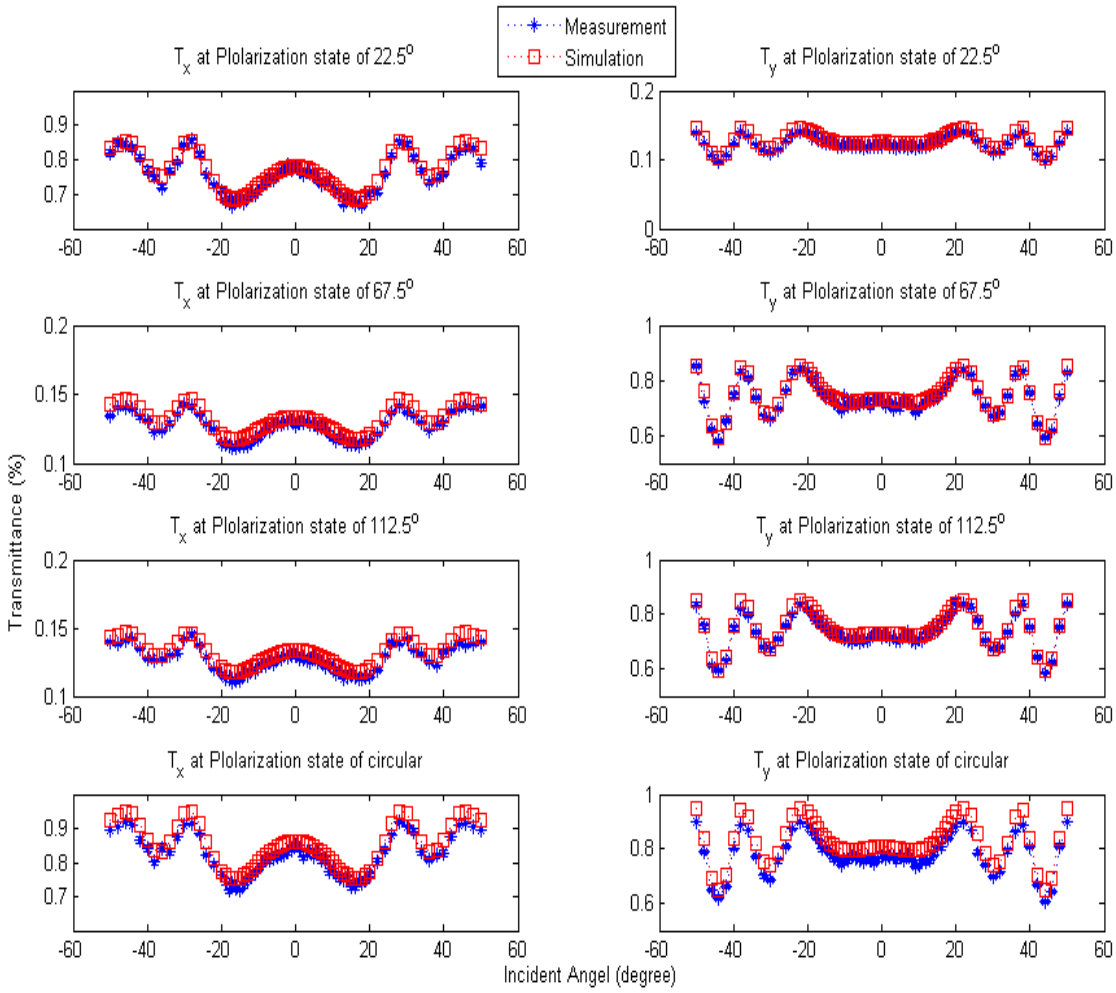

Figure 5-6. Figure 5-5. The polarization-resolved optical transmittance measurement results T_x and T_y the OCB cell with bend-splay alignment are presented by using four different input polarization states (22.5°, 67.5°, 112.5°, and CP). The LC cell was applied with 2.5V. Two curves are included for comparison: red open squares: simulated curve with Berreman matrix technique, and blue cross symbols: the measured transmittance as a function of optical incident angle.

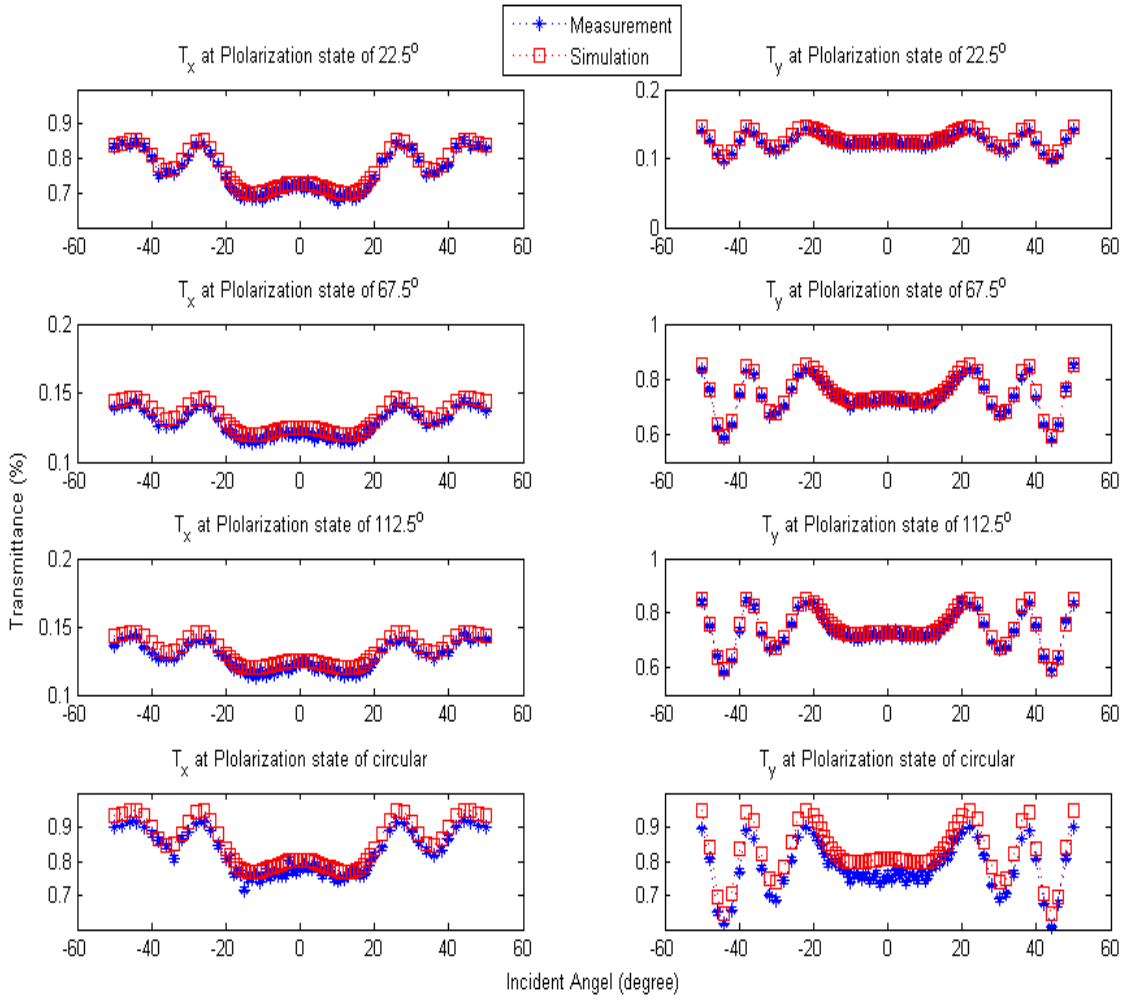

Figure 5-7. Figure 5-5. The polarization-resolved optical transmittance measurement results T_x and T_y the OCB cell with bend-splay alignment are presented by using four different input polarization states (22.5°, 67.5°, 112.5°, and CP). The LC cell was applied with 5V. Two curves are included for comparison: red open squares: simulated curve with Berreman matrix technique, and blue cross symbols: the measured transmittance as a function of optical incident angle.

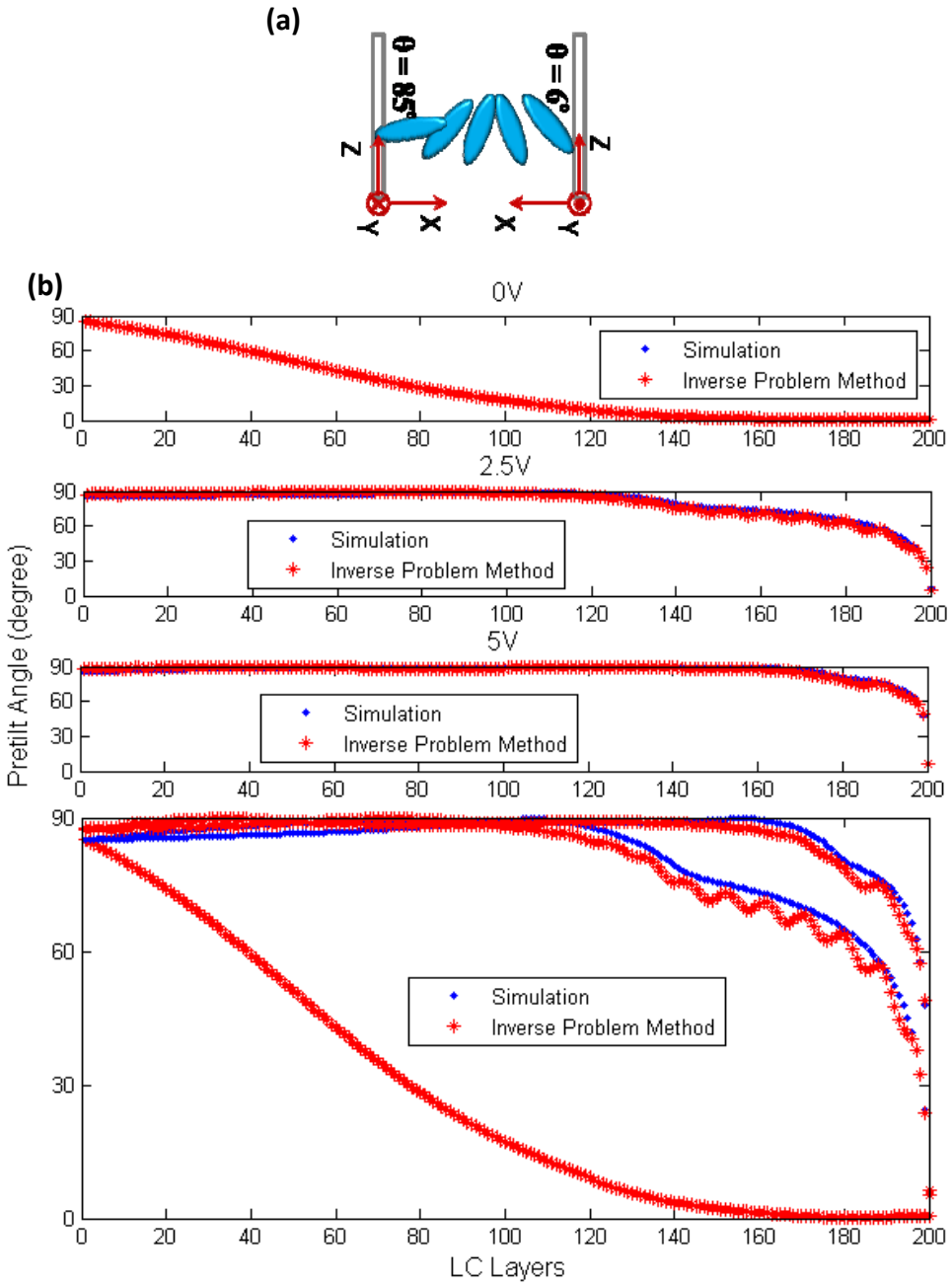

Figure 5-8. The retrieval director profiles of the hybrid cell by inverse problem method. (a) The coordinate system used to present the LC director profiles. (b) The retrieved director profiles of the hybrid cell biased at 0V, 2.5V, and 5V. Two profiles are included for comparison: red squares: retrieved profile, and blue symbols: the simulated profile calculated by the FEM with *Q*-tensor approach.

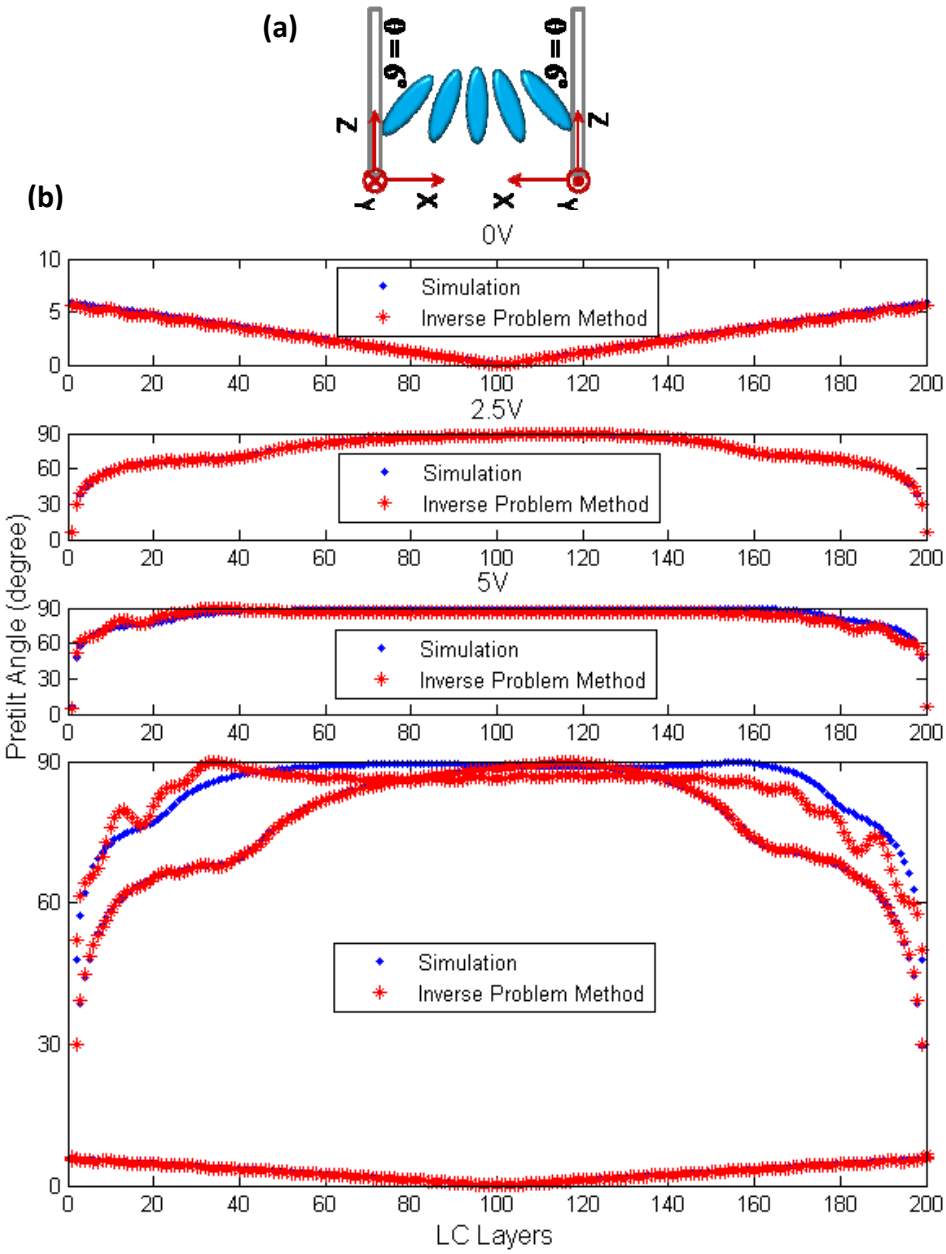

Figure 5-9. The retrieval director profiles of the OCB cell by inverse problem method. (a) The coordinate system used to present the LC director profiles. (b) The retrieved director profiles of the OCB cell biased at 0V, 2.5V, and 5V. Two profiles are included for comparison: red squares: retrieved profile, and blue symbols: the simulated profile calculated by the FEM with *Q*-tensor approach.

Chapter 6

Conclusions and Future Prospect of This Thesis Study

In conclusion of this thesis research, we have accomplished a finite element method (FEM) simulation of nematics liquid crystal by using *Q*-tensor approach and the optical response is also demonstrated by using Berreman matrix method. We use this simulation technique for comparing the result with the measurement data of the modified OCB cell. We find that including line-patterned hybrid alignment configuration into an OCB cell can effectively eliminate the transition time between the splay to the bend configuration. For the LC inverse problem, we have the detail analysis of the effect of data regularization, the noise influence, and the finite range of incident angle. We use our approach method for the data regularization of the inverse problem to reduce the oscillating behavior in the LC inverse problem retrieval procedure. The director profiles of an OCB and a hybrid cell with and without applied voltage have been successfully retrieved from measured optical transmittance data with our inverse problem retrieval technique.

Further improvements could be done in the future:

(1) Using a perturbation concept to modify the Berreman matrix method for analyzing three-dimensional LC devices.

The optical response for a three-dimensional LC device can only be calculated by the finite difference time domain (FDTD) method. The FDTD method takes a lot of computing time and needs to setup the whole equation system quite precisely. Although the Berreman matrix method can only calculate the optical response caused by azimuthal or pretilt angle, but the computing time is less. We can consult the concept in the reference [10] that using a perturbation to extend the Berreman matrix method for the change of the azimuthal and pretilt angle at the same time.

(2) Changing the line-patterned hybrid alignment configuration for the line-patterned homeotropic alignment configuration into an OCB cell for the symmetry structure.

Because the hybrid alignment configuration has the un-symmetry cell structure, so the relaxation time is not fast as the symmetry OCB cell. The homeotropic alignment configuration has the symmetry cell structure and also it can provide the vertical force as the hybrid alignment configuration.

(3) Replace Tikhonov regularization method with iterative regularization method [21,

The prior probability can be realized very well by neural network. We can offer the prior information about the liquid crystal to help training the neural network system. The iterative regularization method can be expressed as followed which compared to Tikhonov regularization $f_i = \frac{\sigma_i^2}{\sigma_i^2 + \lambda^2}$:

$$f_i = 1 - \left(1 - \sigma_i^2\right)^k \tag{6.1}$$

where k is the iteration number. Figure 6-1 gives an example of the iterative regularization method. When the iteration number increases, the more singular values we can keep. If it can be well designed, the convergence would be fast and reliable.

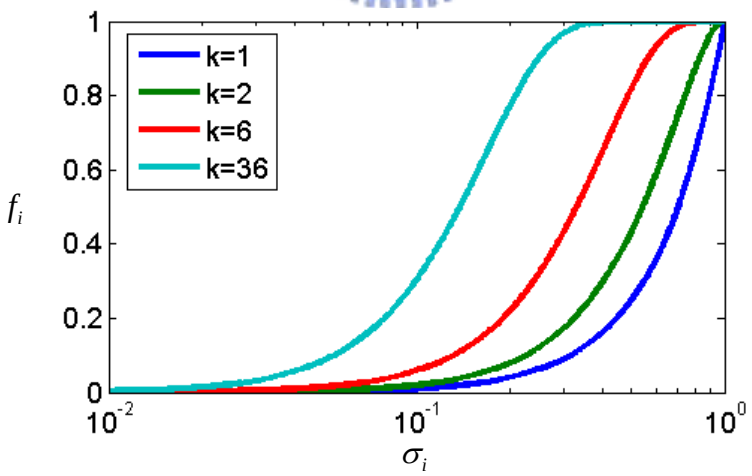

Figure 6-1. An example of the iterative regularization method with different iteration number.

(4) Use an optical microscope with high NA objective to simplify the data taking

procedure.

With one shot of image exposure, the resulting optical image contains the information with varying incident angles needed for the inverse problem retrieval with a schematic illustrated in Figure 6-2 (a). We can do a simple estimation about the numerical aperture of the objective lens which is around 0.76 for our incident angle range as in Figure 6-2 (b).

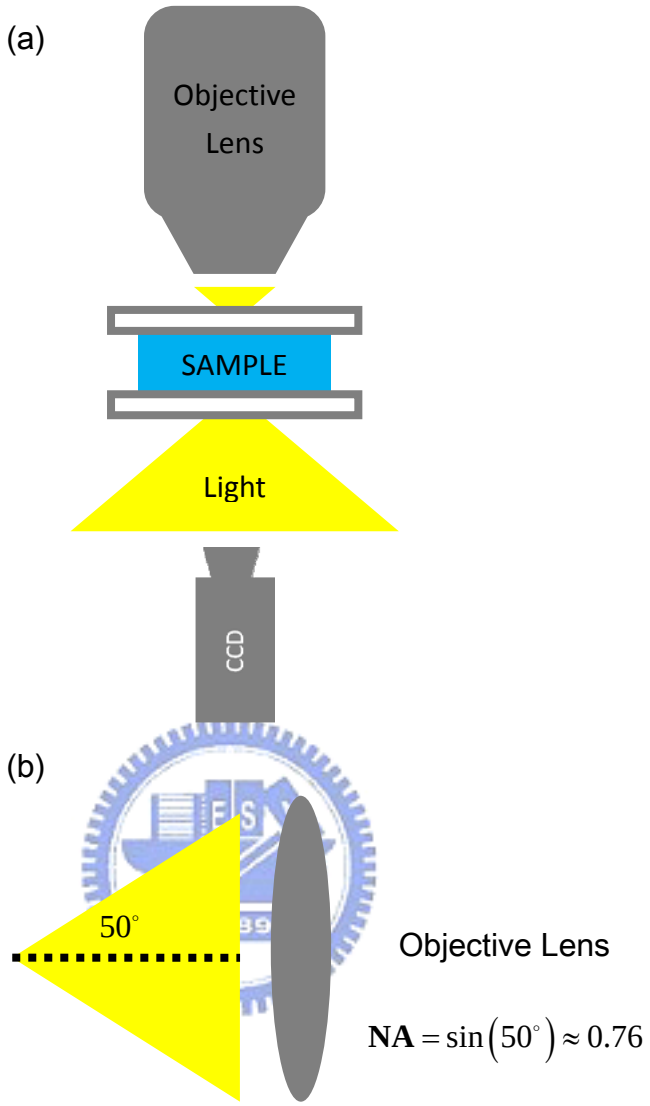

Figure 6-2. Optical microscope with high NA objective can be used to simplify the data taking procedure for inverse problem retrieval. (a) The experiment setup. (b) The NA value of the objective lens for our incident angle range.

References

[1] Denis Andrienko, *Introduction to Liquid Crystal*, International Max Planck Research School,

http://www.mpip-mainz.mpg.de/~andrienk/teaching/IMPRS/slides.pdf

[2] B. Jerome, *Rep. Prog. Phys.*, **5**4, 391, 1991

[3] E. Hecht, *Optics*, Addison-Wesley, 2002

[4] Hiroyuki Mori, Eugene C. Gartland Jr., Jack R. Kelly and Philip J. Bos, *Jpn. J. Appl. Phys.*, **38**, 135-146, 1999

[5] P.G. de Gennes and J. Prost, *The Physics of Liquid Crystal*, Oxford University Press, Oxford, 1993

[6] N. J. Mottram and C. J. Newton, "Introduction to Q-tensor theory", *Tech. Rep. 10/04*, University of Strathclyde, 2004

[7] S. Dickman, J. Eschler, O. Cossalter and D. A. Mlynski, *SID'93 Digest*, **638**, 1993

[8] Toralf Scharf, *Polarized Light in Liquid Crystals and Polymers*, John Wiley & Sons, 2002

[9] Gi-dong Lee, Philip J. Bos, Seon hong Ahn and Kyeong Hyeon Kim, *Phys. Rev. E*, **67**, 041715, 2003

[10] S. Faetti and G. C. Mutinati, *Phys. Rev. E*, **68**, 026601, 2003

[11] T. A. Davis and E. C. Gartland JR., S*IAM J. Numer. Anal.*, **35**, No. 1, pp. 336-362, 1998

[12] COMSOL Multiphysics, *http://www.comsol.com/*

[13] E. J. Acosta, M. J. Towler and H. G. Waltonm, *Liquid Crystal*, **27**, No.7, pp. 977-984, 2000

[14] K. Kuboki, T. Miyashita, T. Ishinabe and T. Uchida, *Mol. Cryst. Liq. Cryst.*, 410, pp. 391-400, 2004

[15] Philip J. Bos, P. A. Johnson Jr., Rickey Koehlen and K. Beran, *SID'83 Digest*, **30**, 1983

[16] J. Chen, *J. Appl. Phys.*, **52**, 724, 1981

[17] W. R. B. Lionheart and C. J. P. Newton, *New J. Phys*, **9**, 63, 2007

[18] Alex G. Ramm, *Inverse Problems: Mathematical and Analytical Techniques with Applications to Engineering*, Springer, 2005

[19] L. Rosasco, A. Caponnetto, E. De Vito and U. De Giovannini, *Learning, Regularization and Ill-Posed Inverse Problems*,

http://www6.cityu.edu.hk/ma/people/caponnetto/pub_files/lip_nips(CP1).pdf

[20] Fortran Linear Inverse Problem Solver (FLIPS),

http://kavaro.com/mediawiki/index.php/Flips

[21] Per Christian Hansen, *Iterative Regularization Methods*,

http://www2.imm.dtu.dk/~pch/Talks/iterative.ps

[22] A. Kirsche and C. Bockmann, *Pade iteration method for regularization*, ScienceDirect Applied Mathematics and Computation, **180**, pp. 648-663, 2006

[23] K. Fukumizu and S. Watanabe, *Probability Density Estimation by Regularization Method*, International Joint Conference on Neural Networks, **2**, pp. 1727-1730, 1993